Universitetet i Stavanger

FACULTY OF SCIENCE AND TECHNOLOGY

MASTER THESIS

Study programme/specialisation: Master in Engineering Structures and Materials / Civil Engineering Structures	The spring semester, 2022 Open
Author: Vítor Alexandre Artem Diniz Campos Mello Martins Pinto	
Programme coordinator Sudath C. Siriwardane Supervisor Main supervisor: Jasna B. Jakobsen Co-supervisor: Jónas Thor Snæbjörnsson	
Title of master's thesis: Stay cables of Stavanger City bridge: damping estimation and mitigation of vibrations	
Credits: 30	
Keywords: Cable vibrations Cable-stayed bridge Damping estimation Damper design	Number of pages: 75 + supplemental material/other: 0 Stavanger, 14/06/2022 date/year

Preface

My passion for bridge design culminates in this thesis, which is also the endpoint of my Master level study. Knowledge of wind engineering and structural dynamics, which were acquired during my time at the University of Stavanger, will be applied in this case study of the Stavanger City Bridge (Bybrua, in Norwegian).

This 44-years-old bridge is occasionally experiencing large cable vibration. To minimize the risk of cable damage due to fatigue, as well as limit the visual impact of such vibrations on the bridge users, the bridge operator Rogaland County Municipality (Rogalands Fulkeskommune, in Norwegian) is considering relevant means to limit the vibrations. This thesis aims to contribute to this work, by studying the existing damping level in the cable and a study of relevant damper for the cable.

I would like to express my gratitude to the supervisor of this study, Professor Jasna Jakobsen, for the knowledge and guidance throughout the making of this thesis. Professor Jasna, was also the lecturer of the two courses mentioned above, that will be extensively needed to understand the intricate mechanisms of cable vibration.

Professor Jónas Snæbjörnsson was also actively helpful, joining every meeting online from Iceland, sharing his very valuable opinion on the many problems and doubts.

Abstract

Bybrua was open to traffic in 1978 and it is a landmark of Stavanger. This stay-cabled bridge has occasionally experienced some large vibrations. The aim of the study is to evaluate what is the damping characteristics of the cable for the many different modes of vibrations. This will be done using different procedures such as Free Decay Response, Frequency Domain Decomposition and Random Decrement Technique. A range of external dampers will be discussed, and a preliminary analysis of a Stockbridge damper will be carried out in order to estimate what the result of placing such damper will cause in the vibration control.

Table of contents

List of figures

List of tables

Nomenclature

T	Cable tension force
m	Cable mass per unit length
g	Gravity acceleration
H	Cable horizontal force
L	Cable length
F	Cable tension force
h	Vertical distance between two endpoints of the inclined cable
l	Horizontal distance between two endpoints of the inclined cable
Re	Reynolds number
U	Mean wind velocity
D	Cable diameter
Sc	Scruton number
St	Strouhal number
f_s	Vortex shedding frequency
u_*	Friction velocity
z_0	Terrain roughness length
z_{ref}	Reference height
I_u	Turbulence intensity
F_D	Drag force
C_D	Drag coefficient
F_L	Lift force
C_L	Lift coefficient
U_{cr}	Critical wind velocity
c	Wake force constant
f_n	Natural frequency
n	Vibration mode
k	Stiffness
W_n	Mode shape
A_n	Vibration amplitude
S_x	Displacement power spectral density
$S_{\ddot{x}}$	Acceleration power spectral density

E	Envelope
BF	Best fitted exponential function
LB	Lower boundary
UB	Upper boundary
FDR	Free decay response
c	Damping coefficient
F	External force
PSD	Power Spectral Density

Δs	Differential cable length
υ	Air kinectic viscosity
δ_s	Logarithmic decrement damping
ρ	Air density
κ	Von Karman's constant
τ	Shear stress
ω_n	Natural frequency
ω	Frequency
ζ	Damping ratio
ϕ	Diameter
φ	Phase

1 Introduction

The principal of supporting bridge with ropes, chains or cables has been known since ancient times [1]. In the nineteenth-century, hundreds of chain-supported bridges were built in Europe, those chains can be made of wrought iron eye-bars and the towers were made of stone or bricks. The first modern cable-stayed bridge is the Strömsund Bridge, built in 1956. The materials and techniques used in Strömsund are similar to the ones used in more recent bridges.

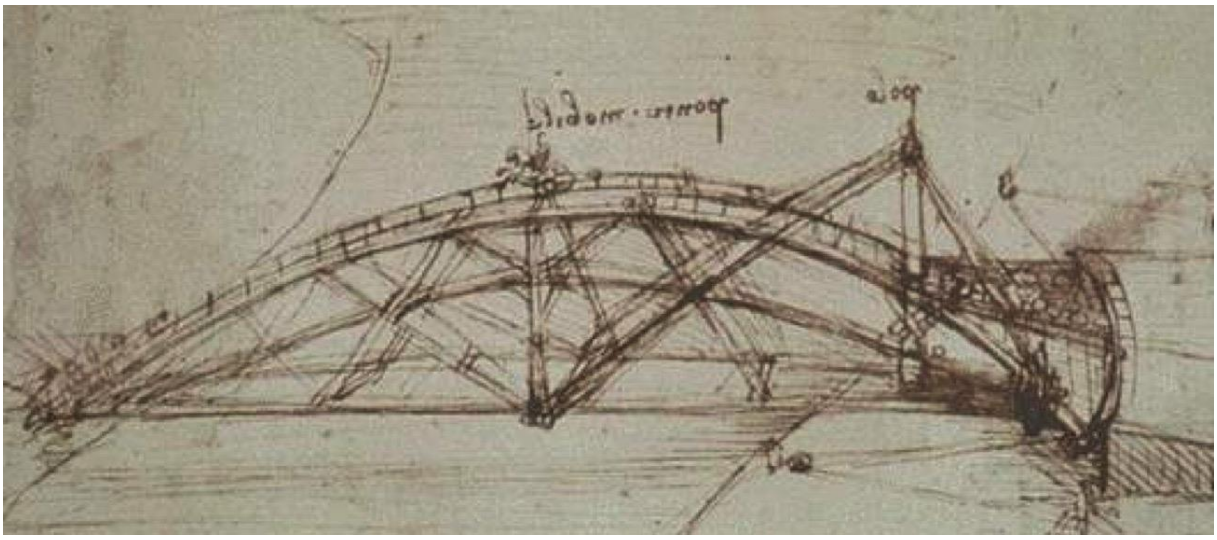

Figure 1 Cable supported bridge, by Leonardo da Vinci, 1485-1490

With advance in technology, design knowledge and theoretical background, the more recent bridge are becoming longer and slenderer. The slender structures can be more prone to vibration. The extreme slenderness of Tacoma Narrows Bridge, a depth-to-span ratio of 1:350 and the low torsional rigidity led to its failure under winds of only $18\,m/s$, the bridge experienced twisting oscillation due to pulsating wind eddies [1].

After the collapse of Tacoma Narrows Bridge, the dynamic studies of the cable supported bridge became an important subject at the structural design companies as well as in the research centres at universities.

This thesis aims to investigate dynamic response of Bybrua's stay cables. The stay cables are experiencing vibrations due to environmental loads, especially the rain-wind-induced vibration (RWIV) and wind-induced vibration (WIV) [2]. The structure has been monitored by the University of Stavanger in collaboration with the Rogaland County Municipality, therefore, the full-scale experimental data will be used.

Since cables of a cable-stayed bridge are slender structures with low inherent damping levels, they are prone to various types of wind induced vibrations. The related large deformations can

lead to damage due to fatigue of the cable (most notably at the anchorages) as had happened in Saint-Nazaire bridge (Figure 2).

Figure 2 Saint-Nazaire cable failure [3]

This thesis will investigate what is the natural frequencies and damping ratio of the cables, using different methods and comparing their results. Estimating damping characteristics of civil engineering structures can be a challenge due to the usual low damping coefficients, which can make the results very significantly. The size of the structure makes it difficult to be isolated from external conditions, such as wind loads and traffic.

An external damping device will be studied to mitigate vibration amplitudes. A simplified model, represented by a two degree of freedom system will be analysed.

2 Literature review

A generic overview of how cable-stayed bridge function, their concept, design and principals will be presented in this section. Moreover, a study of mechanical vibrations of cables, which phenomena triggers its motion and how damping can help mitigate those factors.

2.1 Structural systems for different bridge spans

When a long span bridge is designed, one must choose between trying to span the distance with a beam-like structure (which is cost-efficient for short to mid-spans) or by helping the beam-like structure with supporting cables.

Usually, a span of under 50m would be a pre-cast I-beam prestressed concrete structure or I-beam steel structure. For spans between $50\,m$ and $250\,m$ a balanced cantilever structural system is cost-efficient. The spans closer to $250\,m$ start to show girders that are too tall, the reason is the increasingly high negative bending moment near the supports. Bendorf bridge, built one decade before Bybrua, has a main span of $208\,m$, the girder height above the column is $10{,}5\,m$.

Figure 3 Bendorf bridge, visited by the municipal delegation [4]

From $250\,m$ up to $1000\,m$ the cable-stayed bridge is the most cost-effective solution. However, cable-stayed bridge can also be an option for shorter spans, if there is another reason that is not efficiency. For example, an architectural reason, where the slenderer appearance of a cable-stayed bridge is of interest, when compared to balanced cantilever that has a taller girder. This was the case of Bybrua. A municipal delegation went to visit similar bridges along the Rhine River to decide which solution would have the best appearance for the important part of the city. The cable-stayed bridge was chosen, even though that was not the cheapest option (the span is only 185m, which is shown to be below the optimum range for a cable-stay bridge,

however there is only one tower, therefore this solution would be similar to a 370m bridge if there were 2 towers). However, its slender appearance was considered better for the skylines of Stavanger [5].

When it comes to spans over 1000 m, a suspension bridge is the most efficient design due to many factors. One is that the tower can be made shorter than in a cable-stayed bridge of the same span. See Figure 4, where, for example, the Russky Bridge (cable-stayed bridge with a main span of $1104\ m$) presents a taller tower than the Great Belt Fixed Link East Bridge (suspension bridge with a main span of $1624\ m$).

In general, the tower of a cable-stayed bridge needs to be taller because of the angle between the cable and the deck. The shorter the tower, the more horizontal the cable is, which make it inefficient in carrying the vertical loads from the deck and traffic. The increasing tension force on the cable to compensate for a shallow angle can lead to excessive compression of the deck. Long and slender decks can show buckling problems if the deck has a high compression. Movement joints can experience large displacements due to creep effect in a highly compressed deck.

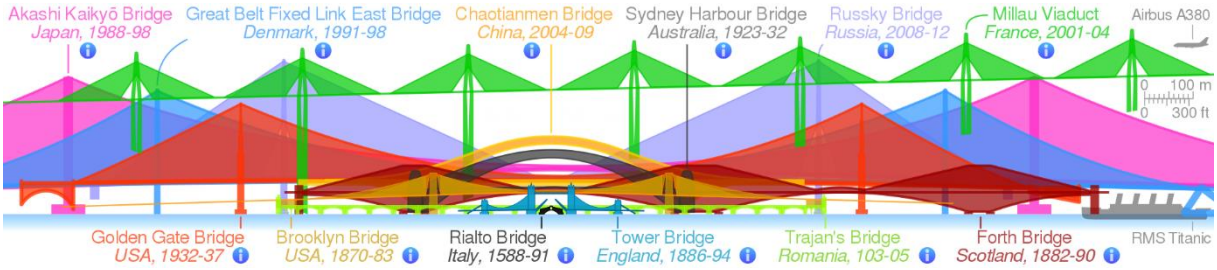

Figure 4 Comparison between many famous bridges [6]

2.2 Cable-stayed bridges

Within the cable-stayed bridges, there are three typical cable configurations in the vertical plane (Figure 5) [1].

Fan system shows a more difficult cable arrangement, since all the cable anchorages are close to each other at the tower, however, this solution display the cable in the most vertical orientation possible, as discussed in 2.1.

The harp system has evenly spaced cables in both the deck and the tower. This makes the system easier to detail and to build (due to the element being more similar thorough the structure).

The intermediate solution (semi-fan) has an easier detailing than the fan system due to the anchorages being further apart without compromising the angle at which the cables attach to the deck.

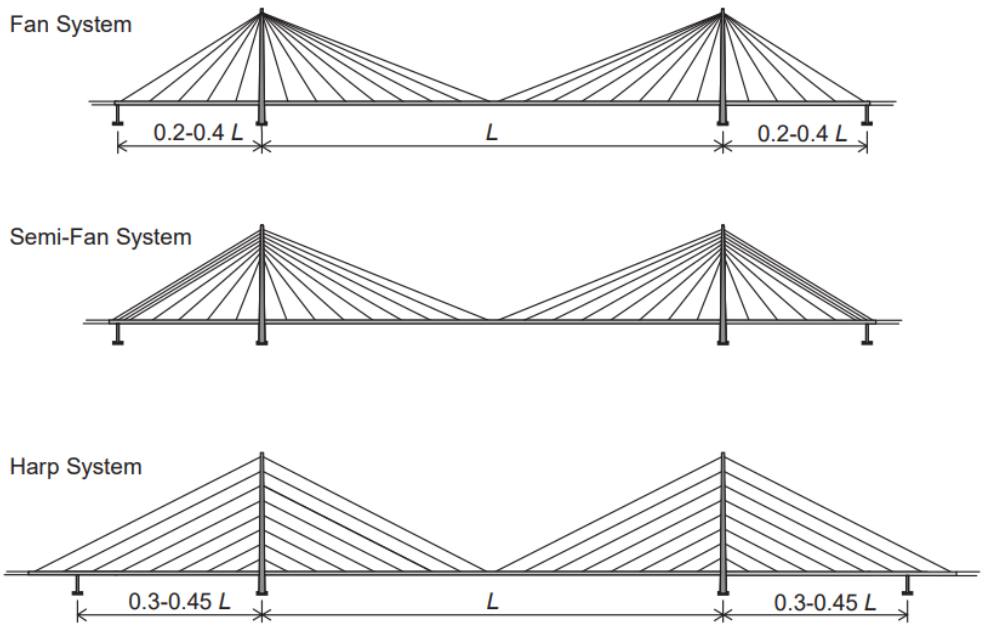

Figure 5 Cable configuration for cable-stayed bridges [1]

There is also a choice of configuration in the longitudinal spacing. Bridges built from 1950s to mid-1970s tend to have fewer cables and, therefore, larger distance between cables. This leads to cables being subjected to large axial forces which requires many strands per cable. More recent cable-stayed bridges have a higher number of cables, something that makes it possible for the cable to be made of a single strand. This helps the process of replacement of the cable when it is necessary. This will also lead to a more evenly supported deck, due to the more cables, and an easier construction, due to the mono-strand anchorages being smaller. However, the multi-cable system tends to experience more wind-induced vibrations [1], since the cable is lighter and thus present a smaller Scruton number 2.4.2.

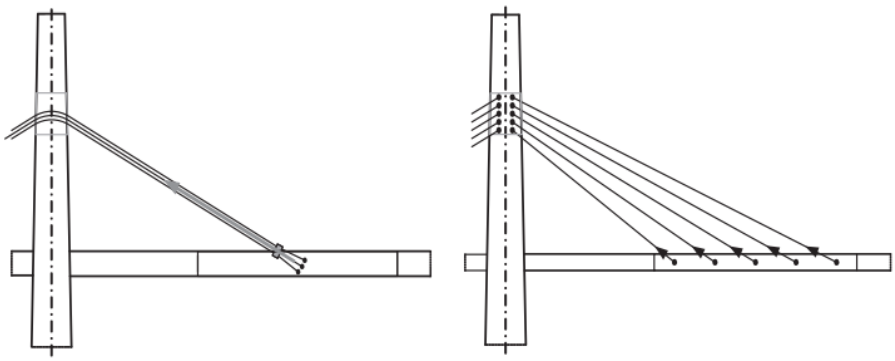

Figure 6 Few multi-strand cables (left) and multi-cable system (right) [1]

Cable-stayed bridges can also be different in the way the cables are transversally aligned to the deck. The cables can be in one single plane, usually the middle. This solution will lead to large

torsion in the deck, since the cables can only support the deck with one vertical force in the centre.

The cables can be parallel on each side, for two cables, or on each side and in the middle, if there are three cables in the cross-section. When using this solution, the girder does not need to be as transversally stiff as the previous case, because it is supported in more planes. This solution will lead to more cables and anchorage points needed.

The third arrangement is by inclined cables. This happens when the anchorage at the top of the tower is centred, and therefore the cables must spread sideways in order to reach their anchorage points at the deck level. Some transversal area might be lost due to lack of minimum height if the transversal inclination of the cables is shallow. The deck will have to endure a transversal compression due to the inclined cables.

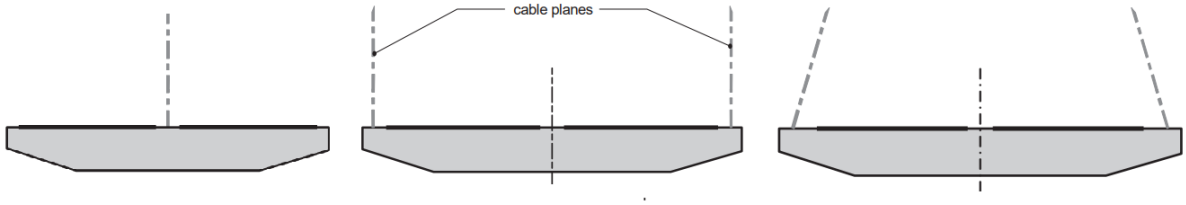

Figure 7 Distribution of the cables in the cross-section [1]

2.3 Cable

Cables are made in such a way that the cross-section area is relatively large for its second moment of area, this happens because the wires inside are not connect to each other, but only overlapping, which leads to low shear stress in between two wires. However, there is still friction between two wires.

The structural member will then have low flexural rigidity but a high longitudinal rigidity. This will ensure that the cable is primarily stressed in the direction of its axis, which is what it is intended to do. It is well known that axial forces are the most efficient way of carrying a load, bending being the second and torsion the last. Within the two cases of normal force, tension is more efficient than compression due to the potential effect of buckling on the latter.

Let a simple example show how efficient multi-wires cables are in carrying axial forces while maintaining a low flexural rigidity. If $100\ cm^2$ of steel cable is needed, one could choose a steel bar with diameter of $11.28cm$. That bar would have $795.8cm^4$ as second moment of area. However, if 100 strands of $1.128cm$ diameter are chosen, the desired area of $100cm^2$ would be achieved with only $1.591cm^4$ as second moment of area, if the friction between the wires are not considered.

The fact that cables are made out of many strands is also advantageous for robustness of the member. If there is, for example, crack growth in a cross section, the crack can lead to failure of the wire, but that will not drastically change the resistance of the cross-section. On the other hand, if it was one steel bar of the same area, the same crack could lead to more damage of the overall cross section.

The Silver Bridge, in the USA, which was a suspension bridge with eye-bar links instead of cables, collapsed due to a crack in the eye-bar [7], see Figure 8 for the cross section of the main chain of the suspension bridge. The increased redundancy due to a cable being made of many wires can be beneficial, see Figure 2 that shows that even a damaged cable might not collapse.

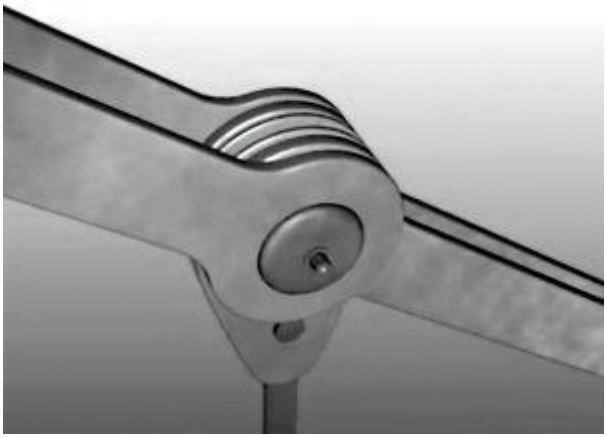

Figure 8 Silver Bridge eye bar link [7]

The commercially available morphologies for cables are locked coil cable, parallel wire cable and parallel strand cable.

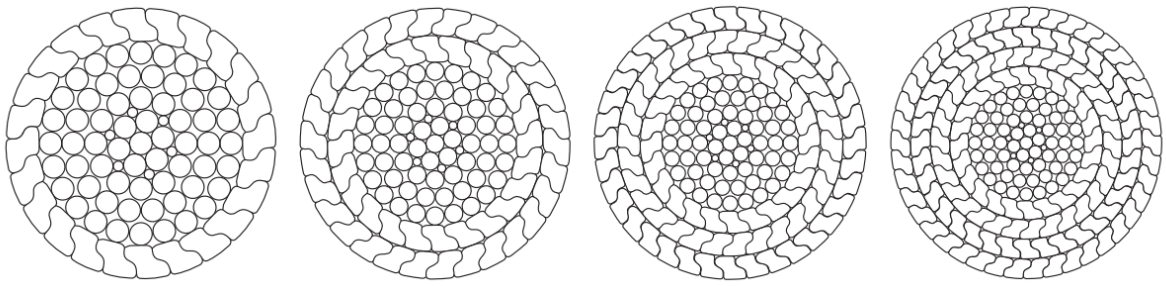

Figure 9 Examples of locked coil cable [8]

Locked coil cable has a compact cross section and a smooth and tight outer perimeter. Both the inner round wire and the outer Z-shaped are laid in a helical pattern, one clockwise and the next counterclockwise. This solution was used in Bybrua.

A locked coil cable with nominal diameter of $80\ mm$ displays an area of $4358\ mm^2$ [8]. For comparison, a cable made only of round wires and the same nominal diameter of $80\ mm$ has an area of $3870\ mm^2$ [8].

2.3.1 Cable curvature

An inextensible cable, hung between two points, subjected to a distributed vertical force will follow an equilibrium a curve called catenary.

According to Cardoso (2013) the catenary displayed by a cable with two end points at the same height can be studied as shown in Figure 10.

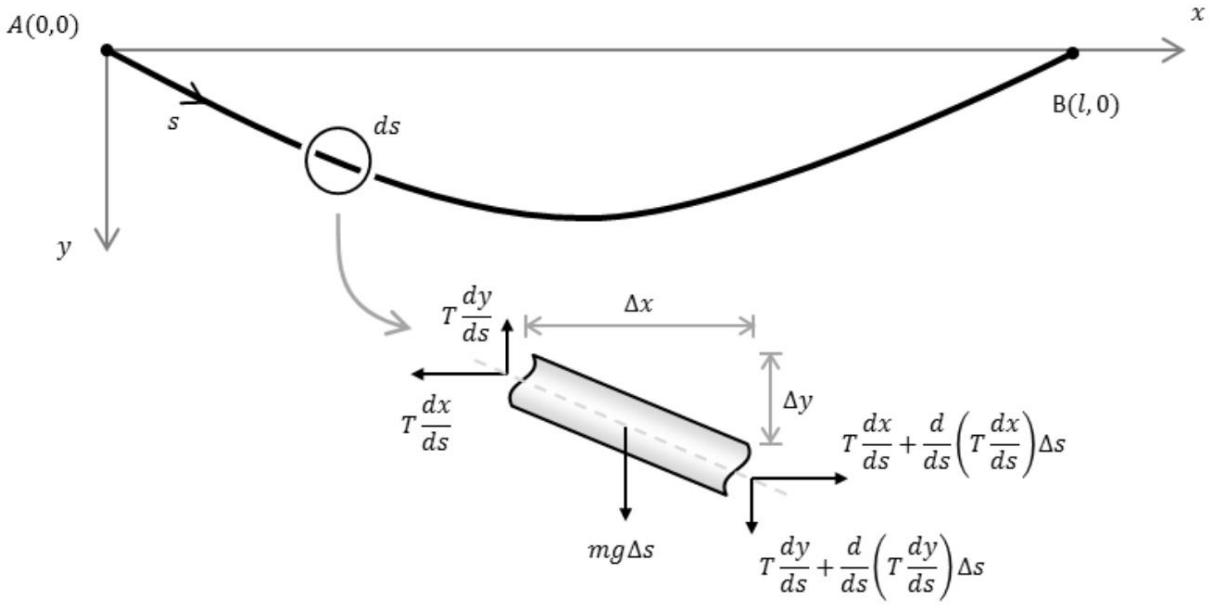

Figure 10 Free body diagram for a catenary [9]

Assuming the only force applied between the anchorage points is the distributed self-weight force mg, the static equilibrium of the element in the two direction is as follows.

$$\frac{d}{ds}\left(T\frac{dx}{ds}\right)\Delta s = 0 \qquad 1$$

$$\frac{d}{ds}\left(T\frac{dy}{ds}\right)\Delta s = -mg\Delta s \qquad 2$$

Integrating Equation 1 gives:

$$T\frac{dx}{ds} = c_1 = H \quad or \quad T = H\frac{ds}{dx} \qquad 3$$

Where $H\ [N]$ is the horizontal force, which is constant for the cable, because there is no horizontal loading between the anchorage points.

Taking the second form of Equation 3 into Equation 2 will give:

$$\frac{d}{ds}\left(H\frac{ds}{dx}\frac{dy}{ds}\right) = -mg \qquad 4$$

Further algebraic calculations give:

$$H\left(\frac{d^2y}{dx^2}\right) = -mg\frac{ds}{dx} \quad (5)$$

Using the trigonometric identity:

$$\cos^2(\theta) + \sin^2(\theta) = \left(\frac{dx}{ds}\right)^2 + \left(\frac{dy}{ds}\right)^2 \quad (6)$$

Then:

$$H\left(\frac{d^2y}{dx^2}\right) = -mg\sqrt{1 + \left(\frac{dy}{dx}\right)^2} \quad (7)$$

The solution is:

$$y = \frac{H}{mg}\left\{\cosh\left(\frac{mgl}{2H}\right) - \cosh\left(\frac{mg}{H}\left(\frac{l}{2} - x\right)\right)\right\} \quad (8)$$

Where l $[m]$ is distance between the anchorage points and y $[m]$ is the vertical distance of any given point of the cable, according to the coordinate system shown in Figure 10.

This solution is known to be numerically demanding due to the hyperbolic functions. Two other simplified methods can be used.

For cables where the two end points are at different height, which is the case of a cable-stayed bridge, Virlogeux (2005) shows that a simple study of static equilibrium can give the largest sag value with good accuracy.

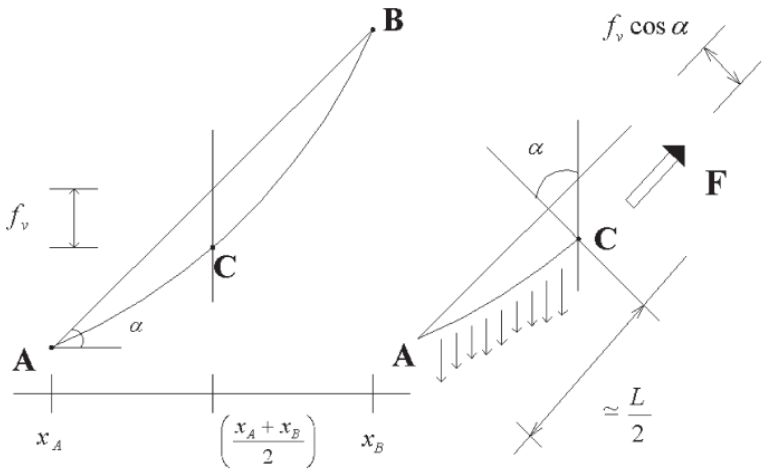

Figure 11 Virlogeux study of largest sag [3]

It is assumed that the deformed cable is parallel to the undeformed cable at point C. Point C is the middle of the span in the horizontal direction. Due to sag, this is not the middle of the cable in the vertical direction. Now a static equilibrium is calculated with respect to moments around the point A. This will give:

$$mg\frac{L}{2}\times\frac{L}{4}\times\cos\alpha\approx F\times f_v\times\cos\alpha\quad\therefore\quad f_v\approx\frac{mgL^2}{8F} \tag{9}$$

And with the relationship from vertical forces from both ends, it is known that, at mid-span:

$$H = F\times\cos\alpha \tag{10}$$

Where $H\ [N]$ is, again, the constant horizontal force in the cable.

Cardoso (2013) approach is using a parabola to discretise the cable, instead of the hyperbolic trigonometric functions. This will ease the calculations by a fair amount.

The error prediction will be calculated for some specific cases to showcase when this simplification is valid.

First, the function for the parabola must be study. Back to Equation 6, however, this time it is assumed that $\left(\frac{dy}{dx}\right)^2 = 0$, when in comparison to the unity, for small sag. Then:

$$H\left(\frac{d^2y}{dx^2}\right) = -mg \tag{11}$$

However, we have from Equation 4:

$$H\left(\frac{d^2y}{dx^2}\right) = -mg\frac{ds}{dx} \tag{12}$$

Which means that:

$$\frac{ds}{dx} = 1 \tag{13}$$

Therefore:

$$y = \frac{mgl}{2H}x\left(1-\frac{x}{l}\right) \tag{14}$$

Checking the error involved in the simplified parabola function.

The procedure will be to calculate sag using the parabolic function and the sag using the catenary function. The cable will be divided in 100 evenly spaced cross sections, sag will be calculated for all of them. For every cross section the error between parabola and catenary will be calculated using Equation 15. Different axial forces will be used to show that when the axial force is low, the error can be high, but when the axial force is high, the error can be neglected. Only the largest error of each axial force will be presented in Figure 12.

$$error = \left|\frac{y(x)_{parabola} - y(x)_{catenary}}{y(x)_{catenary}}\right| \tag{15}$$

Data: rupture stress of $175\ kN/cm^2$, axial forces will be a percentage of the rupture force, ranging from 2% up to 20%. Both cable end points are at the same height, no additional weight

is added to the cable, meaning that there is no protective pipe or other appliances that would increase the vertical load. Cable length is 100 m. Density of steel is 7850 kg/m^3.

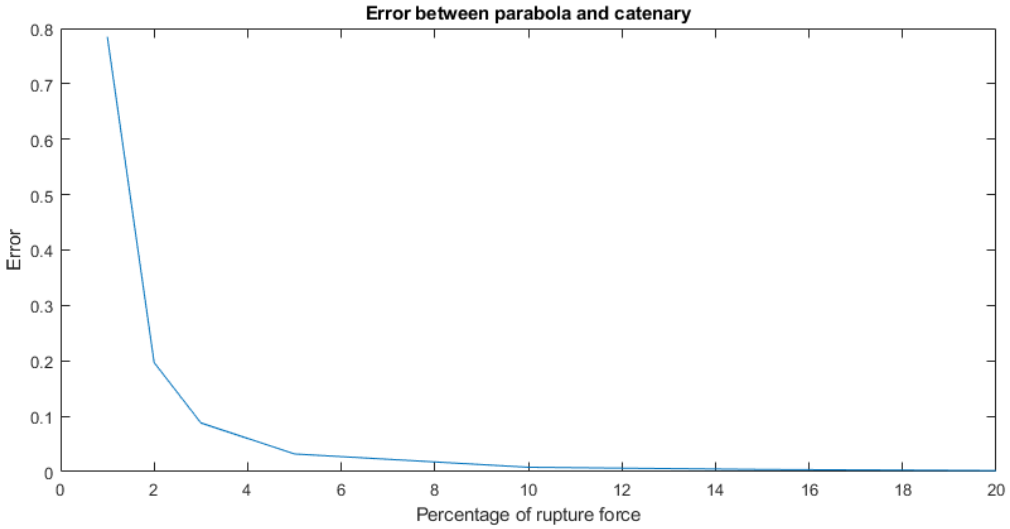

Figure 12 Maximum sag error when simplifying the function for the curve of the cable

Stay-cables, however, are inclined and therefore the vertical position of the end points can alter the results. The solution studied by Podolny, et al, 1976, is for the catenary:

$$L^2 = h^2 + 4\left(\frac{H}{mg}\right)^2 \sinh^2\frac{mgl}{2H} \qquad 16$$

where L $[m]$ is the total length of the curve, h $[m]$ is the height between the two endpoints, and l $[m]$ is the horizontal distance between the two endpoints.

For the parabola assumption the equation is as follows:

$$L = \frac{1}{cos\theta}\left(1 + \frac{8}{3}\left(\frac{mgl^2}{8H}\cos^2\theta\right)^2\right) \qquad 17$$

Where θ is the angle between the two endpoints and the horizontal line.

The knowledge of the total length is particularly interesting for the study of the effective rigidity of the stay cable, since the displacement between the two endpoints is not the same as the incremental length of the cable, due to the non-linearity of the geometry.

2.3.2 Cable mechanical properties

The advance in material technology regarding the steel has its importance in the record-breaking spans. For example, the Akashi Kaikyo Bridge has the main cable made of an improved tensile strength steel [1].

Some of the important parameters for an accurate model of the structure and a safe design are modulus of elasticity, ultimate tensile strength, total elongation of rupture, stress at the limit of proportionality.

Values for relaxation, and fatigue strength are important to ensure the long service life of the structure, typically the design life is 50 years. The potential hysteresis of helical wired cables can mean an increase in the damping of the cable, whereas a parallel wire cable shows a lower damping ratio.

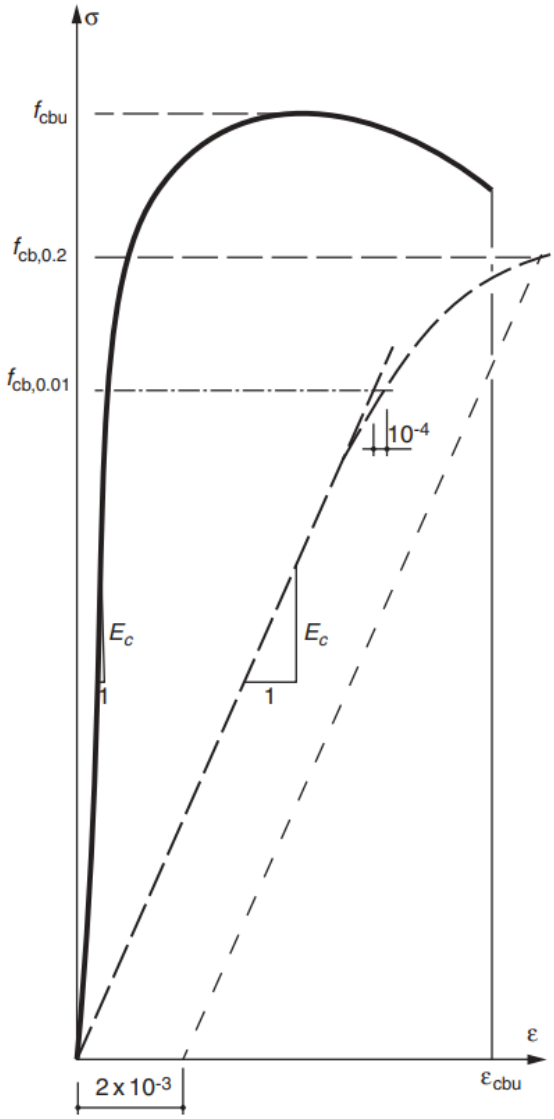

Figure 13 Stress-strain diagram, dotted line has a ten times larger horizontal scale [1]

It can be seen in the solid line of Figure 13 that the low-alloy steel used for the cables does not show a horizontal plastic plateau and the deformation at rupture is smaller than the structural steel [1].

2.4 Wind-cable interaction

Wind loading is important in the design of slender structures. Several parameters must be defined in order to have full understanding of the interaction between the air and the structure.

2.4.1 Reynolds number

The Reynolds number (Re) is a parameter that describes the flow pattern of a fluid around an obstacle. It is calculated as the ratio between the inertia forces and the flow forces. At low Re the flow is laminar and at high values it is turbulent.

For the wind passing around a cylinder the Reynolds number is calculated as:

$$Re = \frac{UD}{\upsilon} \tag{18}$$

Where $U[m/s]$ is the mean wind velocity, $D[m]$ is the cylinder diameter and $\upsilon[m^2/s]$ is the air kinematic viscosity, which is $1{,}5 * 10^{-5}\ m^2/s$ at a temperature of $20\ °C$ and pressure of $1\ atm$. Reynolds number is, therefore, dimensionless.

For smooth cylinders in laminar flow, the critical Reynolds number is between $1 * 10^5$ and $5 * 10^5$.

2.4.2 Scruton number

The Scruton number (Sc) is a parameter relevant for structures susceptible to vortex-shedding-induced vibration, which is the case of stay cables.

$$Sc = \frac{2\delta_s m}{\rho D^2} \tag{19}$$

where δ_s is the logarithmic decrement damping, m $[kg/m]$ is the linear mass of the cylinder, ρ $[kg/m^3]$ is the air density, and D $[m]$ is the across-flow dimension (cylinder diameter). Scruton number is, therefore, dimensionless. For a simplified check, if $Sc > 10$ then vortex induced vibration should not be a concern [10]. Therefore, an increased mass or damping will likely reduce the chances of wind induced vibrations.

2.4.3 Strouhal number

The Strouhal number (St) is a parameter that specifies the vortex shedding frequency. The definition is set as follows.

$$St = \frac{f_s D}{U} \tag{20}$$

Where f_s $[Hz]$ is the vortex shedding frequency, D $[m]$ is the across-flow dimension (cylinder diameter) and U $[m/s]$ is the mean wind velocity. Strouhal number is dimensionless. When the body being studied is a cylinder, it is known that $St \approx 0.2$ for subcritical flow [11].

2.4.4 Wind kinematics

Wind is a natural phenomenon and, therefore, it will show a significant randomness, over time and position, in terms of the magnitude and direction. However, it is possible to study it in the statistical sense.

The wind velocity can be separated into the mean wind velocity, which is usually an average of 10 minutes up to 1 hour of data, and turbulent part, which is time varying.

The so-called atmospheric boundary layer is the lowermost region where the friction between the moving air and the terrain plays a major role. This part can be quite short for low roughness terrain such as a calm sea, or very tall for a high roughness terrain like a mountainous forest. Above the boundary layer is the free troposphere, which is not of interest for civil structures such as bridges, because it only happens far above even the tallest buildings.

Within the boundary layer, the mean wind speed profile can be described by a logarithmic law, specially in strong wind conditions [10].

The formula can be expressed in several ways, e.g. as:

$$\bar{U}(z) = \frac{u_*}{k}(\ln z - \ln z_0) = \frac{u_*}{k}\ln\left(\frac{z}{z_0}\right) \qquad 21$$

where z $[m]$ is the height from the ground, u_* $[m/s]$ is the frictional velocity, k is the von Karman's constant with the experimentally found value of 0.4, z_0 $[m]$ is the roughness length of the terrain.

Friction velocity is a way to re-write the shear stress of the layers in terms of velocity, it is calculated as:

$$u_* = \sqrt{\frac{\tau}{\rho}} \qquad 22$$

Where τ $[N/m^2]$ is the shear stress and ρ $[kg/m^3]$ is air density.

Another formulation is the "power law". Even though it has no theoretical background, it gives values similar to the logarithmic law and it is easier to integrate, which can be helpful in many applications.

$$\bar{U}(z) = \bar{U}_{10}\left(\frac{z}{10}\right)^{\alpha} \qquad 23$$

Where $\bar{U}_{10}$ $[m/s]$ is the mean wind velocity at height $z = 10m$, α is a factor that changes with terrain roughness and the range of heights at which the wind is being studied.

$$\alpha = \left(\frac{1}{\ln\left(\frac{z_{ref}}{z_0}\right)}\right) \qquad 24$$

Where z_{ref} is the reference height. The reference height is chosen to be the height at which the power law and the logarithmic formula match. It is defined by the user, it can be at the mid height of the structure being analysed, for example.

The time variant part of the wind is called turbulence, which is three dimensional by nature. It is decomposed with reference to the main wind direction into the longitudinal (u), lateral (v) and vertical (w) component. The longitudinal has the largest magnitude and will be the only one further mentioned. A compact measure of the turbulence is its standard deviation, σ_u. It is known that near the ground the value for σ_u can be approximated by $\sigma_u = 2.5\, u_*$ [12].

It is not convenient to measure the gustiness of the wind using a parameter that has dimension, therefore another parameter can be used to more precisely compare to wind data with different magnitudes, the turbulence intensity.

$$I_u = \frac{\sigma_u}{\bar{U}} \tag{25}$$

When using the Equation 21 and $k = 0.4$ yields:

$$I_u = 2.5\,\frac{u_*}{\frac{u_*}{0.4}\ln\left(\frac{z}{z_0}\right)} = \frac{1}{\ln\left(\frac{z}{z_0}\right)} \tag{26}$$

2.4.5 Wind forces

In a wind field, different surface pressures arise around the structure, creating the resultant forces on the structure. Friction on the surface also adds a minor component to the wind loading. This phenomenon depends on many factors that will be mentioned below.

Drag force is present in most fluid-structure interaction. It has the same direction of the wind and can be defined as follow:

$$F_D = \frac{1}{2}\rho_a \bar{U}^2 D C_D \tag{27}$$

where ρ_a $[kg/m^3]$ is the air density, D $[m]$ is the relevant across-wind dimension (for cylinders it would be the diameter) and C_D is the drag coefficient which can be found experimentally. The formula above is per unit length, commonly used for long element such as long cylinders.

Lift forces is the force perpendicular to the mean wind direction and it appears in most cases. It might not happen in a perfectly round cylinder, because the lift force is the integral of pressures above and below the chord line. Therefore, a perfectly round cylinder will show equal pressures above and below the chord line.

$$F_L = \frac{1}{2}\rho \bar{U}^2 D C_L \tag{28}$$

where C_L is the lift coefficient, which can be found experimentally. On cylinders/cables in operation, the mean lift coefficient can be different from 0 in the absence of full rotational symmetry, pollution or rain droplets on the cable surface and/or in the critical Reynolds number range.

Lift and drag coefficient are unique to each object shape and may have different values for different angles of attack and different Reynolds number, since those two parameters might change the flow around the bluff body.

The sum of drag and lift force on the body might not be acting at the shear centre, therefore, an overturning moment might appear, as typical in case of elongated shapes such as bridge girders.

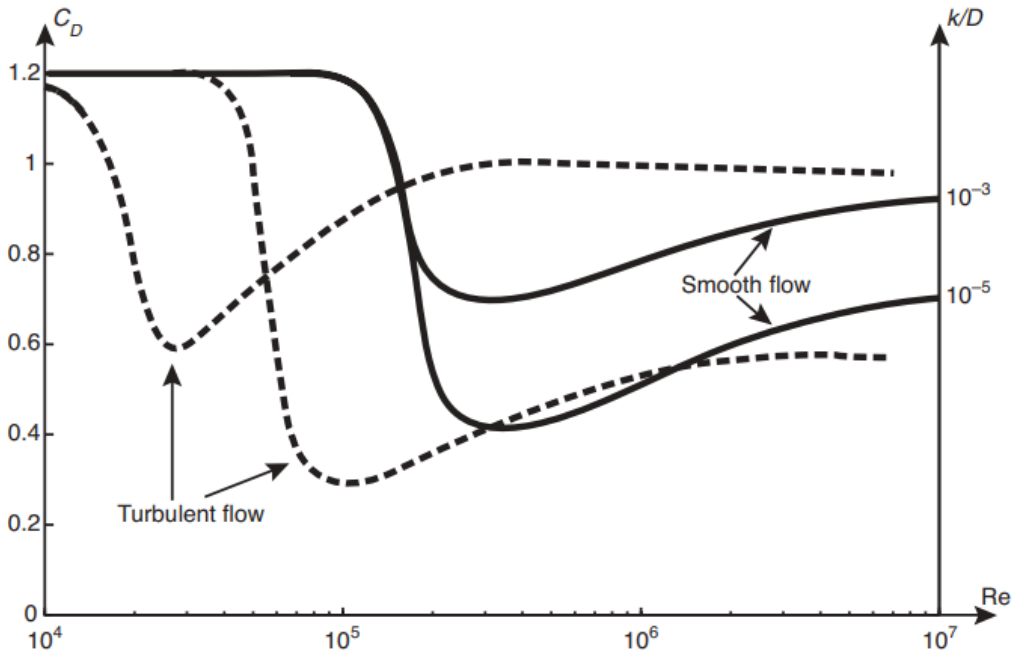

Figure 14 Drag coefficient for a cylinder [1]

2.4.6 Buffeting

Buffeting is a mechanism by which the change in the wind velocity and/or direction cause the structure to vibrate. This is a self-limiting phenomenon, so no catastrophic displacements can occurs, however, this can lead to durability issues if it happens during the lifetime of the structure, and serviceability can also be affected [1]. High turbulence intensity might lead to high buffeting, since this means that the wind velocity changes more.

2.4.7 Vortex induced vibration (VIV)

Depending on the flow conditions, an alternating vortex-shedding might occur in the separating shear layers into the wake of a bluff body. This alternate vortex shedding can induce the

structure into a across-wind vibration. With higher turbulence intensity the vortices get less consistent.

Vortex-shedding is self-limiting by its nature, because larger amplitudes decrease the synchrony of frequencies from upper and lower surfaces. That is why this mechanism is not of catastrophic nature, but can be of concern regarding durability and serviceability.

The critical wind velocity regarding vortex-shedding is defined as:

$$U_{cr} = \frac{f_i D}{S_t} \tag{29}$$

where f_i $[Hz]$ is the eigenfrequency of the structure, D and S_t are defined in 2.4.3.

2.4.8 Wake induced vibration

When two bodies are close enough to each other in the direction of the mean wind speed, the second body can be at the wake of the first. The disturbed flow past the upstream body can create different unfavourable pressures on the downstream body. This phenomenon is overall called as wake effect and can cause large vibrations. This happens, usually, at high wind velocities.

According to [10], a formula to predict the critical wind velocity that might set a cable into wake galloping can be described as follows.

$$U_{crit} = cfD\sqrt{S_c} \tag{30}$$

Where c is a constant, f $[Hz]$ is the natural frequency of the cable prone to galloping, D $[m]$ its diameter and S_c the Scruton number.

The constant c has the value of 25 for cables at a distance of $2D$ up to $6D$, or a value of 80 for distances above $10D$. For a distance in between the value above, $c = 40$ can be used.

2.4.9 Rain-wind induced vibration

Rain-wind-induced vibrations (RWIV) are not entirely understood, it is a subject still being researched. It is believed, due to observational and experimental evidence, that the phenomenon occurs when either one or two water rivulets are created along the cable. Those rivulets can change the shape of the cable, thus changing lift and drag coefficient, along with other parameters. These changes can lead to initiation of galloping. The wind velocity required is between 5 and 18 m/s, mainly on smooth cables that have low damping and inclined in the direction of the wind. The frequencies that are excited are between $0{,}5$ and $3{,}3$ Hz [1].

The magnitude of rain, in order to occur RWIV, is a light to moderate rain fall of around 1 to 10 mm/h, outside this range the water rivulets might not be consistent [1].

2.5 Cable dynamics

Stay cables are slender structure with low mass and low damping. The low flexural rigidity coupled with nominally pin supports leads to a structure that behaves as a taut string, where the stiffness is a function of the applied axial force. This setup makes for a likely vibration condition. Damping ratios can be at the order of 0.05% to 0.5% [13].

An idealised taut string model can show infinite natural frequencies and the formulation is as follows:

$$2\pi f_n = \omega_n = \frac{n\pi}{L}\sqrt{\frac{T}{m}} = \sqrt{\frac{k}{m}} \quad \{n \mid n \in \mathbb{N}^*\} \tag{31}$$

Where n is the mode being studied, f_n $[Hz]$ is the natural frequency for mode n, ω_n $[rad/s]$ is the natural frequency for the mode n, L $[m]$ is the length of the string, T $[N]$ is the tension force and m $[kg/m]$ is the mass per unit length.

The mode shape corresponding to the above natural frequency is.

$$W_n(x) = A_n \sin\frac{n\pi x}{L} \quad \{n \mid n \in \mathbb{N}^*\} \tag{32}$$

Where A_n $[m]$ is the vibration amplitude which depends on the initial conditions.

Ultimately, the free vibration of an undamped taut string is

$$w(x,t) = \sum_{i=1}^{n} A_n \sin\left(\frac{n\pi x}{L}\right) \sin\left(t\frac{n\pi}{L}\sqrt{\frac{T}{m}}\right) \tag{33}$$

2.5.1 Inducing cables into vibration

All the vibration causes mentioned in 2.4 are of concern for Bybrua.

Buffeting might occur if the wind properties vary in a way that match the cable dynamics.

Vortex shedding can be a problem if the wind velocity is near the critical wind velocity. Bybrua's cables do not show the surface treatment that could help mitigate this vibration cause, this is discussed in 2.6.

Wake induced vibration can be of concern, because of the arrangement of the cables. Each cable is made of 4 individual smaller cables that are just a few diameters apart. The vortices shedded by the upwind cable can induce de downwind cable into vibration.

There is reason to believe that the largest vibrations in the cable of Bybrua happens due to RWIV [2].

Parametric excitation is another cause for vibration. It consists of motion of at least one of the cable anchorages. If the excitation comes from the lower anchorage, it is usually due to traffic dynamics or the wind forces acting at the deck. If the excitation comes from the top anchorage,

it can be from wind forces on the tower or earthquake accelerations. There can be other combination of factors that might lead to parametric excitation.

2.6 Mitigation of wind forces

According to [10] regarding the mitigation of rain-wind induced vibration, the minimum is to provide a surface treatment to the cable in order to avoid the upper rivulet forming during moderate rain. Examples of this surface treatment can be seen at Figure 15. This would decrease the wind forces on the cable due to RWIV.

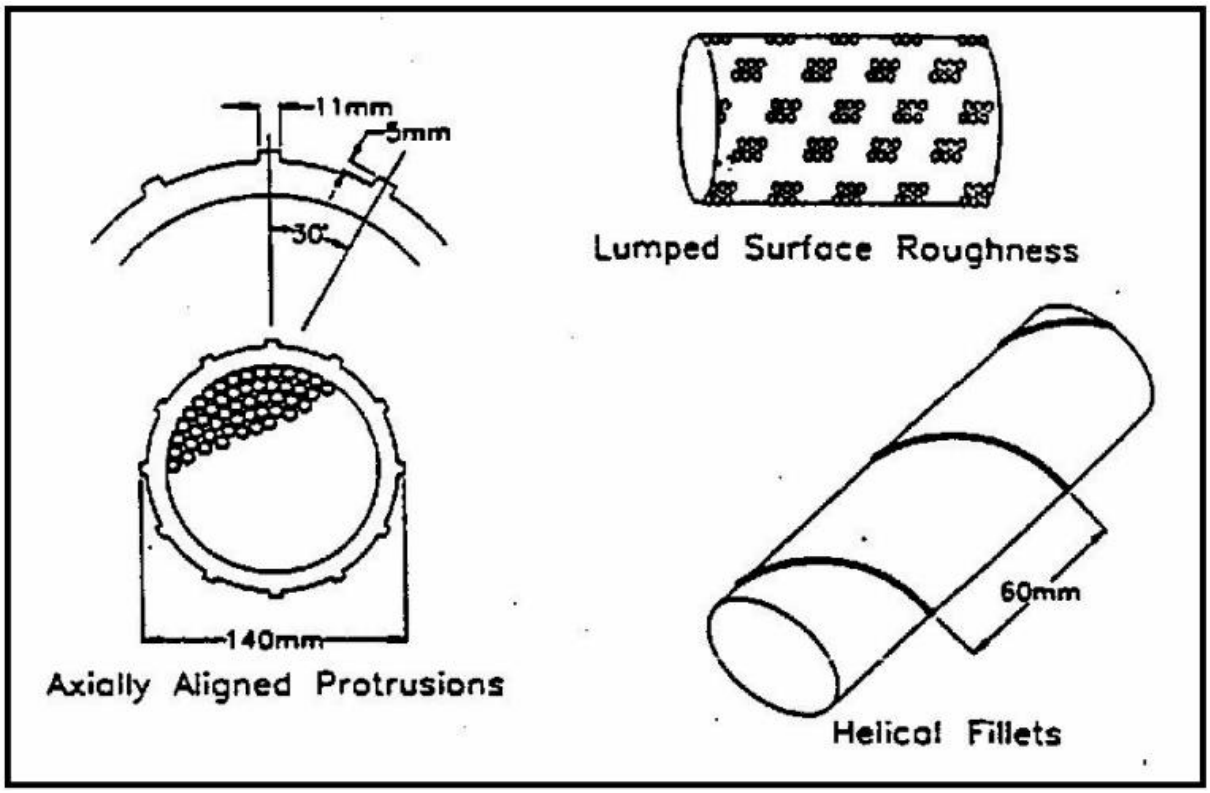

Figure 15 Cable surface treatments to reduce rain-wind induced vibrations [10]

Bybrua, however, does not have this treatment. It is a locked coiled cable with smooth surface without any rivulet breaking.

One option would be to wrap the cable with a special tape that would provide the helical fillet like a pipe with that feature, however this would be a cost demanding procedure with constant maintenance, since the tape would eventually tear off [10].

Another option would be whirling a helical wire around the cable [14], which can be made of stainless steel and thus much less maintenance needed. There are many solutions to securely attaching the wire to the cable. What was done in Akashi-Kaikyo Bridge, is that the wire was whirled around the cable while some tensile force was applied, then the wire was secured in both ends of the cable. The tensile force on the wire is what keeps it from flapping on the wind.

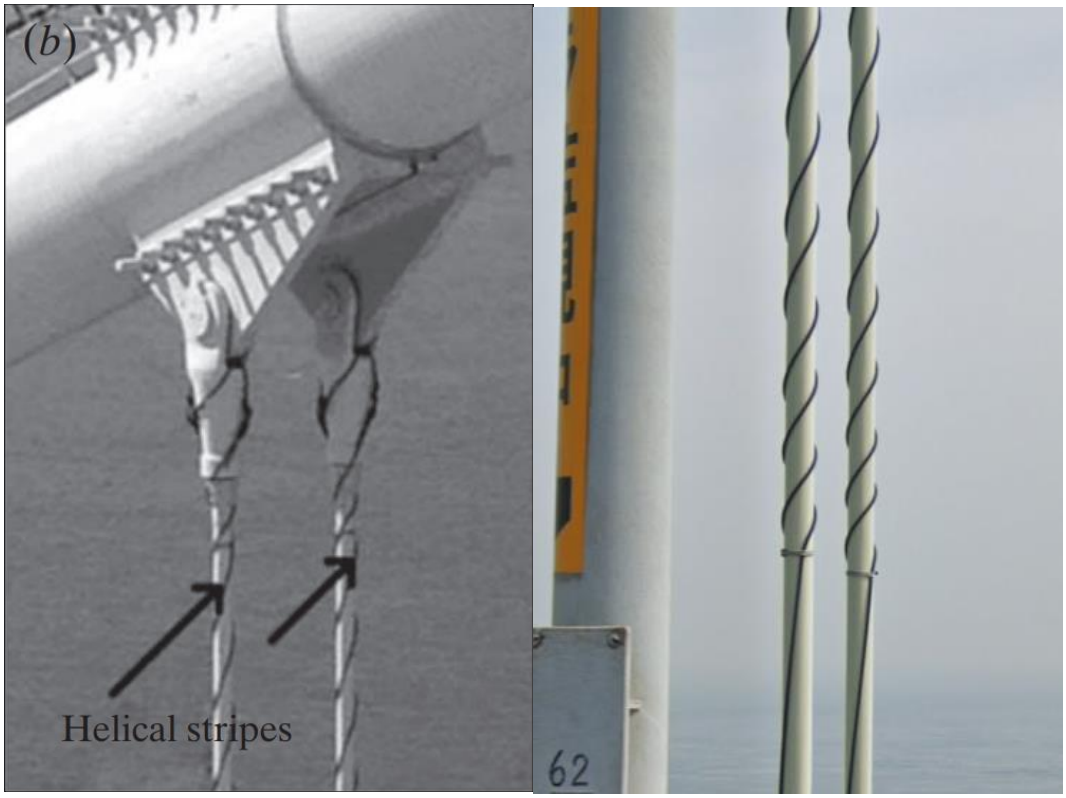

Figure 16 Helical wire around a hanger at Akashi-Kaikyo Bridge. [14] [15]

Another option would be the installation of a split pipe with the required helical fillet. The two halves of the pipe would be place around the cable and secured together according to manufacturer specification. This solution would prevent the water rivulet from forming and thus minimizing the rain-wind induced vibration. The installation process can be expensive, and the upper part of the cable is difficult to access. However, this solution would not require constant maintenance and the traffic would not have to be entirely interrupted.

Figure 17 Cross section of two half pipes intended to be added on existing cables [16]

2.7 Damping of cable vibration

Stay cables have very low damping coefficients, they can be quite similar to a string in a musical instrument, once the string is plucked it takes quite some time for it to come to a rest. Damping ratio can range from 0,05% to 0,5% [13] or 0,01% to 0,2% [3], depending on the cable itself and if there is any injection inside the pipe to help dissipate energy.

Bybrua does not have a pipe in which an injected material with form a bond between the cable and the pipe and increase the energy dissipation, so the damping ratio is expected to be in the low range mentioned above. The added mass of a pipe plus, for example, grouting would increase the Scruton number (2.4.2). It is known that most types of wind-induced vibrations tend to be mitigated by a higher Scruton number. [10]

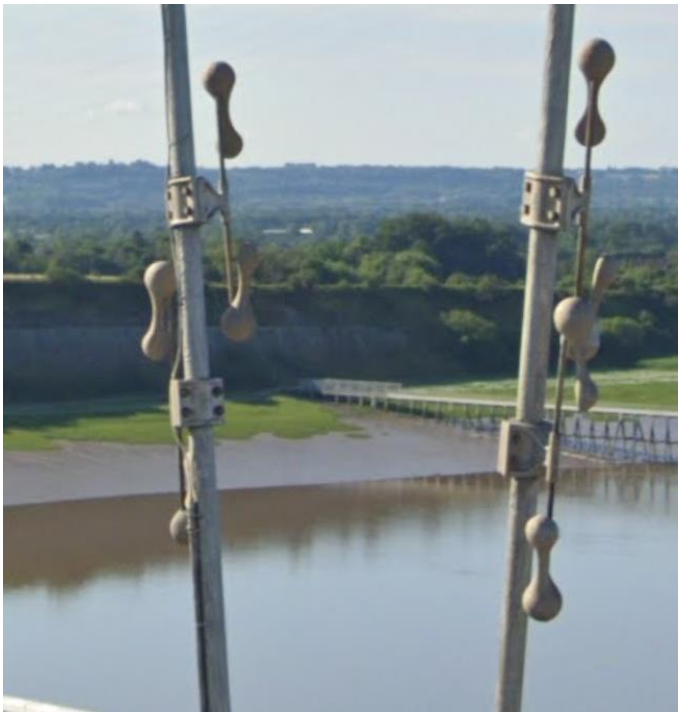

Figure 18 Severn Bridge damping system [15]

A Stockbridge damper is a type of tuned mass damper that is widely used in long transmission lines to avoid excessive vibration in those cables. This method has been also used in cable-stayed bridges and suspension bridge with success. Examples are Severn Bridge and the backstay of the London Eye, both in the United Kingdom. It consists of a mass that is carefully chosen to vibrate instead of the bridge cable itself. The rod attaching the mass to the support is of a specific cable that damps the motion due to the strand's friction between each other. Several minor variations are available due to patents. Some show different motion of the mass, for example a twisting motion, allowing damping in more than one plane.

The size of the damper would have to be carefully chosen due to the fact that, in Bybrua, there are cables bundled up in groups of four, which would mean that a Stockbridge damper on the top cable could hit the bottom cable. The distance between the cables can be as low as 41 cm.

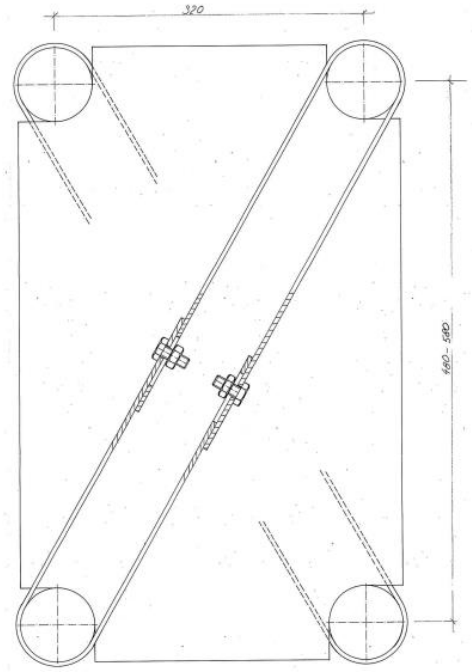

Figure 19 Cross section of the cable bundle, it is shown the distance being between 480 to 580 between cable centres [17]

When groups of cables are bundled together there could be another type of damper possible, it is a friction damping system that tie all the cables in the bundle together.

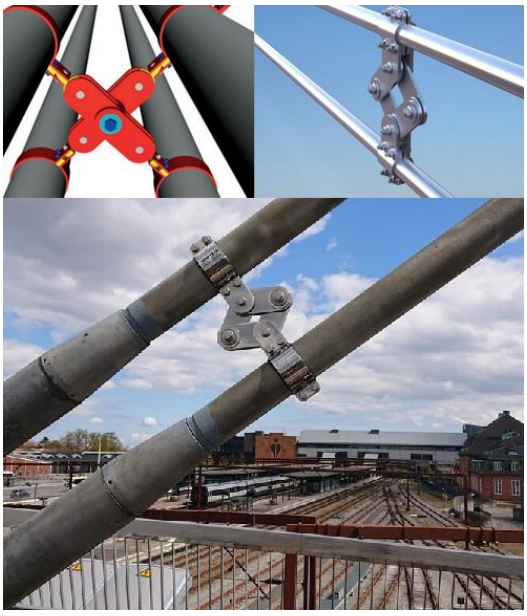

Figure 20 Friction damping between two or more cables [18]

In Figure 20 can be seen that the system is a mechanism, therefore movement is expected. However, the tighter the bolts are, the more resistant the system will show to a given movement,

that is the concept of this damping system. The location of this damping system must be carefully chosen, because as many other dampers, an initial threshold force must be overcome before the system works at all, this might lead to a fixed node in the cable instead of the desired damping, if the initial threshold is large [10].

In Bybrua the way the individual cables are bundled together do not represent any major damping contribution. It might only help to prevent vibration of a single cable, acting as a node for the single cable at the connection point.

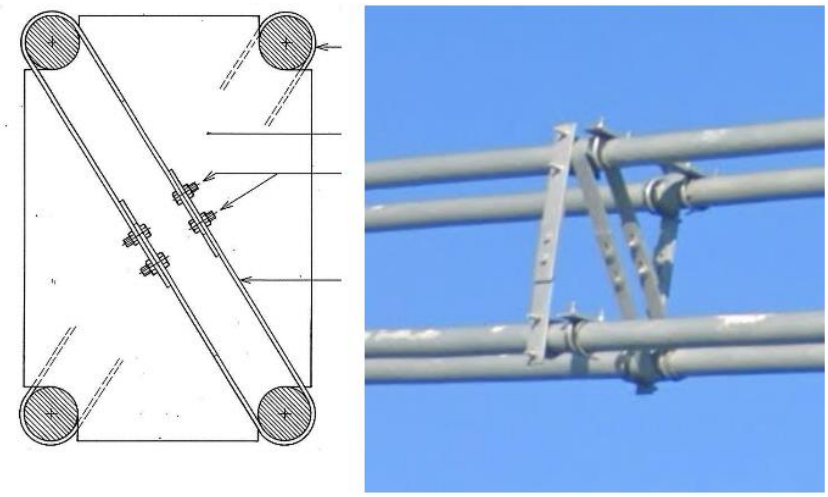

Figure 21 Bybrua cable bundle [17] [15]

Another possible solution is a viscous damper linking the cable to the deck. This proves to be an interesting solution for the design of a new bridge, however quite impractical for a retrofit because it will prove to be much more expensive, architecturally invasive and difficult execution. Most of this happens due to the need for the installation of the supporting structure.

Figure 22 Russky bridge damper [15]

Crosstie is another solution for diminishing the cable vibration. It consists in tying two or more cables to each other and, sometimes, ultimately to the deck. This solution increases the stiffness of a single cable in the vertical plane and will change the vibration mechanics of the cable since it has now a vertical constrain. This solution is more interesting for newer bridges that show many cables instead of the older structures that has fewer stronger cables (like Bybrua).
This constrain of a cable might mean that the lower modes are more difficult to excite due to a node being added.

Figure 23 Crosstie example [10]

3 Case study – Bybrua

Bybrua was built to connect Buøy and Hundvåg to the continent. Those two islands are important due to their increasing population and Rosenberg Mek. Verksted, which is an important industrial centre. The islands Sølyst and Engøy were already connected to Buøy by older bridges, crossing the straits Engøysund and Pyntesund. So, a bridge connecting all those islands to the city centre was necessary [5].

Figure 24 Bybrua, connecting Buøy and Hundvåg to the city center [19]

A delegation from the municipality along with the consultant engineer went on an inspection of the many bridges along the Rhine river in Germany to see modern bridges with similar spans. The impressions made by the Severin bridge and Bendorf bridge were decisive for the choice, where the Severin bridge, a cable-stayed bridge had shorter deck giving an impression of more slenderness. Whereas Bendorf bridge Figure 3 is a balanced cantilever, has much taller cross-sections, being considered to appear too heavy and massive [5].

Figure 25 Severin bridge [15]

By choosing a cable-stayed bridge, the channel below the bridge was kept open to maritime traffic at its full width, since the asymmetrical tower was built near the north margin of the channel. A cantilevered concrete bridge spanning the whole channel would require a deck height of up to $9\,m$ near the support, which would have lifted the bridge deck and possibly reduced the navigation height [5].

Figure 26 Panoramic view of Bybrua [20]

The bridge total length is $1067\,m$. There are 23 side span ranging between 40 and $42\,m$ and a mains span of $185\,m$. The tower is $70\,m$ tall and the deck is at $26\,m$ above sea level. The deck is made of prestressed concrete for all the spans but the main span. The main span is a single cell box girder in steel.

Figure 27 Steel box girder at the main span

Figure 28 Connection between concrete girder (top) and steel girder (bottom)

The cables at the north side of the bridge (the left part of Figure 26) are directly above the columns, this is because the short spans do not requite to be supported by the cable, but the tower still requires some balance in the horizontal forces, so it does not experience excessive bending moments. The cables on the north side act similarly to a backstay.

The tower is a hollow cross section of reinforced concrete. The construction was carried out with slip forms. There is an inclination of 9° of the tower legs. The foundation of the tower is on rock. There is a protection against ship collision using rock filling.

The concrete deck has fire protection because it passes above many wooden houses and oil storage tanks. This protection is achieved with extra concrete layer and skin reinforcement [5].

3.1 Instrumentation

The instrumentation of the bridge was carried out to understand better how the vibration is happening and trying to understand the causes.

Four wireless accelerometers were placed in the cables, one accelerometer in the bridge deck and one weather station to measure wind and rain.

3.1.1 Cable instrumentation

The cables are identified by a three letters name CXY, this nomenclature will be used throughout the document. X is the longitudinal designation of the cable, starting with number 1 being the northmost cable. Y is the transversal designation of the cable, where it is called either W, for the west side of the deck or E, for the east side of the deck. The accelerometers are placed 4 m above the bridge deck.

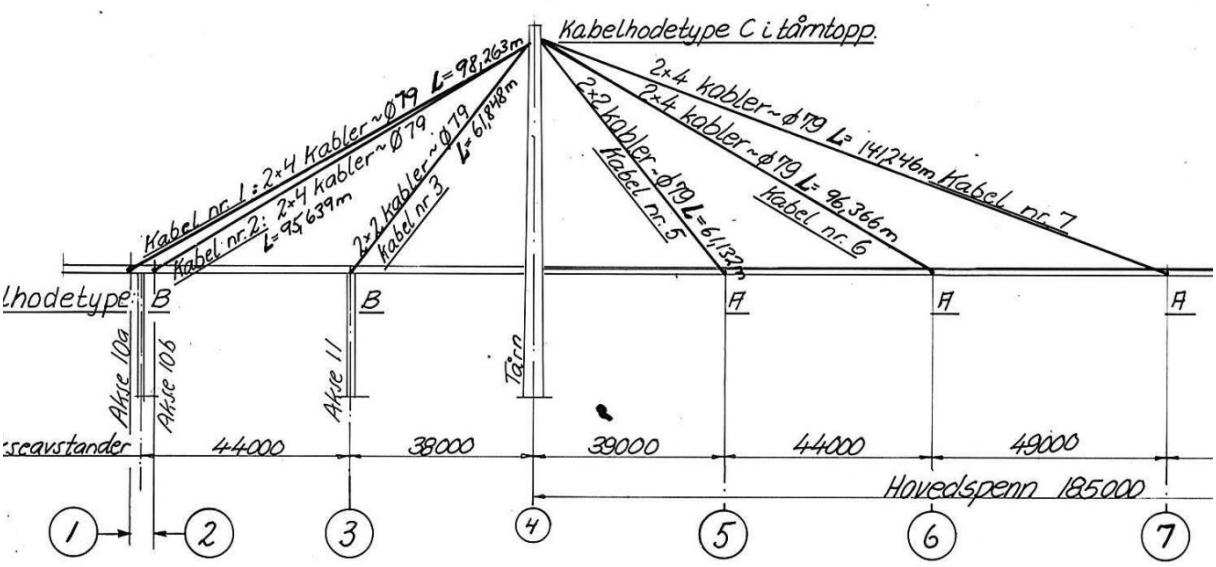

Figure 29 Longitudinal designation of the cable, from left to right, cables C1, C2, C3, C5, C6 and C7 [17]

The accelerometers used are G-LINK-200, they are battery powered and weather resistant [21]. It was chosen an accelerometer with small dimensions to minimize the change in geometry of the cable due to the added accelerometer. All four accelerometers used are identical, they will, therefore, be identified by their serial number (4251, 12045, 12046 and 12047).

Figure 30 Sensor on the cable bundles until 20/04/2021 [2]

Cable bundles C1E, C1W, C2E and C2W were monitored using a tri-axial wireless accelerometers until 20/04/2021 (see Figure 30). Cable C1E was showing the largest vibration amplitudes of all the cables monitored [2], therefore, after 20/04/2021, all the sensors were attached to C1E. Sensor 12046 was malfunctioning, therefore it was no longer used. The location of each sensor in C1E after 20/04/2021 can be Top or Bottom, Roadside or Seaside. Figure 31 shows the cable bundle and Table 2 the position of each sensor.

Figure 31 Sensors on the cable bundle after 20/04/2021

Table 1 Table of cable and sensors until 20/04/2021

Cable	Sensor
C1E	12046
C1W	12047
C2E	12045
C2W	4251

Table 2 Table of position within C1E and sensor after 20/04/2021

Position (C1E)	Sensor
Not used	12046
Top road	12047
Bottom sea	12045
Bottom road	4251

3.1.2 Weather transmitter

There is a weather transmitter WXT530 from Vaisala [22] at 3.5m above the deck measuring horizontal wind velocity and its direction, relative humidity, temperature, rain intensity and pressure. The weather station is placed between the anchoring points of cables C1/C2 and C3 on the east side of the bridge deck.

Figure 32 Weather transmitter [15]

3.1.3 Bridge deck instrumentation

There are accelerometers inside the deck girder, one in the middle of the span between cables 2 and 3, another in the middle between the tower and cable 5. Those accelerometers are tri-axial CUSP-3D from Canterbury Seismic Instruments [23]. The accelerometer inside the bridge

deck is different than the cable because there was no requirement of size and weight when inside the deck.

Figure 33 Accelerometer inside the bridge deck

3.2 Natural frequency

The natural frequency is one of the most important parameters for a dynamic analysis of a structure, therefore this will be assessed. The forces in the cables are known from the original calculations, there is a maximum and a minimum force provided. With the force and cable properties it is possible to calculate the natural frequency.

It is also possible to determine the natural frequency of the cable by carrying out a spectral analysis of accelerations. When calculating the power spectral density of the accelerations, there should be peaks of the spectral density that correspond to the frequency of the natural frequency. With the natural frequency determined by spectral analysis, it is possible to calculate the axial force on the cable at the time of the recordings. This force should be between the minimum and maximum provided by the original calculations

3.2.1 Estimation of the eigenfrequencies

From the original drawings it is known that the cable diameter is $\phi = 79mm$. The drawings also give that the cable mass plus the anchorages is $4000\ kg$ for the cables being analysed.

There is no information regarding the cable weight itself.

Ca. kabelvekter

Kabel	nr. 1	ca	4,0 t	inkl.	hoder
"	" 2	"	4,0 t	"	"
"	" 3	"	2,7 t	"	"
"	" 5	"	2,7 t	"	"
"	" 6	"	4,0 t	"	"
"	" 7	"	5,6 t	"	"

Figure 34 Original cable weight table [17]

Considering that the cable is of a locked coil it is possible to infer what it is the mass when compared to industry's catalogue for this type of cable.

From a manufacturer catalogue [8] it is made the next table.

Table 3 Cable effective area [8]

Cable effective area, from Redaelli			
Nomimal diameter [m]	Total area [m²]	Effective area [m²]	%
8.40E-02	5.542E-03	4.805E-03	86.71%
8.00E-02	5.027E-03	4.358E-03	86.70%
7.60E-02	4.536E-03	3.933E-03	86.70%

Therefore, a locked coil cable with a diameter of $\phi = 79\,mm$ will give an effective area of $4250\,mm^2$.

The original calculation provides that the cross-section area used was $4272\,mm^2$. This will be the effective area used.

It is known that the cable does not have any outer pipe nor grouting, just a protective paint whose mass will be neglected. Therefore, the mass per unit length of the cable is calculated as.

$$A_{eff}[m^2] * 7850\ [kg/m^3] = 33{,}54[kg/m] \qquad 34$$

The cable length is as follows:

Kabelskjema

Kabel nr.	Antall	Kabellengde L i mm
1	8	98.263
2	8	95.639
3	4	61.848
5	4	61.132
6	8	96.366
7	8	141.246
Sum	40	

Figure 35 Cable length from original drawing [17]

For cable 2, the overall mass of the cable will be $3207\ kg$ which is lower than what is displayed in Figure 34, which also includes the mass of the cable anchorages.

The maximum tensile force in the cable is shown in the calculations as being $\frac{1395}{8}\ Mp$ (megapond) [24] which can be translated as being $1710\ kN$.

Using the formula Equation 31 and choosing $n = 1$.

$$2\pi f_n = \omega_n = 1 * \frac{\pi}{95.639}\sqrt{\frac{1710000}{33.54}} = 7.417 \ \rightarrow f_n = 1.180\ Hz \qquad 35$$

If considering only the permanent load (self-weight of the structures) the force would be $\frac{943}{8}\ Mp$ [24] which can be translated to $1156\ kN$.

$$2\pi f_n = \omega_n = 1 * \frac{\pi}{95.639}\sqrt{\frac{1156000}{33.54}} = 6.098 \ \rightarrow f_n = 0.971\ Hz \qquad 36$$

Those two values will be compared to the data collected by the accelerometers, as previously described. The values estimated from the recorded data should be in between the two frequencies calculated above.

The data gathered on 28/08/2019 between 08:00 and 09:00 was used in order to estimate the eigenfrequency. There was no precipitation and mean wind velocities of $8{,}3\ m/s$. The data consist of accelerations recorded at a sampling frequency of $64Hz$, therefore $1\ h$ of data corresponds to 230400 samples.

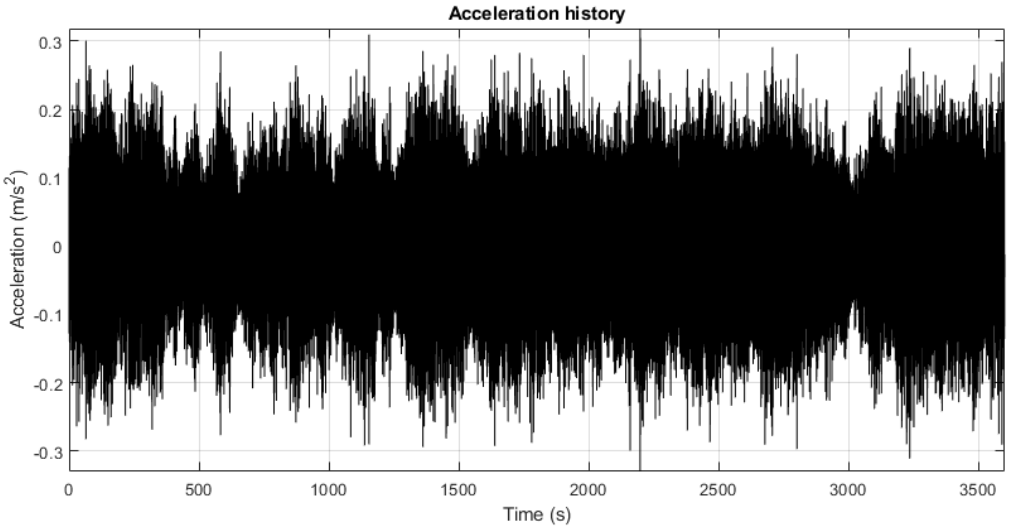

Figure 36 Acceleration history 28/08/2021 between 08:00 and 09:00. Cable C2E heave motion

In order to study the cable response as well as estimate the natural frequency, a spectral analysis in MATLAB [25], using Welch method, was carried out. The number of segments used was chosen to give a frequency resolution of $0.005\ Hz$. This means that for $1\ h$ long data set, 18

segments were chosen. The overlapping between two segments was chosen as 50% and a Hamming window.

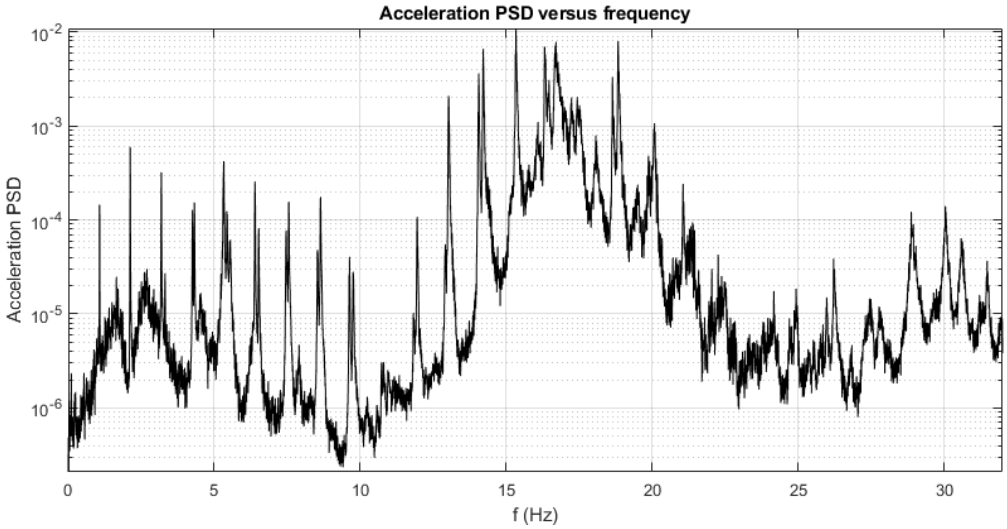

Figure 37 Acceleration power spectrum density for C2E heave motion

Using the assumption that the motion of the cable can be described as the sum of infinite cosine functions

$$x(t) = \sum_{i=1}^{N} A_i * \cos(\omega_i t + \phi_i) = \sum_{i=1}^{N} x_i(t) \tag{37}$$

Then the acceleration will be the second derivative of displacement

$$\ddot{x}(t) = \sum_{i=1}^{N} -A_i * \omega_i^2 * \cos(\omega_i t + \phi_i) = \sum_{i=1}^{N} x_i(t) * (-\omega_i^2) = \sum_{i=1}^{N} \ddot{X}_\iota * \cos(\omega_i t + \phi_i) \tag{38}$$

The displacement power spectrum reflects the displacement amplitude squared [26]

$$S_x(\omega_i) = \frac{1}{2} A_i^2 \, \Delta\omega_i \tag{39}$$

Similarly, the acceleration spectrum is

$$S_{\ddot{x}}(\omega_i) = \frac{1}{2} \ddot{X}_i^2 \, \Delta\omega_i \tag{40}$$

The properties of the Fourier transform and the spectra of the function derivatives [26], imply that the displacement spectrum relates to the spectra of the accelerations as:

$$S_x(\omega_i) = \frac{S_{\ddot{x}}(\omega_i)}{{\omega_i}^4} \tag{41}$$

This is consistent with the relationship between the displacement and the acceleration amplitudes:

$$\ddot{X}_\iota = -A_i * \omega_i^2 \qquad 42$$

Equation 41 shows that the acceleration power spectrum and the displacement power spectrum have the peaks at the same positions in the frequency axis, each are the natural frequencies. The displacement power spectrum gets very large for low frequencies, which can be a computational difficult to manage the values that get divided by low values of ω^4, also for the first value of the series, where $\omega = 0$.

Due to the large difference in magnitude along the series, it is a good practice to use logarithmic scale for the vertical axis.

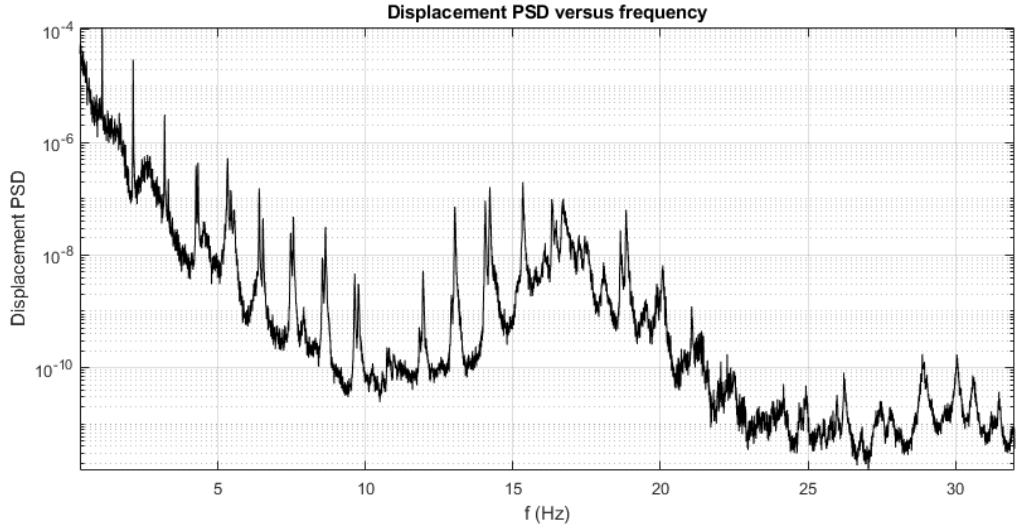

Figure 38 Displacement power spectrum density for C2E heave motion

From the diagrams of acceleration and displacement power spectral densities it above it is possible to obtain the eigenfrequency for the first mode of vibration. This is done by picking the value of the frequency for the first peak of the spectral density. The value for the first natural frequency is $f_n = 1{,}07\ Hz$. From the analysis using the forces from the original calculations, the first natural frequency should be $0{,}971\ Hz < f_n < 1{,}180\ Hz$. Therefore, the value of $f_n = 1{,}070\ Hz$ fits in the expected range.

From the above eigenfrequency is possible to infer what is the tensile force in n the cable at the time of measurement.

$$f_n = 1.070\ Hz \rightarrow 2\pi f_n = \omega_n = 1 * \frac{\pi}{95{,}639}\sqrt{\frac{T}{33{,}54}} \rightarrow T = 1405\ kN \qquad 43$$

Again, this force is within the expected range of minimum and maximum forces from the original calculations: $1156\ kN < T = 1405\ kN < 1710\ kN$.

The eigenfrequency for the subsequent modes, presented in 2.5 follows the equation:

$$f_n = \frac{\omega_n}{2\pi} = \frac{n}{2L}\sqrt{\frac{T}{m}} \quad 44$$

where n is the mode number.

Therefore, the second eigenfrequency should, theoretically, be twice the first and so on. When using measurements of full-scale models, the values can differ.

Table 4 Natural frequency for the first 5 modes, C2E

Natural frequency for the first 5 modes, cable C2E					
Mode	1	2	3	4	5
Frequency [Hz]	1.070	2.120	3.190	4.288	5.325

When calculating a linear regression of the values shown in Table 4, the value for $R^2 = 0.9999$ and a linear equation of $f_i = 1{,}068 * n + 0{,}005$. This shows that the values for natural frequencies of a stay-cable is very close to the taught string model assumed in 2.5. The idealised model does not account for sag, bending stiffness, damping and equivalent rotational spring of the anchorages.

The mode shapes, presented in 2.5, follow the equation

$$W_n(x) = A_n \sin\frac{n\pi x}{L} \quad 45$$

where n is the mode number.

The first three eigenfrequencies for all 4 cables monitored were estimated at both vibration directions, sway (lateral motion, perpendicular to the cable axis) and heave (vertical motion, perpendicular to the cable axis). The results are shown in Table 6.

Table 5 Channel and motion direction relationship

Channel	Direction
Ch2	Sway
Ch3	Heave

Table 6 Cable eigenfrequencies for the first 3 modes

One hour long data from 07:00 to 08:00 28/08/2019				
		Vibration mode		
Cable	Channel	#1	#2	#3
C1E	Ch2	1.025	2.055	3.143
C1E	Ch3	1.025	2.055	3.143
C1W	Ch2	1.040	2.075	3.173
C1W	Ch3	1.045	2.075	3.115
C2E	Ch2	1.065	2.120	3.190
C2E	Ch3	1.075	2.120	3.190
C2W	Ch2	1.050	2.100	3.160
C2W	Ch3	1.060	2.100	3.155

Table 6 shows the first three natural frequencies estimated for the four cables. It is possible to see that heave and sway vibration have similar natural frequencies, in some cases the estimated value is the same for both directions.

It is also possible to estimate how similar the forces in cables C1 and C2 are. The values for the frequencies are of the same order of magnitude, the average of $1{,}034\ Hz$ for cable C1 and $1{,}063\ Hz$ for cable C2. Cable C1 is $2{,}7\%$ longer, which would give a natural frequency of $97{,}4\%$ if all the properties stay the same between the two cable (including the axial force). The estimated natural frequency of C1 is $97{,}3\ \%$ of the one from C2. This shows that the tensile force in the cables C1 and C2 should be similar.

3.2.2 Cable curvature

With the new acquired knowledge of the existing force on the cable and using the equations shown in 2.3.1 it is possible to calculate the cable curvature using both the parabolic and catenary approach.

The calculation will be done for cable C2E because that is the cable that the axial force was calculated in 3.2.1, however, the same principal can be done for any other cable.

The tensile force on the cable is $T = 1405\ kN$, length $L = 95{,}639\ m$, mass per meter $m_l = 33{,}54\ kg/m$, gravity $g = 9{,}81\ m/s^2$.

The length of the cable will be divided into 100 parts, and the vertical displacement Δy will be calculated for all the parts.

The horizontal applied force H will be calculated using the angle θ between the two end points in relation to the horizontal line, such that

$$H = T * \cos(\theta) \tag{46}$$

Recalling the formulas for vertical displacement Δy.

Parabolic approximation will yield the following formula

$$\Delta y = \frac{mgl}{2H} x \left(1 - \frac{x}{l}\right) \tag{47}$$

And the catenary formulation will yield the following formula

$$\Delta y = \frac{H}{mg}\left\{\cosh\left(\frac{mgl}{2H}\right) - \cosh\left(\frac{mg}{H}\left(\frac{l}{2} - x\right)\right)\right\} \tag{48}$$

The results are a maximum sag of $0{,}2296\ m$ for both formulas used. The maximum sag is $2.9 * \emptyset_{cable}$ in

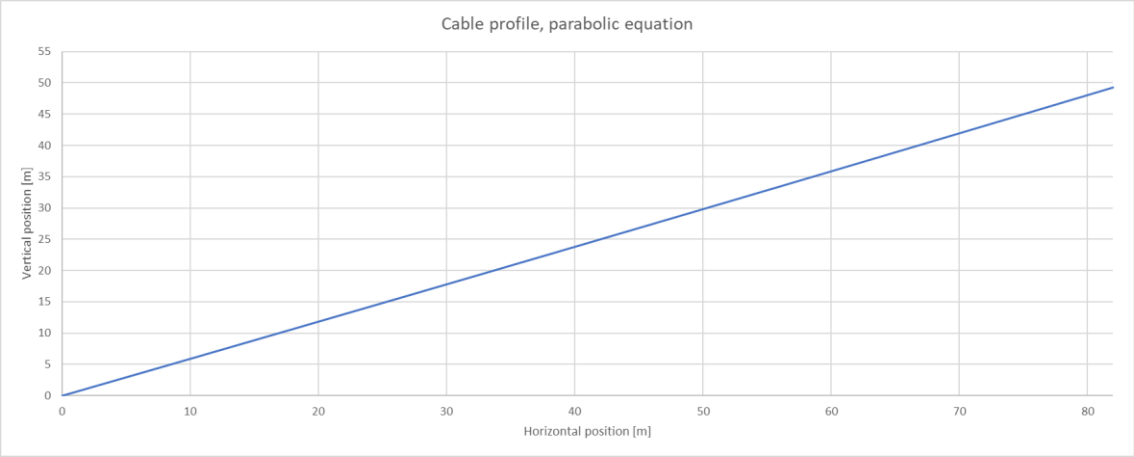

Figure 39 Cable profile considering parabolic approximation for sag

It is not visually possible to see the sag in Figure 39. This would only be visible at the cable when closely looking in the cable direction.

Just as a more visual demonstration, the following figure (Figure 40) will show the cable profile with the local sag Δy being multiplied by a factor of 50.

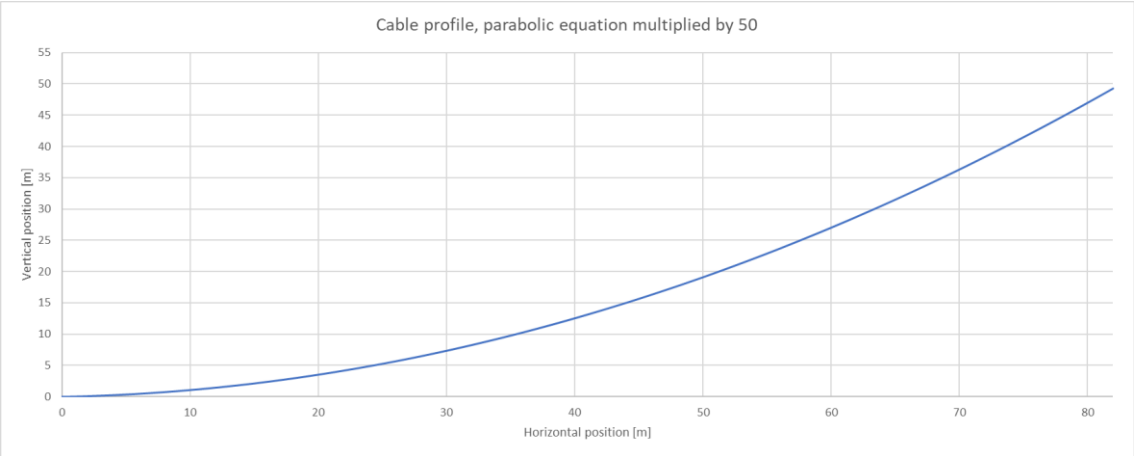

Figure 40 Cable profile considering parabolic sag multiplied by 50

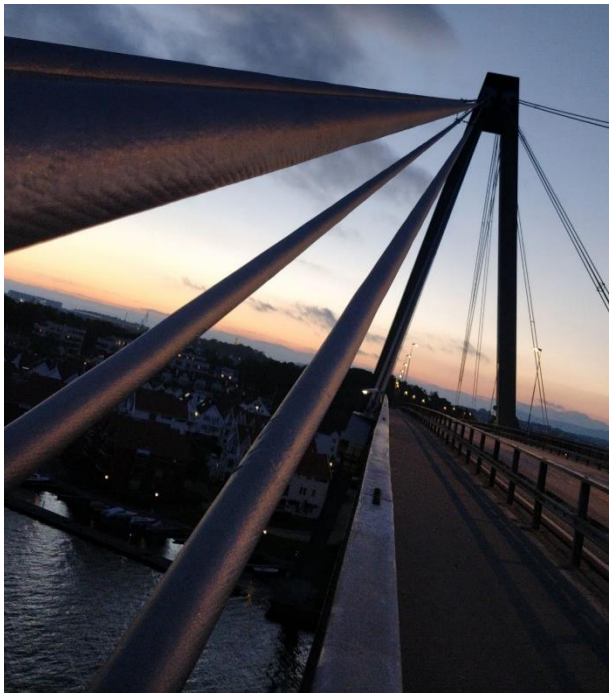

Figure 41 Visual observation of sag on the structure

Figure 41 shows the visual observation of the longest cable in Bybrua, cable C7. The picture was taken along its chord to make the sag more visible [1]. The low weight of the cable (the cable does not have a protective pipe or grout, that would have added weight) and the relative short length of the cable makes for a small sag that is barely visible. For comparison, Figure 42 shows a Stonecutters Bridge, the second longest span cable-stayed bridge when constructed. The long cables, up to $540\ m$ [27], show a larger sag than the shorter cable of Bybrua, cable C7 has $141{,}246\ m$ (Figure 29).

Figure 42 Visible sag on Stonecutters Bridge [1]

3.3 Estimation of damping ratio

Damping can be a difficult property to determine in civil engineering structures. Quite different than mechanical engineering systems where efficient dampers are introduced to reduce vibrations and then the system has a well-defined damping level.

In civil engineering structures, if a damper, like the ones showed in 2.7, is not used, it does not mean that the structure has no damping whatsoever. There is still friction, plasticity, wind drag and other mechanism that provide a certain level of energy dissipation, even without an added damping device.

Assuming that the cable damping can be modelled as linear viscous damping, two different types of acceleration data will be studied in order to estimate the damping: the free decay response (after initial pulling of the cable by a rope) and the ambient vibration data.

With the free decay response, an exponential function will be calculated as being the best fit for the envelope of the displacement response, then the damping ratio will be estimated by analysing the exponential function. The ambient vibration data will be analysed with Frequency Domain Decomposition and Random Decrement Technique.

3.3.1 Analysis of the Free Decay Response

On the 15/06/2021 the cable C1E was tested by introducing an excitation to the cable and then letting free vibrations occur. Since the test was not done in a lab, there is still wind loads and traffic loads, however, they were small when in comparison to the forces introduced to the cable at the test, therefore it is considered that the cable was under free vibrations. The mean wind velocity was $5{,}8\ m/s$ and there was no rainfall.

The cable was manually pulled, as it can be seen in Figure 43. This external force was used to record the free decay of the cable vibration. After pulling the rope shown in Figure 43 for a few second, until the cable was visually vibrating, the external force was interrupted and the cable was let to vibrate freely, while the accelerations being recorded by the three accelerometers shown in Figure 43 and explained in 3.1.1.

The external force applied was in the vertical plane. Even though there is acceleration in the horizontal plane, the results show to be less consistent. Therefore, only the heave motion will be analysed.

The acceleration records are displayed in Figure 44 to Figure 46.

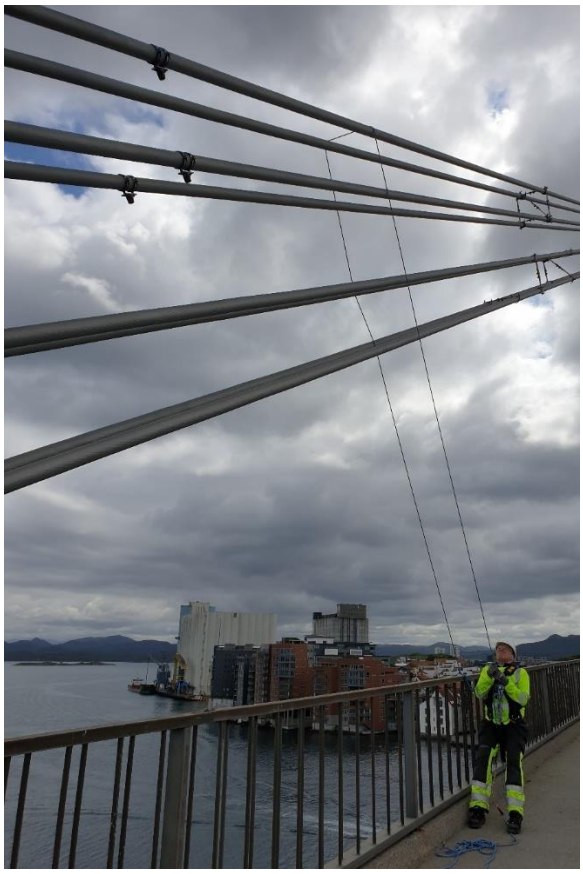

Figure 43 Manually pulling the cable. Photo by Jasna B. Jakobsen, UiS

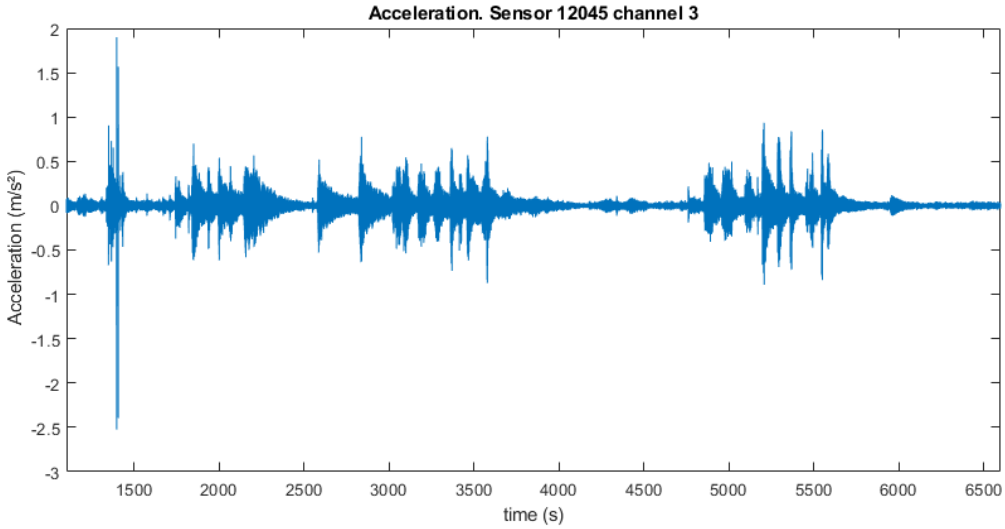

Figure 44 Acceleration records 15/06/2021. Sensor 12045 Heave motion

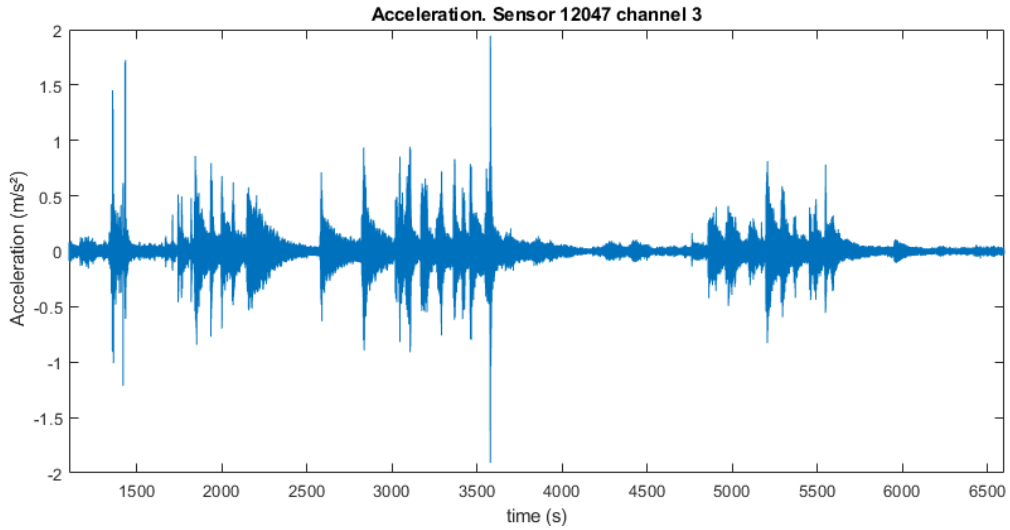

Figure 45 Acceleration records 15/06/2021. Sensor 12047 Heave motion

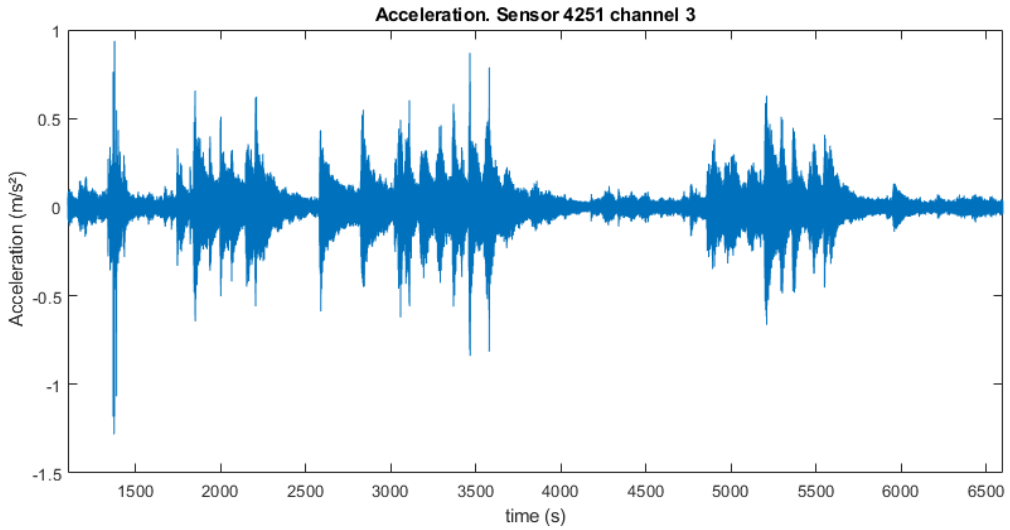

Figure 46 Acceleration records 15/06/2021. Sensor 4251 Heave motion

In the acceleration records above, it is possible to see the peaks of acceleration that happen when the external force is being applied to the cable. There are three windows between $t = 1100\ s$ and $t = 1900\ s$ that consistently show free decay response throughout the 6 diagrams. Those three windows will be used to estimate the damping ratio of the structure. Figure 47 shows a close-up of the three windows mentioned above.

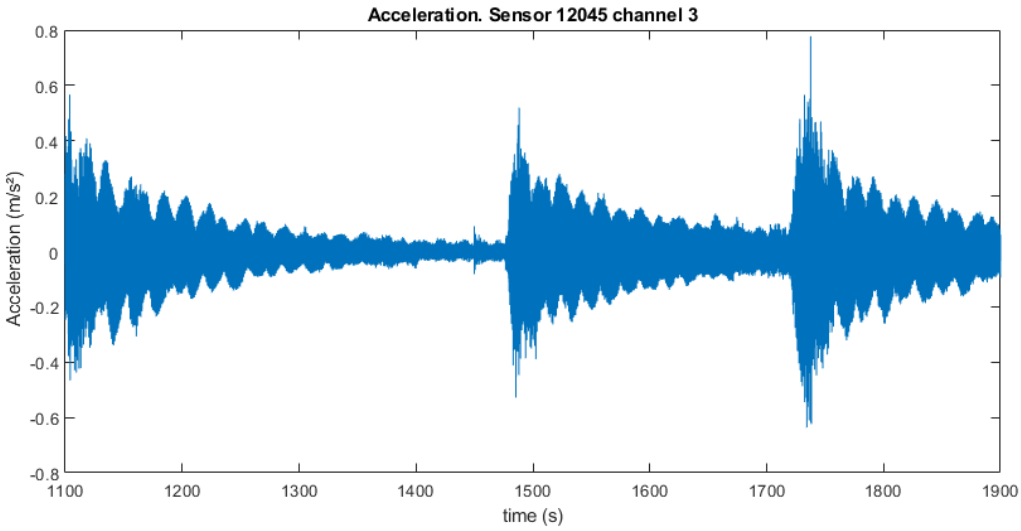

Figure 47 Acceleration records 15/06/2021. Sensor 12045 Heave motion, between $t = 1100\ s$ and $t = 1900\ s$

In the following, the acceleration record will be first translated into displacement time-histories. An exponential function will be fitted to the displacement envelopes, and the damping ratio determined from the fitted function.

The method applied to transform acceleration record into displacement record is via Inverse Fourier Transform, i.e. in the frequency domain. A step-by-step procedure is:

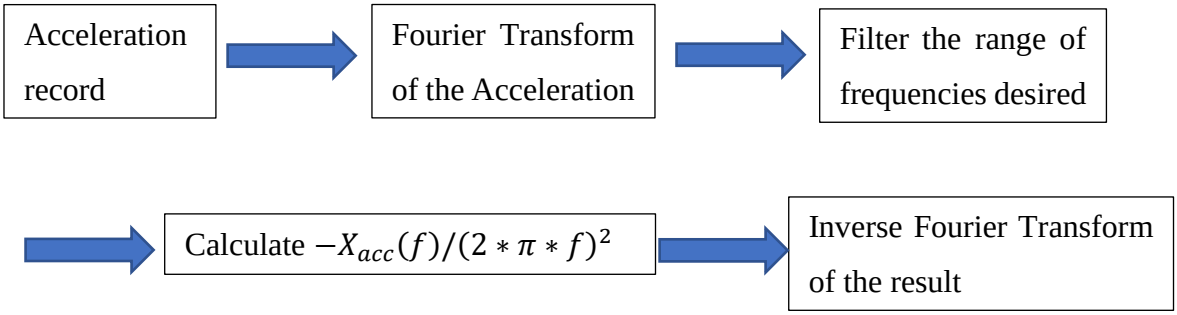

Figure 48 Procedure to transform acceleration record into displacement record

The Fourier Transform is a complex function, which gives a result with real and imaginary parts. The complex number can also be described with a magnitude and a phase. When performing the Inverse Fourier Transform of the filtered complex function, the phase of each frequency component is properly preserved.

One example of the procedure being applied is shown below. It is the data from sensor 12045 (cable bundle C1E, bottom cable on the seaside), heave motion, from time $t = 1170\ s$ until $t = 1440\ s$. The new time array will be from 0 to $270s$, which is the duration of the period analysed.

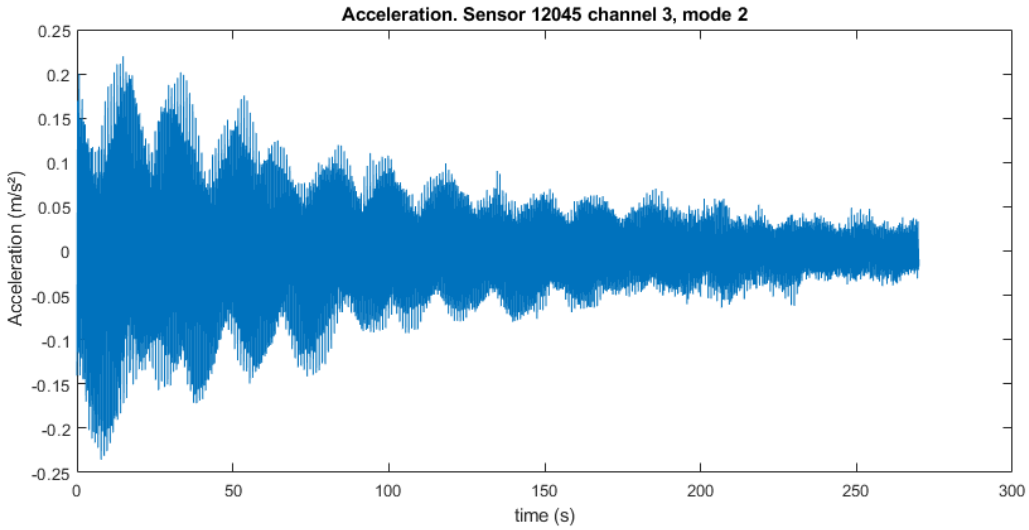

Figure 49 Acceleration records used for free decay 15/06/2021. Sensor 12045 Heave motion

Each frequency studied was separated using a filter with half-width of 0,1 Hz, where the values of the power spectral density were changed to zero outside the filter width. So then for each frequency the range was: $f_n - 0{,}1 < f_{n_{used}} < f_n + 0{,}1\ Hz$. And the power spectral density filtered is,

$$PSD_{used}(f) = PSD\ (f)\ \text{ for }\ f_n - 0{,}1 < f < f_n + 0{,}1\ Hz \qquad 49$$

And

$$PSD_{used}(f) = 0 \text{ for } f < f_n - 0{,}1 \text{ and } f > f_n + 0{,}1\ Hz \qquad 50$$

This method will be used for the first 5 vibration modes.

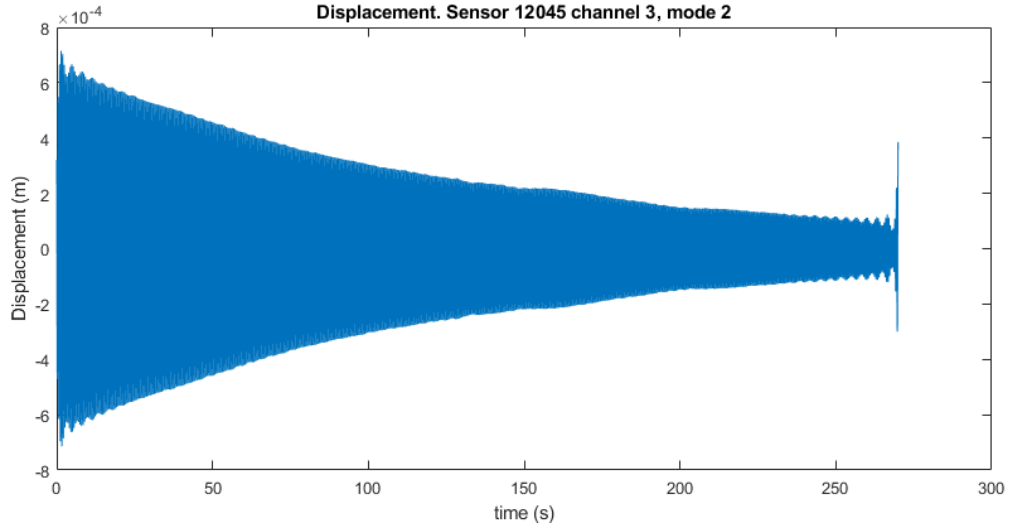

Figure 50 Calculated displacement of the cable during free decay. 15/06/2021. Sensor 12045 Heave motion

The last part of the procedure is to fit an exponential function to the envelope of the displacement. Both positive and negative peaks are used for a higher amount of data points for the fitting. The decay rate also depends on the vibration frequency. Therefore, the damping of

every different vibration mode, studied after the suitable filtering of the free decay response, will be calculated using the vibration frequency of the mode in question to calculate the damping ratio.

The theoretical exponential envelope is calculated as follows:

$$Envelope = E(t) = A_n * \exp(-\zeta_n * \omega_n * t) \quad 51$$

Where A_n is the amplitude of the envelope at time $t = 0$ and n is the vibration mode.

Then, the best fitting (BF) exponential function is found such that:

$$BF_n = B_n \exp(y_n * t) \quad 52$$

where B_n is the amplitude of the fitted exponential function at time $t = 0$ and y_n is the constant value for the best fitted exponential function and n is the vibration mode.

The value for damping ratio ζ_n can be calculated as being:

$$y_n * t = -\zeta_n * \omega_n * t \quad \therefore \quad \zeta_n = -y_n/\omega_n \quad 53$$

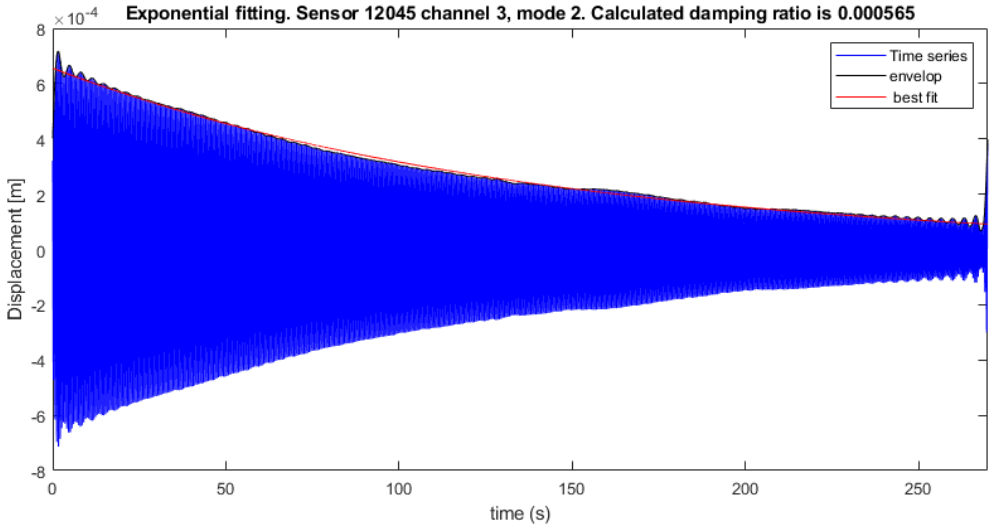

Figure 51 Displacement with envelope and exponential best fit. 15/06/2021. Sensor 12045 Heave motion

In Figure 51, with the filtered free vibration data the damping ratio calculated for the second mode of vibration is $\zeta_2 = 0{,}000565 = 0{,}0565\%$. The value of damping calculated is in the expected range, which can be between 0,01% to 0,2% [1].

The procedure described above was done for the first 5 modes of vibration of the cable, considering the three free decay responses between $t = 1100\ s$ and $t = 1900\ s$.

Some cases show a displacement responses with a beating, this could be due to more than one peak in the power spectral density. Then, when the inverse Fourier transform is calculated, as described in Figure 48, the result can show, for example, a beating phenomenon. Figure 52 shows a case that the beating phenomenon can be seen. Another possible reason is that the cable

is experiencing vibrations that are in fact in with some beating. It can be seen in Figure 49 that the acceleration records, without any signal manipulation, already shows some beating.

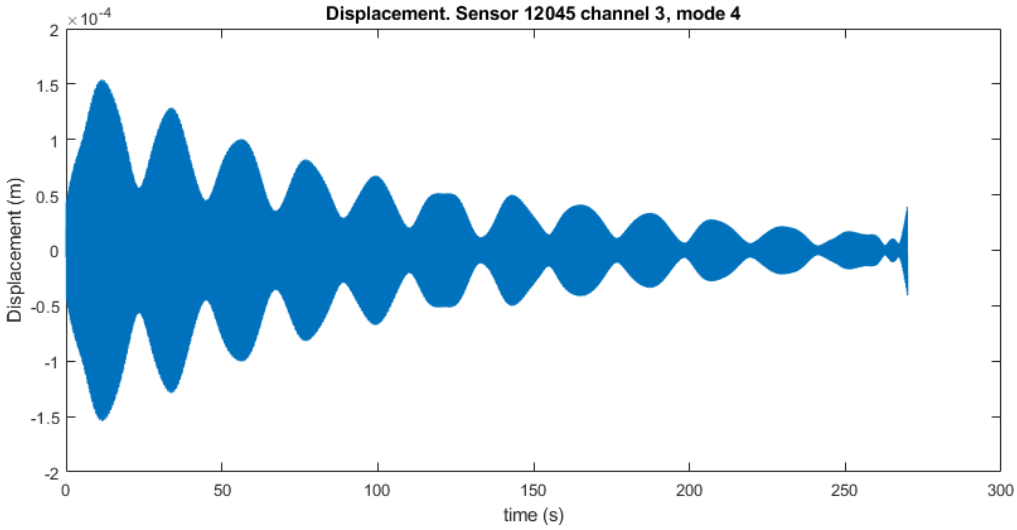

Figure 52 Calculated displacement of the cable during free decay. 15/06/2021. Sensor 12045 Heave motion

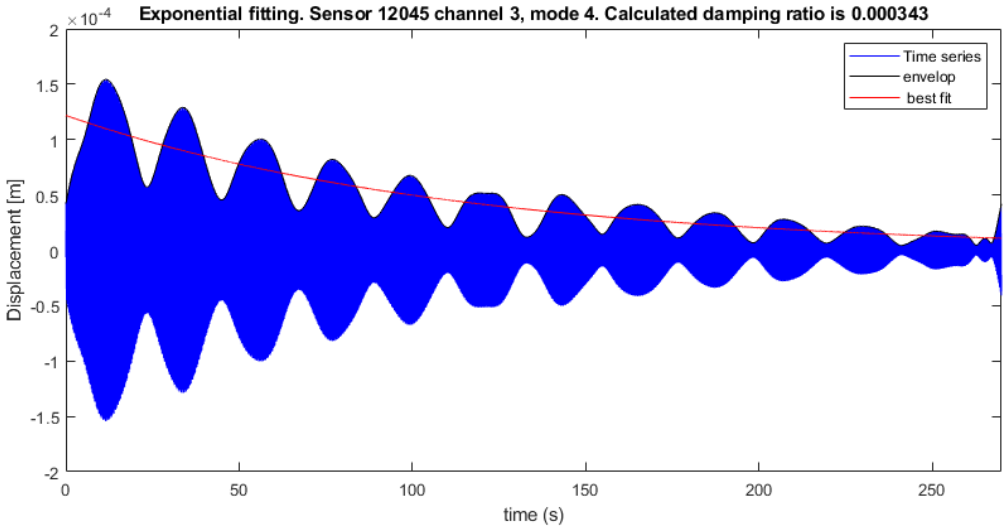

Figure 53 Displacement with envelope and exponential best fit. 15/06/2021. Sensor 12045 Heave motion

Calculating the damping ratio of a free decay response that is experiencing beating can lead to values might not be accurate, but this will still be done because it gives a general understanding of what is the order of magnitude of the damping ratio of the cable.

Other cases show a displacement function that is not compatible to an expected free decay response of a single degree of freedom system. Figure 54 is one example, taken from $t = 1780\ s$ to $t = 1900\ s$.

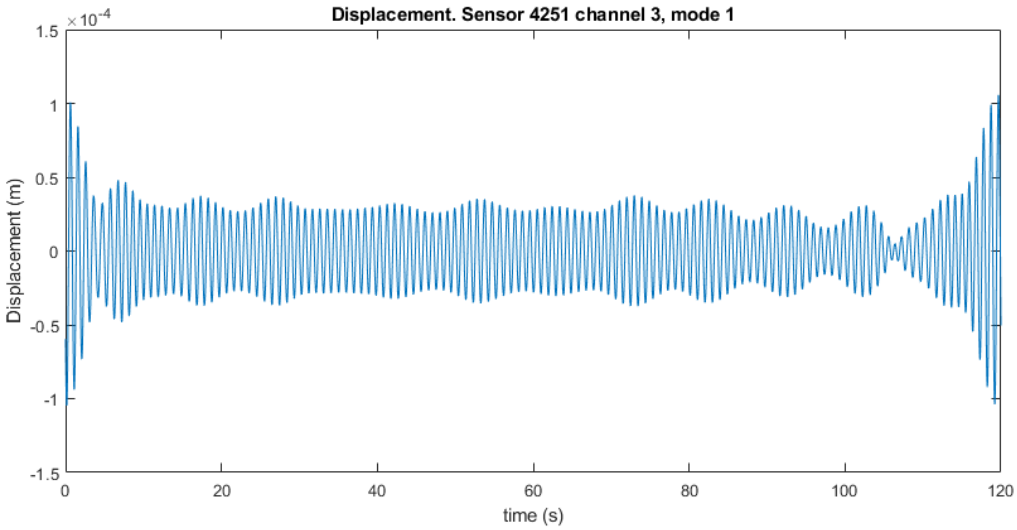

Figure 54 Calculated displacement of the cable during free decay. 15/06/2021. Sensor 4251 Heave motion

Damping ratio should not be estimated for the diagram similar to the one shown in Figure 54, because it has no physical meaning.

Table 7 shows the damping ratio calculated. The values of the three free decay responses are averaged for each sensor. At the last row it is shown the average damping ratio per vibration mode. The values for the sway motion are not considered because they showed inconsistency in the results. The external force was vertical and therefore heave motion is showing better results.

Table 7 Damping ratio estimation. Free Decay Response method

Cable	Sensor	Motion	Damping ratio, vibration mode 1	Damping ratio, vibration mode 2	Damping ratio, vibration mode 3	Damping ratio, vibration mode 4	Damping ratio, vibration mode 5
C1E	12045	Heave	6.91E-04	5.06E-04	4.81E-04	3.47E-04	2.96E-04
C1E	12047	Heave	7.34E-04	4.89E-04	4.84E-04	3.74E-04	2.99E-04
C1E	4251	Heave	7.01E-04	4.97E-04	4.75E-04	3.20E-04	3.24E-04
		Average	7.09E-04	4.98E-04	4.80E-04	3.47E-04	3.06E-04

The values for damping ratio shown in Table 7 are between 0,03% and 0,07% for the average values per vibration mode. The higher vibration modes are showing lower damping ratio coefficient. All the results are within the expected range, which can be between 0,01% to 0,2% [1].

3.3.2 Frequency Domain Decomposition

The second method used is the Frequency Domain Decomposition (FDD). The technique was presented by [28] and it consists of decomposing the power spectral density (PSD) matrix using Singular Value Decomposition. When doing so, the spectral response is decomposed into several single degree of freedom systems, each corresponding to a mode of the original structure. This procedure will be used to analyse the damping ratio of the first 5 modes of vibration of the cable C1E.

The data used will be the values of acceleration record from each sensor in both directions Sway and Heave, simultaneously.

There will be two procedures for the FDD, one uses a spectral peak picking method, where the user defines the area in the power spectral density is the peak.

The other procedure uses an upper and lower boundary around a guess of what the frequency of the peak is, and the program chooses the frequency with its own algorithm. Practically, the result of the frequencies corresponding to the peak picking of the first method will be used as a guess of the target frequency for the second method. The Lower Boundary (LB) is $LB = 0{,}9 * f_{n_{peak\ picking}}$ and Upper Boundary (UB) is $UB = 1{,}1 * f_{n_{peak\ picking}}$.

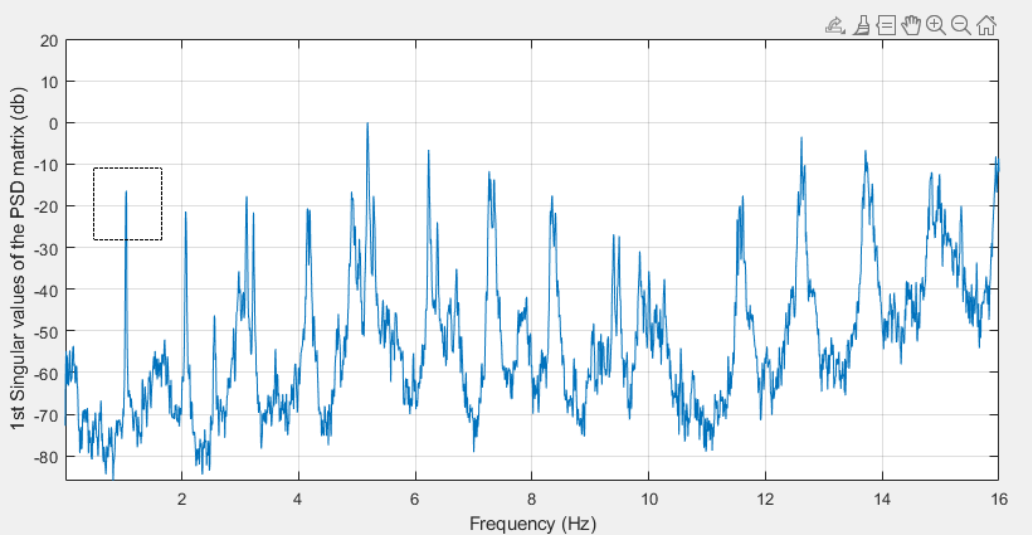

Figure 55 Example of peak picking method around vibration mode 1. Sensor 12045. Data from 14/06/2021 07:05 to 07:45

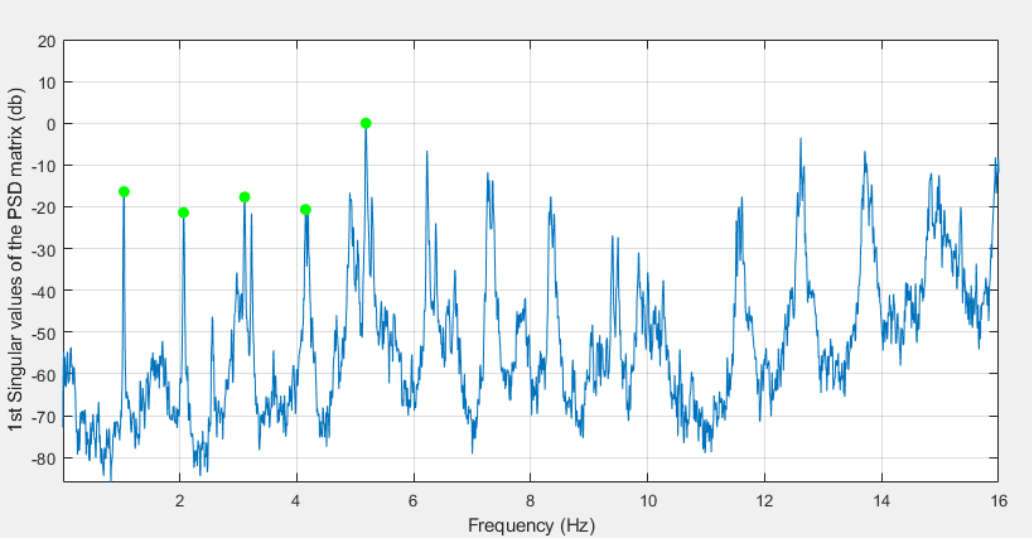

Figure 56 Example of peak picking process. Sensor 12045. Data from 14/06/2021 07:05 to 07:45

It was chosen the data from 14/06/2021 from 07:05 to 07:45 where the cable was excited by ambient vibration only, the average wind velocity was $6{,}5\ m/s$ and no rainfall. The first 5

vibrations modes will be analysed, however in Figure 56 it is possible to see other modes of vibrations.

Four scenarios were chosen using the 40 minutes acceleration record.

- 4 windows of 10 minutes
- 2 windows of 20 minutes
- 1 window of 30 minutes
- 1 window of 40 minutes

The shortest window used was 10 minutes, this means around 570 vibration cycles for the lowest vibration mode. Which are enough cycles for the estimations done.

Table 8 Damping ratio estimation, FDD method Data from 14/06/2021 from 07:05 to 07:45. Heave and sway motion simultaneously.

Damping ratio estimation using FDD from 2021-06-14 / 4 windows of 10 minutes							
Upper/Lower boundary			Damping ratio estimation				
Cable	Sensor	Channel	Damping ratio, vibration mode 1	Damping ratio, vibration mode 2	Damping ratio, vibration mode 3	Damping ratio, vibration mode 4	Damping ratio, vibration mode 5
C1E	12045	2/3	3.50E-03	1.80E-03	1.60E-03	2.30E-03	1.40E-03
C1E	12047	2/3	2.60E-03	1.50E-03	2.00E-03	2.00E-03	1.30E-03
C1E	4251	2/3	3.30E-03	1.90E-03	2.20E-03	1.30E-03	1.40E-03
Average			3.13E-03	1.73E-03	1.93E-03	1.87E-03	1.37E-03
Peak picking			Damping ratio estimation				
Cable	Sensor	Channel	Damping ratio, vibration mode 1	Damping ratio, vibration mode 2	Damping ratio, vibration mode 3	Damping ratio, vibration mode 4	Damping ratio, vibration mode 5
C1E	12045	2/3	4.20E-03	2.40E-03	2.40E-03	3.20E-03	1.40E-03
C1E	12047	2/3	4.40E-03	2.40E-03	2.40E-03	2.60E-03	1.50E-03
C1E	4251	2/3	4.00E-03	2.30E-03	2.60E-03	2.00E-03	1.30E-03
Average			4.20E-03	2.37E-03	2.47E-03	2.60E-03	1.40E-03

FDD using the peak picking method can also estimate the eigenfrequency by identifying the frequency associated with the peak in energy from the power spectra density. From Figure 55 it can be seen how this is done, the user chooses an area around the peak, and the procedure finds the frequency corresponding to the peak.

When using the upper/lower boundary method, the procedure also finds the peak within the range of 90% to 110% of the guessed value for the eigenfrequency. The two methods give the same estimation as it can be seen in Table 9.

Table 9 Eigenfrequency estimation, FDD method. Data from 14/06/2021 from 07:05 to 07:45 Heave and sway motion simultaneously.

Frequency estimation using FDD from 2021-06-14 / 4 windows of 10 minutes							
Upper/Lower boundary			Eigen frequency estimation				
Cable	Sensor	Channel	fn1 [Hz]	fn2 [Hz]	fn3 [Hz]	fn3 [Hz]	fn4 [Hz]
C1E	12045	2/3	1.0426	2.0638	3.1045	4.1458	5.1793
C1E	12047	2/3	1.0426	2.0638	3.1045	4.1796	5.1800
C1E	4251	2/3	1.0426	2.0638	3.1045	4.1425	5.1767
Average			1.0426	2.0638	3.1045	4.1560	5.1787
Peak picking			Eigen frequency estimation				
Cable	Sensor	Channel	fn1 [Hz]	fn2 [Hz]	fn3 [Hz]	fn3 [Hz]	fn4 [Hz]
C1E	12045	2/3	1.0426	2.0638	3.1045	4.1458	5.1793
C1E	12047	2/3	1.0426	2.0638	3.1045	4.1796	5.1800
C1E	4251	2/3	1.0426	2.0638	3.1045	4.1425	5.1767
Average			1.0426	2.0638	3.1045	4.1560	5.1787

The same procedure was carried out for the other 3 scenarios. Table 7 shows the results of the 4 scenarios, where the value for each scenario is already average for the 3 sensors.

Table 10 Damping ratio estimation, FDD method. Data from 14/06/2021 from 07:05 to 07:45. Heave and sway motion simultaneously.

Upper/Lower boundary	Damping ratio, vibration mode 1	Damping ratio, vibration mode 2	Damping ratio, vibration mode 3	Damping ratio, vibration mode 4	Damping ratio, vibration mode 5
4 windows of 10 minutes	3.13E-03	1.73E-03	1.93E-03	1.87E-03	1.37E-03
2 windows of 20 minutes	2.30E-03	1.40E-03	2.13E-03	1.87E-03	1.43E-03
1 window of 30 minutes	2.30E-03	1.40E-03	1.83E-03	1.87E-03	1.27E-03
1 window of 40 minutes	2.20E-03	1.60E-03	1.93E-03	1.90E-03	1.27E-03
Average	2.48E-03	1.53E-03	1.96E-03	1.88E-03	1.33E-03
Peak picking	Damping ratio, vibration mode 1	Damping ratio, vibration mode 2	Damping ratio, vibration mode 3	Damping ratio, vibration mode 4	Damping ratio, vibration mode 5
4 windows of 10 minutes	4.20E-03	2.37E-03	2.47E-03	2.60E-03	1.40E-03
2 windows of 20 minutes	2.27E-03	1.47E-03	2.23E-03	1.80E-03	1.43E-03
1 window of 30 minutes	2.23E-03	1.40E-03	1.73E-03	1.97E-03	1.27E-03
1 window of 40 minutes	1.87E-03	1.47E-03	2.13E-03	1.83E-03	1.20E-03
Average	2.64E-03	1.68E-03	2.14E-03	2.05E-03	1.33E-03

The values from Upper/Lower boundary method similar to the Peak Picking method for most cases. The results are overall high for both methods, some values are above the expected range of 0,01% to 0,2% [1]. The stay cables do not have any added damping devices that can justify the results to be in the high end of the proposed range. The values are higher than what was estimated in 3.3.1, which are between 0,03% and 0,07%.

3.3.3 Random Decrement Technique

The third method will be using the recorded acceleration from ambient load, it was chosen data from 14/06/2021 from 07:05 to 07:45, which is the same records used in 3.3.2, this will make it easier to compare the two methods. Again, the mean wind velocity was $6{,}5\,m/s$ and no rainfall. Only the heave motion will be analysed.

A Random Decrement Technique uses the assumption that the displacement response of the structure is composed of two parts, a random part with average equal to zero and a deterministic

part. The data is divided into many windows that will be averaged in order to remove the random part [29]. Then the Free Decay Response is calculated using the following equation.

$$FDR(\tau) = \frac{1}{N}\sum_{i=1}^{N} s(t_i + \tau) \qquad 54$$

where FDR is the Free Decay response, s is the acceleration response, t_i is the time at the beginning of each window, and N is the number of windows.

The number of windows is set to $N = 60$ and $40\ minutes$ of acceleration data, which leads to a free decay response length of $40\ s$. The response contains at least 40 vibration cycles for the lowest mode, which is enough to evaluate the exponential function that best fit the free decay.

All the following diagrams are from the same 40-minute period, so all the results will have the same loading scenario of wind speeds and traffic, only variability between them is the sensor and vibration mode, which is explicitly mentioned in the title along the calculated damping ratio from the free decay envelope. Each sensor is in a different cable inside the cable bundle C1E as shown in Table 2.

The first part of the procedure is to translate the acceleration records into displacement response of the cable. Figure 48 explain how this is carried out. Then, the displacement response is divided into $N = 60$ parts, and the function in Equation 54 is used. The free decay is then normalized so that the maximum displacement is 1.

The damping ratio will be calculated similarly to 3.3.1, where a envelope is calculated for the free decay response mentioned and a exponential function is estimated to be the best for the envelope, then, using the natural frequency of the vibration being analysed, the damping ratio can be calculated.

The RDT seems to be sensitive to more than one peak in the PSD, therefore the filter half-width had to be reduced from $0{,}3\ Hz$ to $0{,}1\ Hz$. Figure 57 shows an example of the filter half-width of $0{,}3\ Hz$ and Figure 58 shows the same scenario but a filter half-width of $0{,}1\ Hz$.

Figure 59 shows the two peaks close to each other near vibration mode 3 when the filter half-width is $0{,}3\ Hz$.

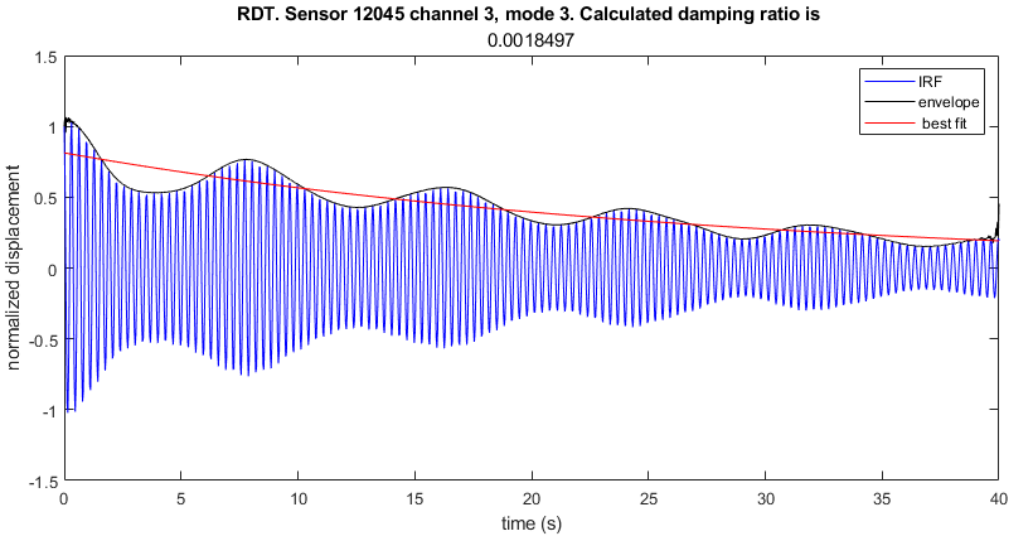

Figure 57 Displacement response, envelope and exponential best fit. 15/06/2021. Sensor 12045 Heave motion. Filter half-width = 0,3 Hz

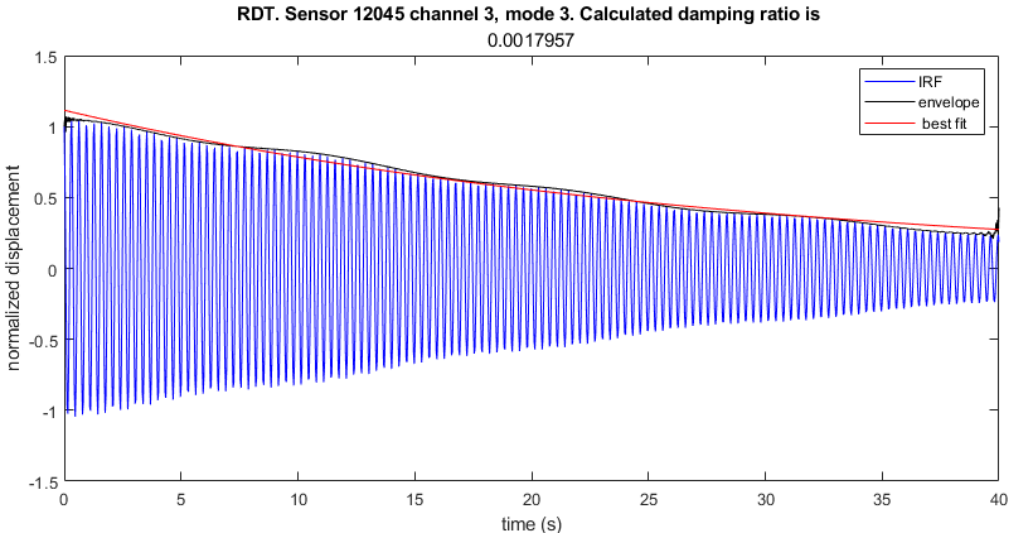

Figure 58 Displacement response, envelope and exponential best fit. 15/06/2021. Sensor 12045 Heave motion. Filter half-width = 0,1 Hz

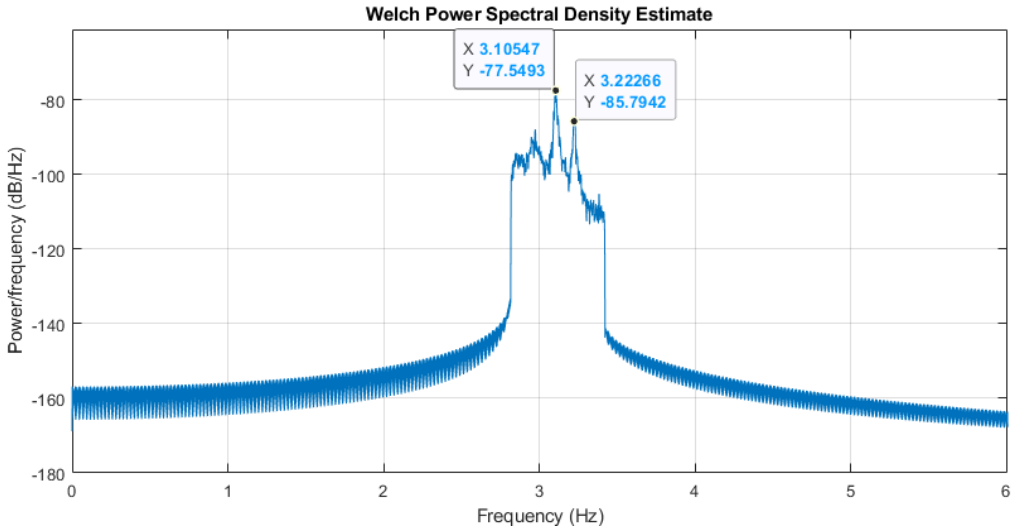

Figure 59 Acceleration PSD with filter half-width = 0,3 Hz around vibration mode 3. 15/06/2021 Sensor 12045 Heave motion

Similarly, Figure 60 shows the two peaks near vibration mode 4, which are too close to each other and would require a filter as narrow as a half-width of $0{,}01\ Hz$ to split them apart. One example of the filter half-width of $0{,}1\ Hz$ for vibration mode 4 is shown in Figure 61. The magnitude of each peak is also closer than for mode 3. This happens for sensors 12045 and 12047, which are the top cable on the roadside and the bottom cable on the seaside. The displacement response of the sensor 4251, the bottom cable on the roadside, is presented in Figure 62 and does not show the beating phenomena because there is just one peak in the filtered window.

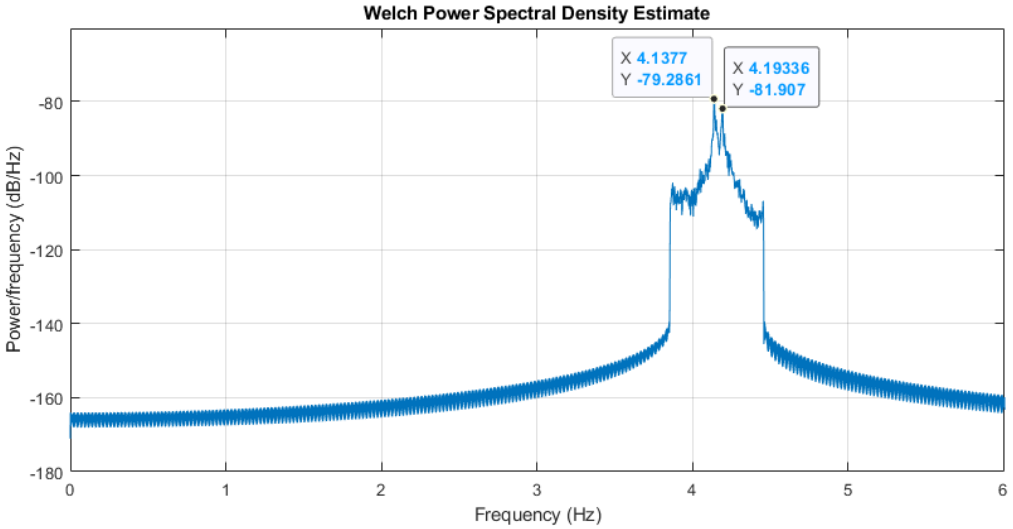

Figure 60 Acceleration PSD with filter half-width = 0,3 Hz around vibration mode 4. 15/06/2021 Sensor 12045 Heave motion

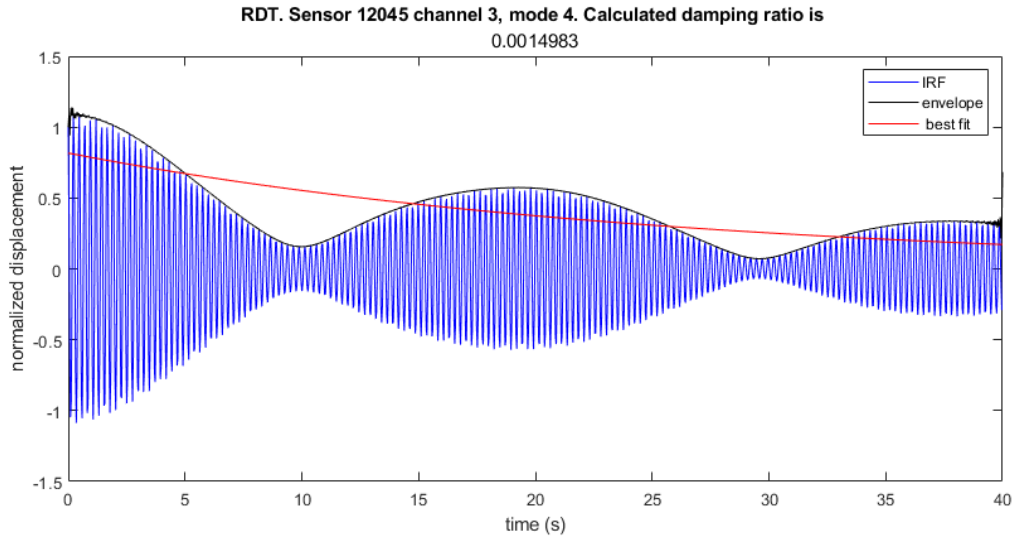

Figure 61 Displacement response, envelope and exponential best fit, mode 4. 15/06/2021. Sensor 12045 Heave motion. Filter half-width = 0,1 Hz

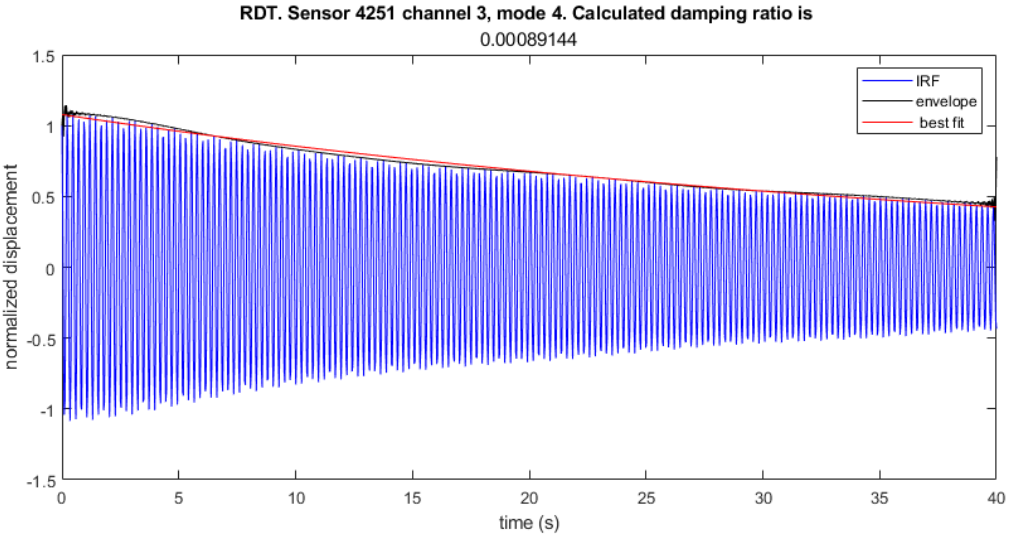

Figure 62 Displacement response, envelope and exponential best fit, mode 4. 15/06/2021. Sensor 4251 Heave motion. Filter half-width = 0,1 Hz

Table 11 Damping ratio estimation using RDT

Cable	Sensor	Channel	Damping ratio, vibration mode 1	Damping ratio, vibration mode 2	Damping ratio, vibration mode 3	Damping ratio, vibration mode 4	Damping ratio, vibration mode 5
C1E	12045	Ch3	7.12E-04	9.90E-04	1.80E-03	1.50E-03	1.01E-03
C1E	12047	Ch3	7.18E-04	9.76E-04	1.82E-03	1.62E-03	1.05E-03
C1E	4251	Ch3	7.45E-04	9.90E-04	1.97E-03	8.91E-04	1.07E-03
Average			7.25E-04	9.85E-04	1.86E-03	8.91E-04	1.04E-03

The values for the vibration mode 4 using the records from sensors 12045 and 12047 are highlighted because they do not correspond to a realistic damping estimation, those values are not considered in the average.

The damping ratio for modes 1, 2, 4 and 5 show similar order of magnitude when compared to the free decay estimated in 3.3.1. Vibration mode 3 shows a high damping ratio, when compared to the expected range of 0,01% to 0,2% [1].

3.3.4 Damping ratio as a function of displacement

Damping ratio was treated, so far, as a parameter independent of the displacement magnitude, and the exponential envelopes fitted to the data, for instance in Figure 51, suggest that the damping level is rather stable throughout the decay. In the following, this is additionally examined in more details, by estimating the damping ratios for large and small vibration amplitudes.

It will be used the free decay technique shown in 3.3.1. There are three free decay responses that are suitable to this analysis, all between $t = 1150\ s$ and $t = 1400\ s$ shown in Figure 44 to Figure 46. Each time series will be divided into $50\ s$ long window that will be fitted by a logarithmic envelope.

Since the absolute magnitude of displacement is important, the acceleration records were manipulated using the calibration function provided by the manufacturer.

It was shown in 3.3.1 that some vibration modes are experiencing beating phenomenon, probably because of two peaks in the PSD being within the filter range, or because the cable was experiencing beating during the recorded data. The windows of analyses for the free decay response is $50\ s$, therefore, the result is more susceptible to the beating, when compared to the windows of at least $100\ s$ and up to $300\ s$ that were used in 3.3.1. Therefore, only the cases that do not show beating phenomenon will be used.

Using the Equation 32, it is possible to translate the amplitudes at the position of the accelerometer, which is placed $4\ m$ above the bridge deck, to the maximum displacement of the cable for the given mode of vibration.

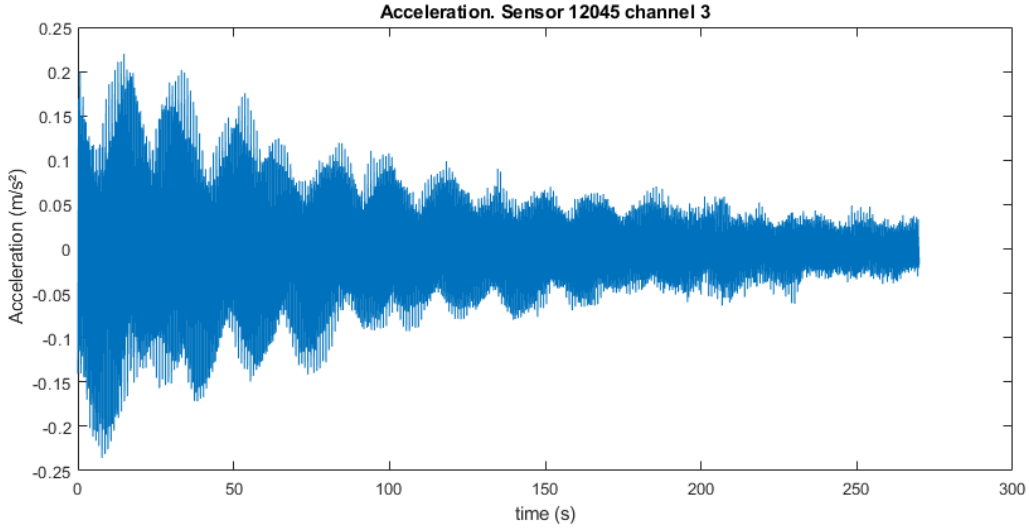

Figure 63 Free decay response for damping-amplitude relation. Sensor 12045. Heave motion

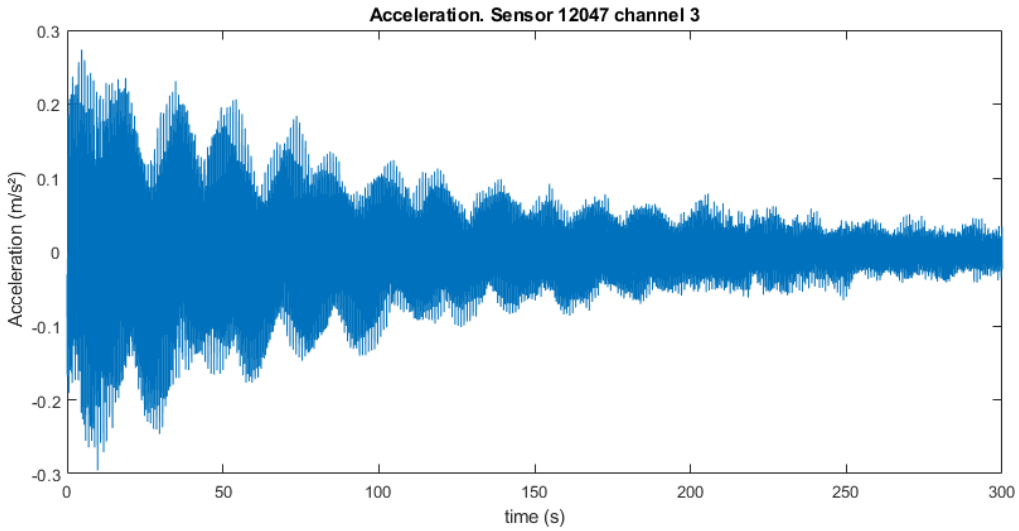

Figure 64 Free decay response for damping-amplitude relation. Sensor 12047. Heave motion

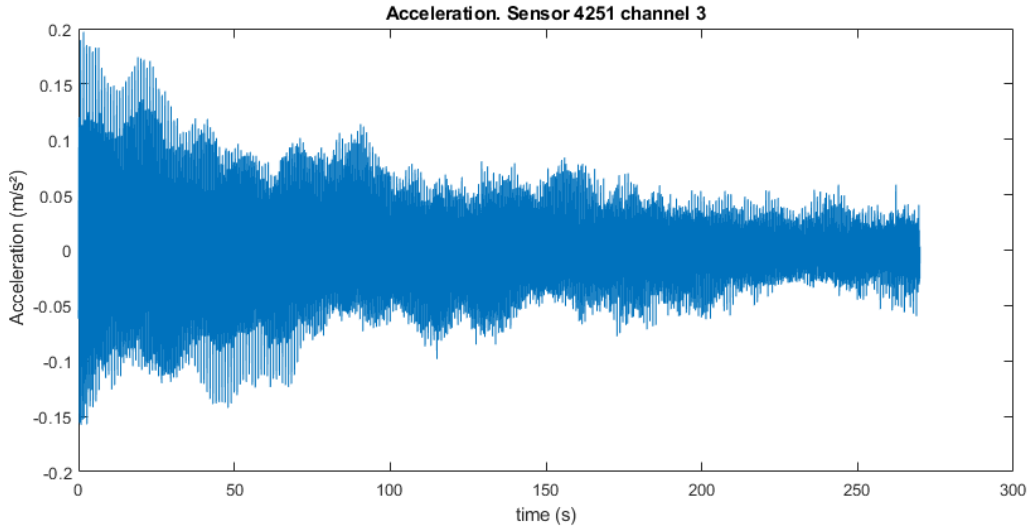

Figure 65 Free decay response for damping-amplitude relation. Sensor 4251. Heave motion

The results were group per vibration mode, and each diagram shows the values of displacement amplitude and damping ratio of the three cables.

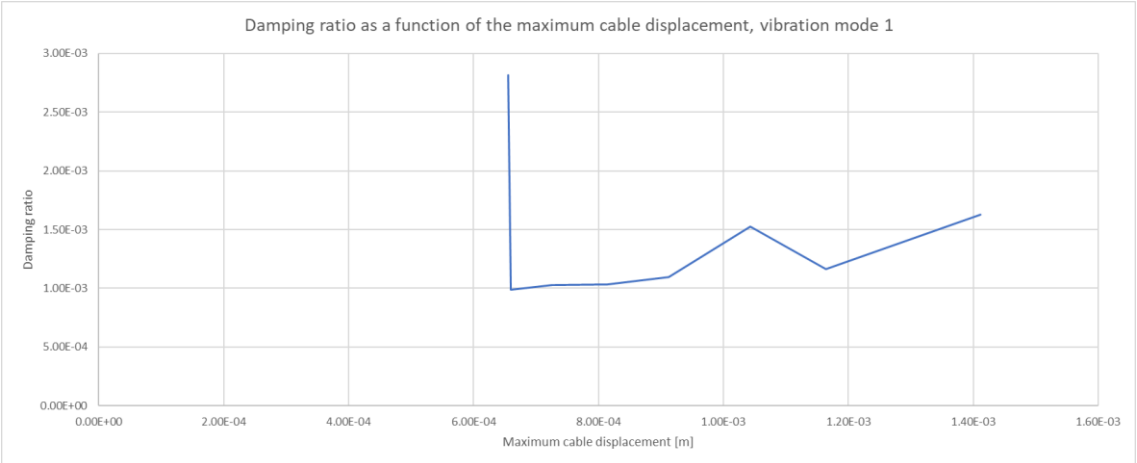

Figure 66 Damping ratio as a function of maximum vibration amplitude. Vibration mode 1. Heave motion

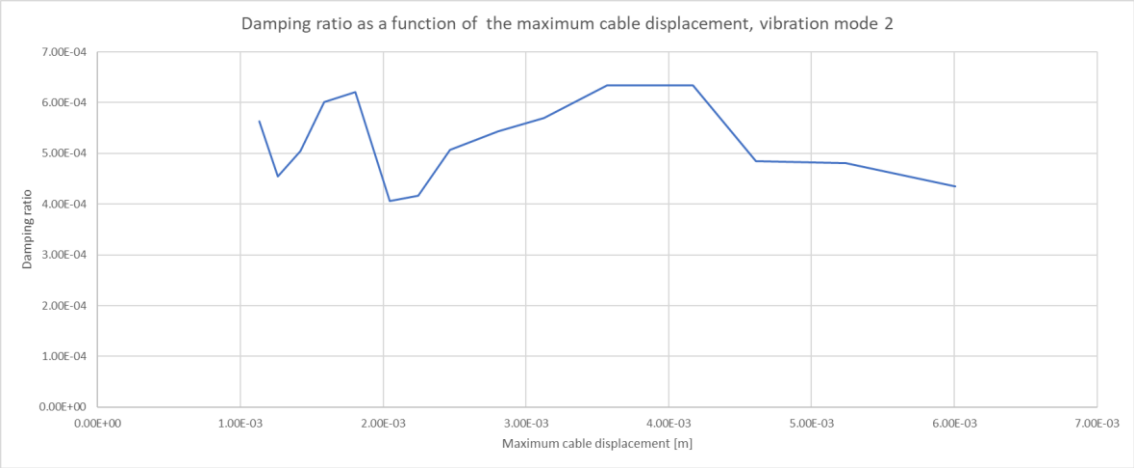

Figure 67 Damping ratio as a function of maximum vibration amplitude. Vibration mode 2. Heave motion

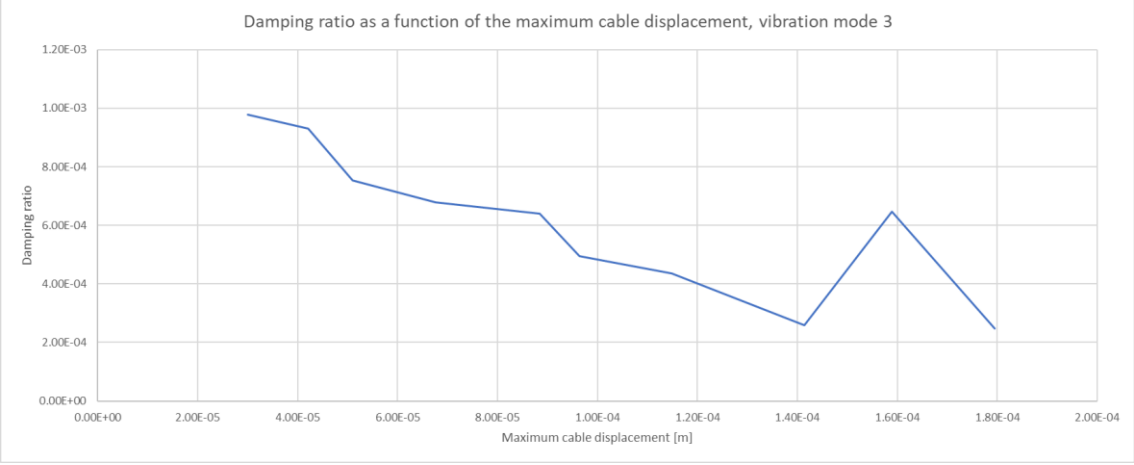

Figure 68 Damping ratio as a function of maximum vibration amplitude. Vibration mode 3. Heave motion

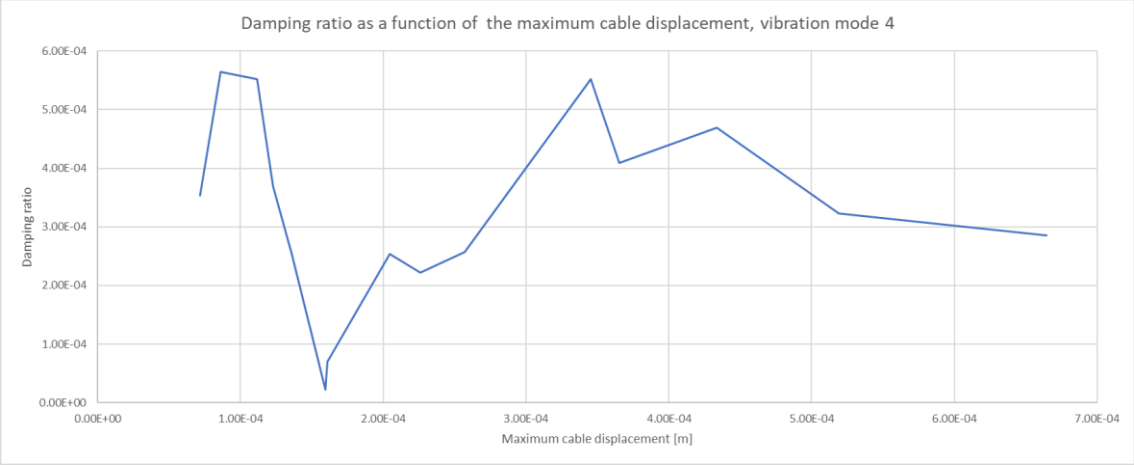

Figure 69 Damping ratio as a function of maximum vibration amplitude. Vibration mode 4. Heave motion

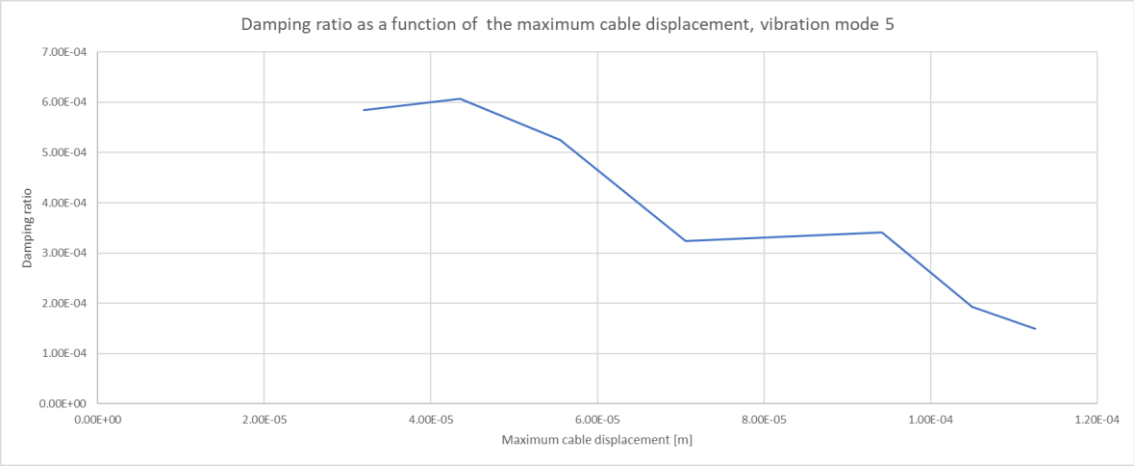

Figure 70 Damping ratio as a function of maximum vibration amplitude. Vibration mode 5. Heave motion

Vibration modes 3 and 5 show a decrease in damping ratio when the maximum vibration amplitude increases. Vibration modes 1, 2 and 4 do not show a relationship between vibration amplitude and damping ratio.

It is important to remember that the cable showed displacement much larger that what is shown in Figure 66 to Figure 70, because what is estimated here is the displacement amplitude that the cable would experience if the vibration mode being analysed was isolated from the other accelerations in the acceleration power spectral density.

3.4 Stockbridge damper analysis

The viability of a Stockbridge damper as a solution to damp the vibration will be studied.

Stockbridge dampers are worldwide used in transmission lines but there are some cases where it has been used in suspension cable in cable suspension bridge, backstay of large structures and stays of cable-stayed bridges.

Figure 71 Back stay of London Eye featuring a Stockbridge damper [15]

It has been observed that the largest vibrations of the cable C1E occur in the 3rd mode of vibration [2], therefore the Stockbridge damper will be tuned to that vibration frequency.

A two degree of freedom (2DOF) system will be analysed where the Stockbridge damper and the cable are coupled. The variables k_3 (modal stiffness of the cable), m_3 (modal mass of the cable) and x_3 (modal displacement of the cable) are all regarding the 3rd mode of vibration of the cable, whereas k_{SB} (stiffness of the Stockbridge damper), m_{SB} (mass of the Stockbridge damper), c_{SB} (damping coefficient of the Stockbridge damper), x_{SB} (displacement of the Stockbridge damper) are regarding the Stockbridge device. When the case of a forced vibration is analysed, the force $F(t)$ will be then applied to the cable.

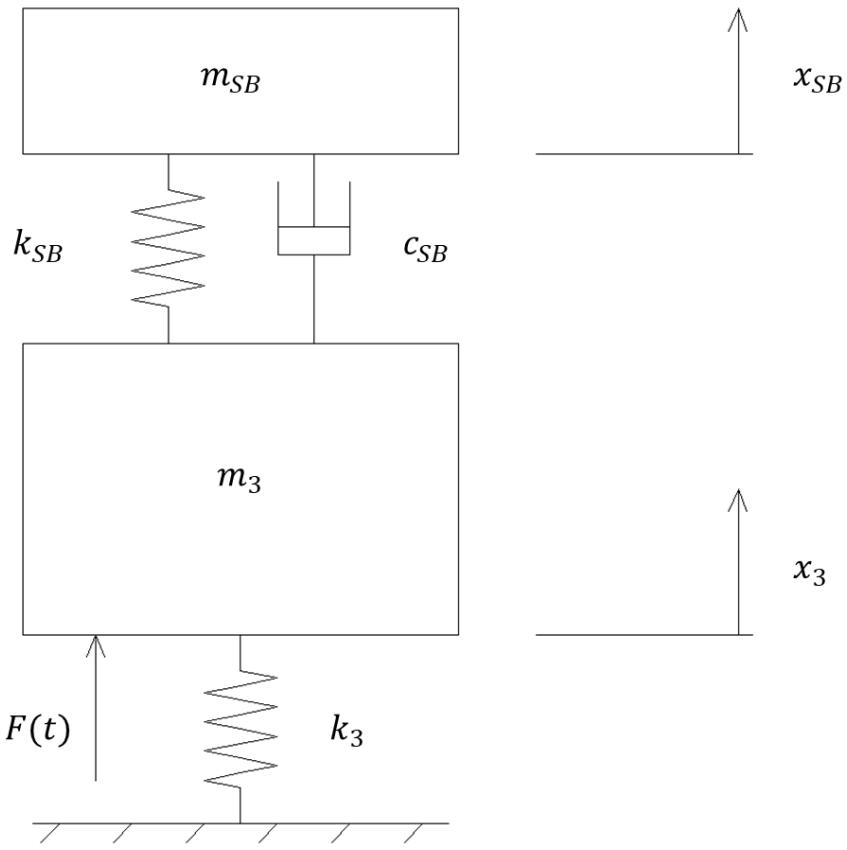

Figure 72 Two degree of freedom system

Figure 72 shows a general arrangement of the 2DOF system. There will either be an initial displacement of the cable, and then the system is let to vibrate freely with no external force $F(t)$, or there will be an external force $F(t)$ and no initial displacement. Both these cases will be shown in 3.4.3. The magnitude of the damping coefficient c_{SB} will also be changed in order to analyse the response of the system for different damping coefficients of the Stockbridge damper. As a conservative approach, and for simplicity, the damping coefficient of the cable itself (discussed in 3.3) was taken as zero.

The system of differential equations to be solved is:

$$\begin{cases} m_3 * \ddot{x}_3 = -k_3 * x_3 - k_{SB} * (x_3 - x_{SB}) - c_{SB} * (\dot{x}_3 - \dot{x}_{SB}) + F(t) \\ m_{SB} * \ddot{x}_{SB} = k_{SB} * (x_3 - x_{SB}) + c_{SB} * (\dot{x}_3 - \dot{x}_{SB}) \end{cases} \quad 55$$

The MATLAB function ode45 [25] will be used to solve the system above using different initial conditions and parameters, depending on the case being studied. The ode45 function solves non-stiff differential equations, using the medium order method [30].

3.4.1 Cable modal parameters

The modal mass of the cable can be calculated as follows.

$$M_n = \int_0^L m_l * \left(W_n(x)\right)^2 \, dx = \int_0^L m_l \, * \left(sin\left(n * \pi * \frac{x}{L}\right)\right)^2 \, dx \qquad 56$$

For the 3rd mode of vibration, the value of $n = 3$. The mass per unit length of the cable is previously calculated as $m_l = 33{,}5\ kg/m$, length of the cable is $L = 98{,}263\ m$.

$$M_3 = \int_0^L m_l * W_3(x)\, dx = \int_0^L m_l \, * sin\left(3 * \pi * \frac{x}{L}\right) \, dx = 1645{,}9\ kg \qquad 57$$

The easier way of calculating the modal stiffness will be using the known relationship between stiffness, mass and eigenfrequency. The value for $f_3 = 3{,}14\ Hz = 19{,}73\ rad/s$.

$$K_n = M_n * \omega_n^2 \qquad 58$$

Again, for $n = 3$ the equation will be:

$$K_3 = M_3 * (\omega_3)^2 = 1645{,}9 * 19{,}73^2 = 640640\ N/m \ = 640{,}64\ kN/m \qquad 59$$

3.4.2 Stockbridge damper parameters

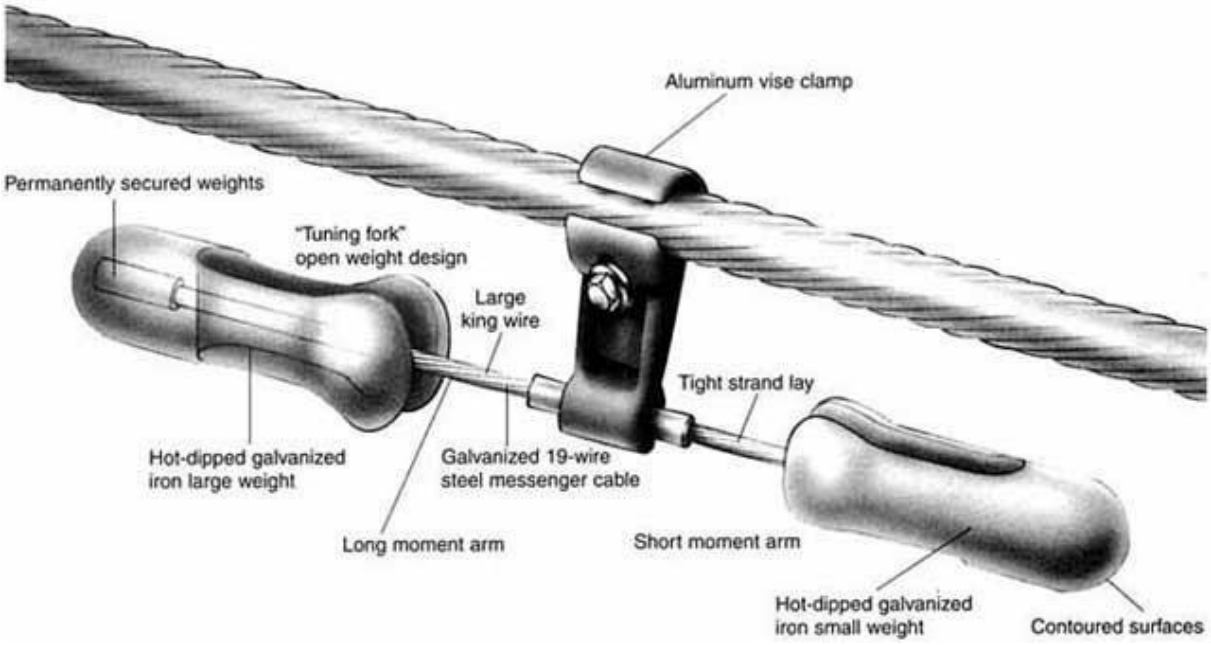

Figure 73 Components of a Stockbridge damper [31]

For simplicity, the Stockbridge damper will be treated as a single degree of freedom device, however, the damper can be designed in with masses and wires that will produce 4 meaningful vibration modes that are in the same range of the main structure important modes to be damped. The centre of gravity of the mass is usually offset to the point of which the wire is connected to the mass, which leads to a vibration mode which is the mass rotating without significant vertical movement.

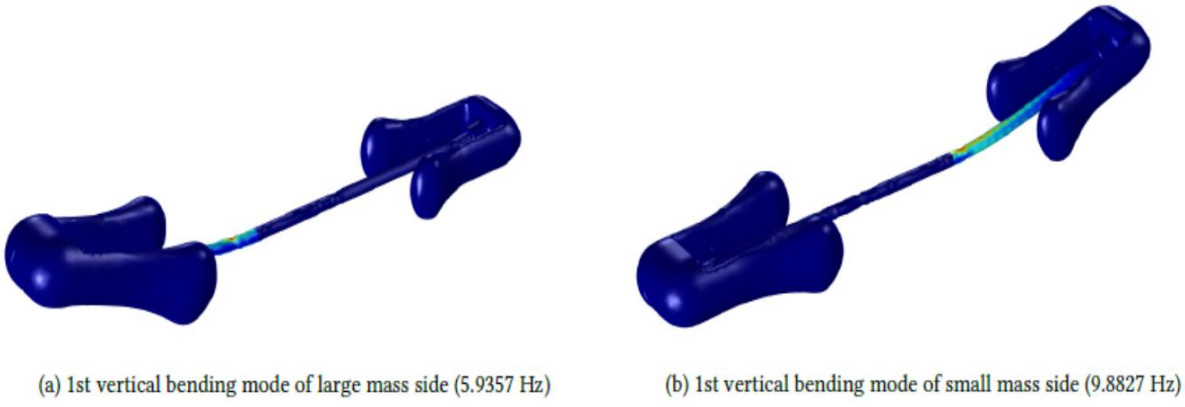

(a) 1st vertical bending mode of large mass side (5.9357 Hz)

(b) 1st vertical bending mode of small mass side (9.8827 Hz)

Figure 74 Example of two vibration modes of a Stockbridge damper [31]

The parameters of the Stockbridge damper are highly manufacturer specific. Therefore, the values for mass, stiffness and damping ratio are subjective to the device itself. After searching for the range of produced option it was chosen a mass of $m_{SB} = 3{,}65\ kg$ as being feasible. Other values could have been chosen and would slightly change the final result.

The stiffness k_{SB} is chosen to achieve the desired eigenfrequency of the device, taking into account the value for mass already chosen. The stiffness of the messenger cable can vary greatly from a stiff short cable with values around $k = 10.000\ N/m$ to less stiff long cables with values around $k = 1.000\ N/m$ or lower.

The aim is to have the Stockbridge damper with the same natural frequency as the cable, therefore the following equation was solved.

$$\omega_{SB} = \omega_3 = 19{,}73\frac{rad}{s} = \sqrt{\frac{k_{SB}}{m_{SB}}} \quad \therefore \quad k_{SB} = 1.420\frac{N}{m} \qquad 60$$

The Stockbridge damper dissipates energy by the bending of the messenger cable. The value of the equivalent viscous damping ratio of the mass moving at the end of the messenger cable is an important parameter for the calculation of the two degree of freedom system. Since this dissipation is the only damping in the model.

A study of damping ratio as a function of displacement was conducted by [32] and shows that, for the Stockbridge damper used in the study, the maximum value of damping ratio was $\zeta = 0{,}13$ and the minimum value found was $\zeta = 0{,}05$. The results by [32] were achieved by testing the Stockbridge damper with a cam machine and recording the acceleration of the mass. The damping ratio was estimated and analysed in relation to the cam machine base displacement. Therefore, once again on the conservative side, the maximum value to be used will be $\zeta = 0{,}05$. In some cases, damping ratio will be chosen as $\zeta = 0{,}01$ for comparison of the results.

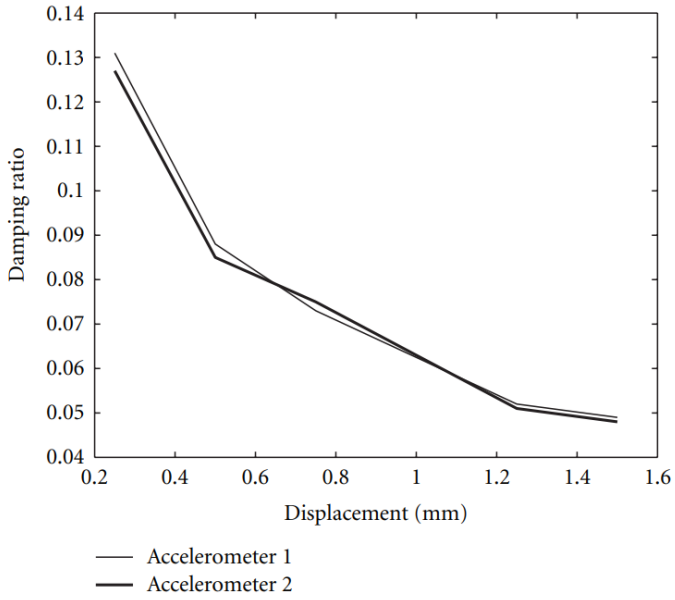

Figure 75 Damping ratio versus base displacement [32]

3.4.3 Results of the 2DOF system

The first scenario will be as follows:

- No damping c_{SB}
- Initial displacement $x_{3_0} = 0{,}01\ m$
- No exciting force

The results will be calculated for the first 20 seconds of free vibrations. It will be analysed the value of the maximum displacement of the Stockbridge damper in relation to the initial displacement value of the cable.

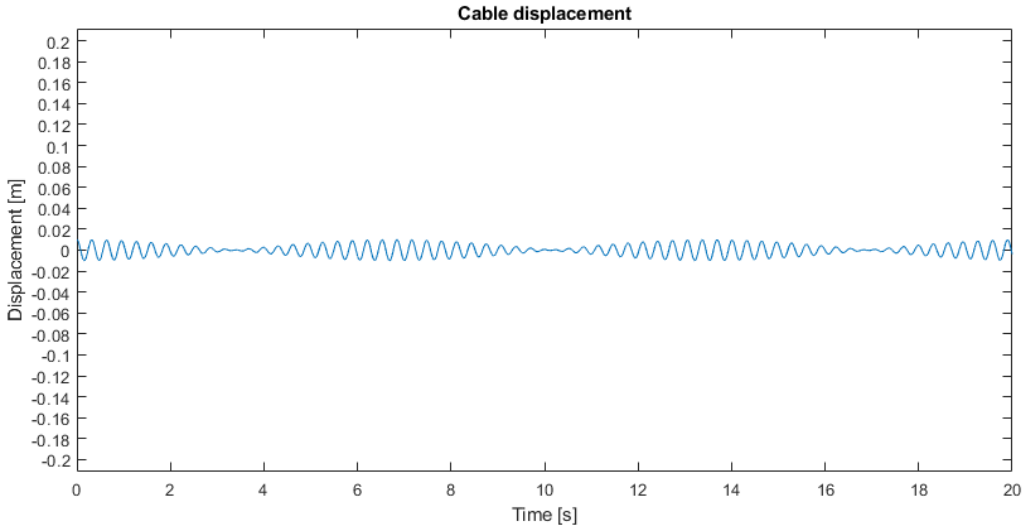

Figure 76 Cable displacement. Scenario 1

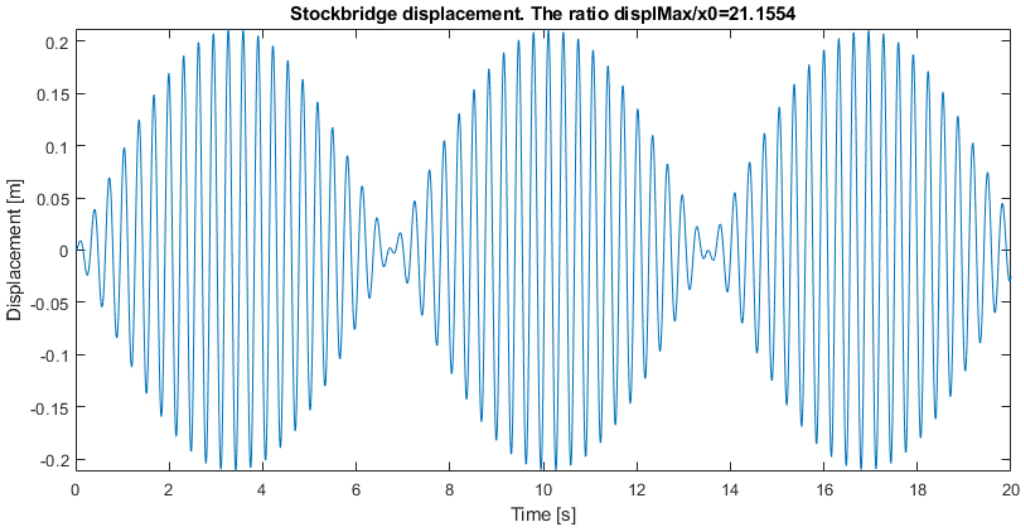

Figure 77 Stockbridge displacement. Scenario 1

It is seen that the cable and the Stockbridge device will exchange energy, when the cable has large displacements (around the value of initial displacement x_{3_0}) the damper has small displacement, and vice versa. This behaviour will extend indefinitely because there is no damping. The maximum amplitude of displacement of the Stockbridge damper is 21,2 times larger than the initial displacement given to the cable. This maximum amplitude will decrease when some damping is introduced.

The second scenario will be as follows:

- Damping ratio of $\zeta_{SB} = 0{,}01 \therefore c_{SB} = \zeta * 2 * \sqrt{k_{SB} * m_{SB}}$
- Initial displacement $x_{3_0} = 0{,}01\ m$
- No exciting force

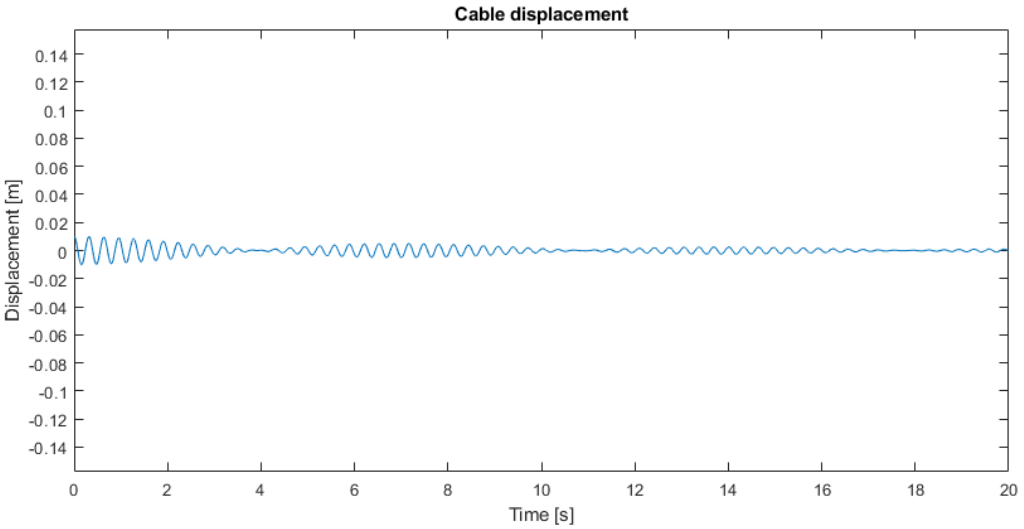

Figure 78 Cable displacement. Scenario 2

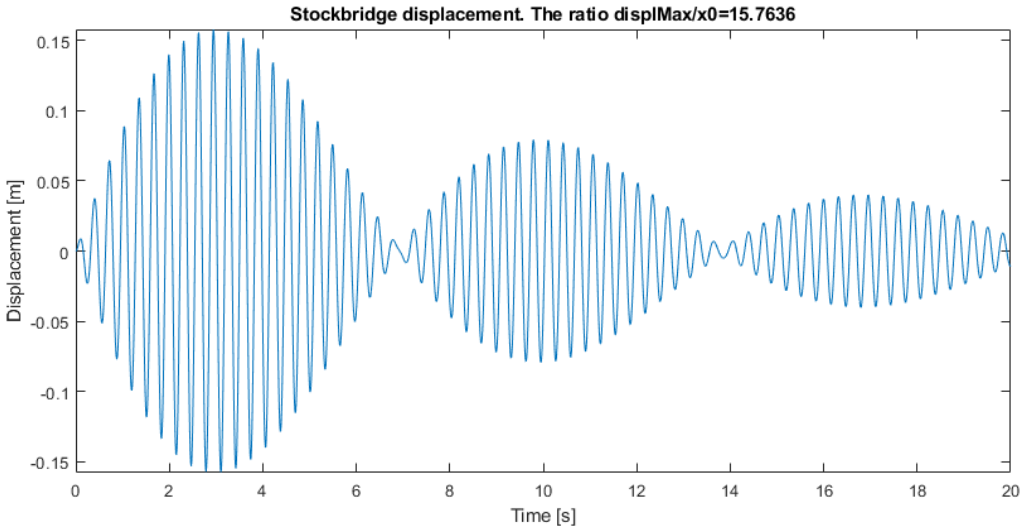

Figure 79 Stockbridge displacement. Scenario 2

For damping ratio of $\zeta_{SB} = 0{,}01$, which is lower than what has been measured by [32], the cable displacement response shows a promising decrease.

It is possible to fit an exponential decay function to the envelope of overall cable displacement response, it will not be precise since the cable is experiencing the beating phenomena, but it is still an important parameter to calculate, since it shows what the equivalent damping ratio the cable itself would experience.

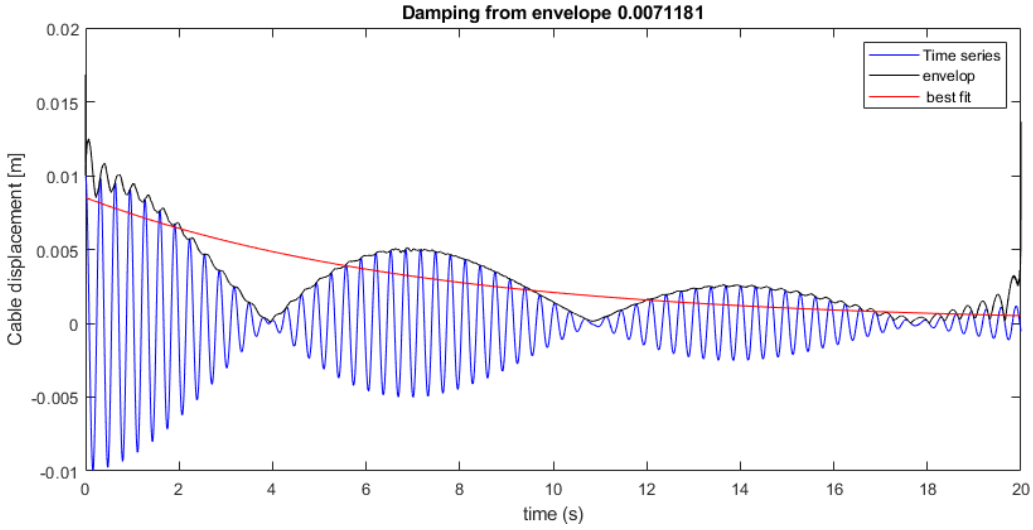

Figure 80 Cable equivalent damping ratio. Scenario 2

Figure 80 shows that the cable will experience $\zeta_3 = 0{,}0071$ which is more than half of the Stockbridge damper damping ratio $\zeta_{SB} = 0{,}01$.

The third scenario will be as follows:

- Damping ratio of $\zeta_{SB} = 0{,}05 \therefore c_{SB} = \zeta * 2 * \sqrt{k_{SB} * m_{SB}}$
- Initial displacement $x_{3_0} = 0{,}01\ m$

- No exciting force

The value of $\zeta_{SB} = 0{,}05$ was the minimum value of damping ratio found when testing it with a cam machine. [32]

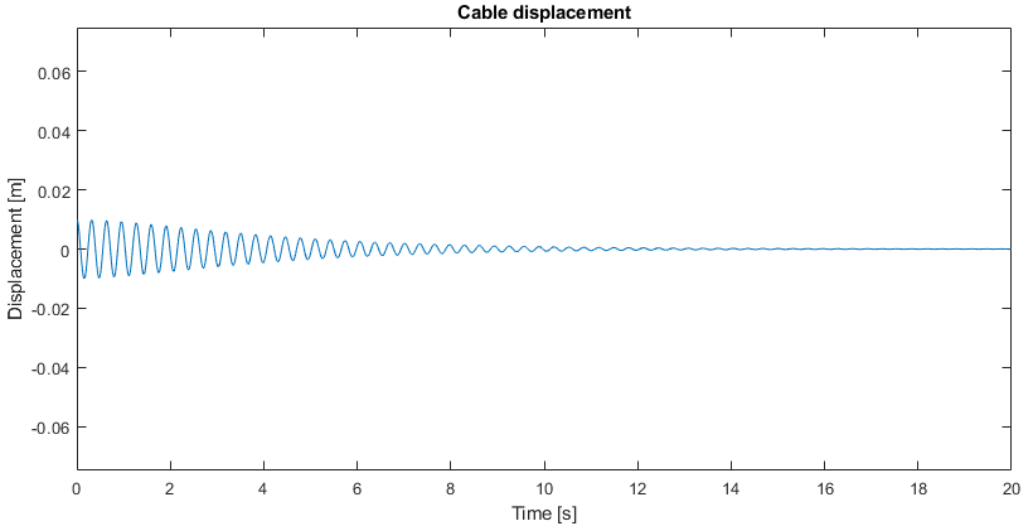

Figure 81 Cable displacement. Scenario 3

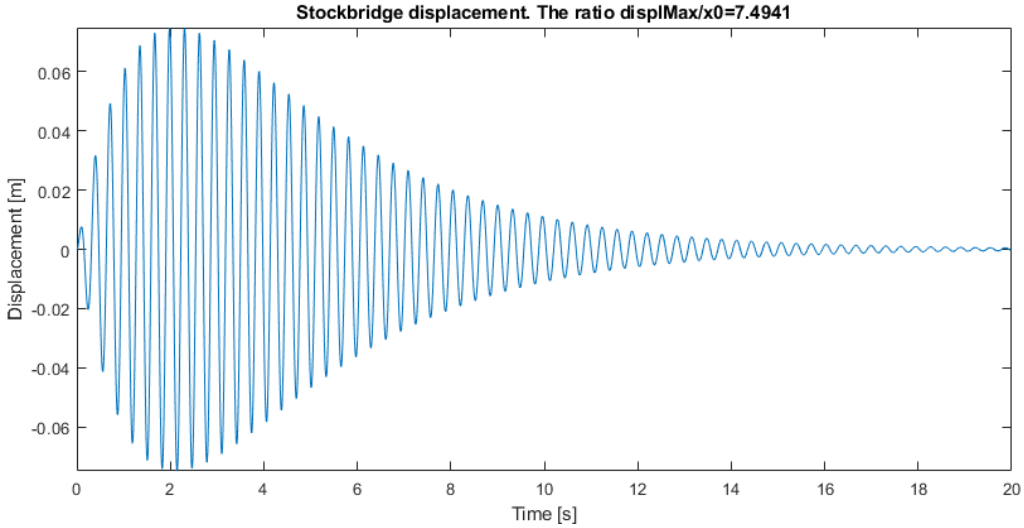

Figure 82 Stockbridge displacement. Scenario 3

The maximum amplitude of displacement of the Stockbridge device is around half of the maximum amplitude when no damping was introduced in the system.

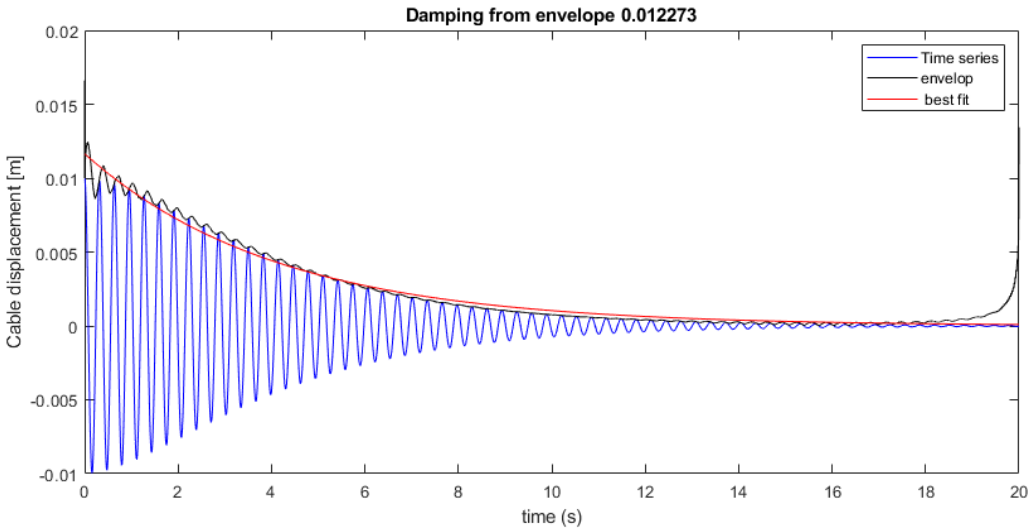

Figure 83 Cable equivalent damping ratio. Scenario 3

The cable equivalent damping ratio is lower than half of the damping ratio of the Stockbridge damper. There is no more beating phenomenon, which could be the reason why the damping ratio of the cable is lower, in percentage of the damping ratio of the Stockbridge damper.

When $\zeta_{SB} = 0{,}01$ the resulting damping ratio was 71,2%. When $\zeta_{SB} = 0{,}05$ the resulting damping ratio was 24,6.

The fourth scenario will be as follows:

- Damping ratio of $\zeta_{SB} = 0{,}00 \therefore c_{SB} = \zeta * 2 * \sqrt{k_{SB} * m_{SB}}$
- No initial displacement
- Random exciting force

The random exciting force was calculated using a sum of 20 sine functions with random frequencies ω_i ranging between 0 and 50 rad/s and random phases φ_i ranging between 0 and $2 * \pi\ rad$, all with magnitude 100 N.

$$F(t) = \sum_{i=1}^{20} 100 * \sin(\omega_i * t + \varphi_i) \qquad 61$$

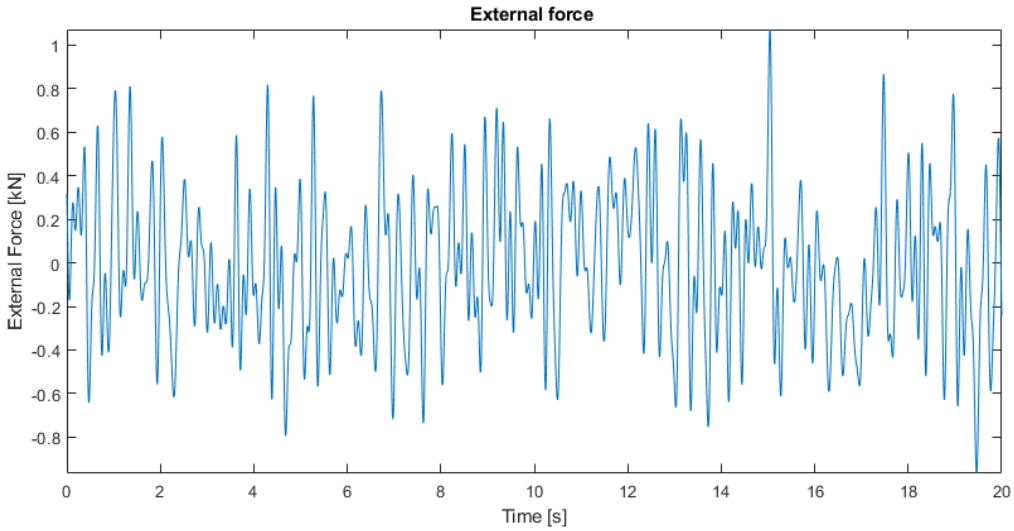

Figure 84 External force

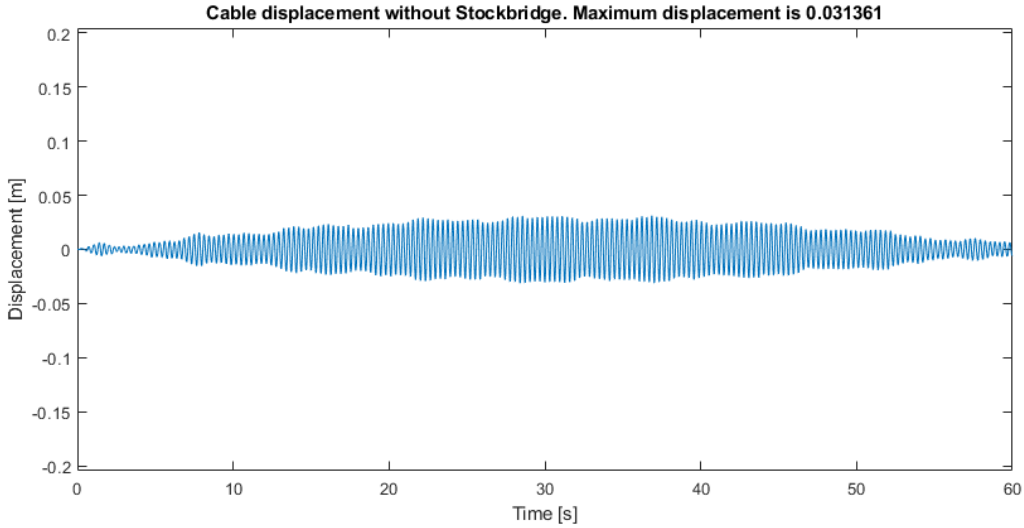

Figure 85 Cable displacement when random force is applied, without Stockbridge damper

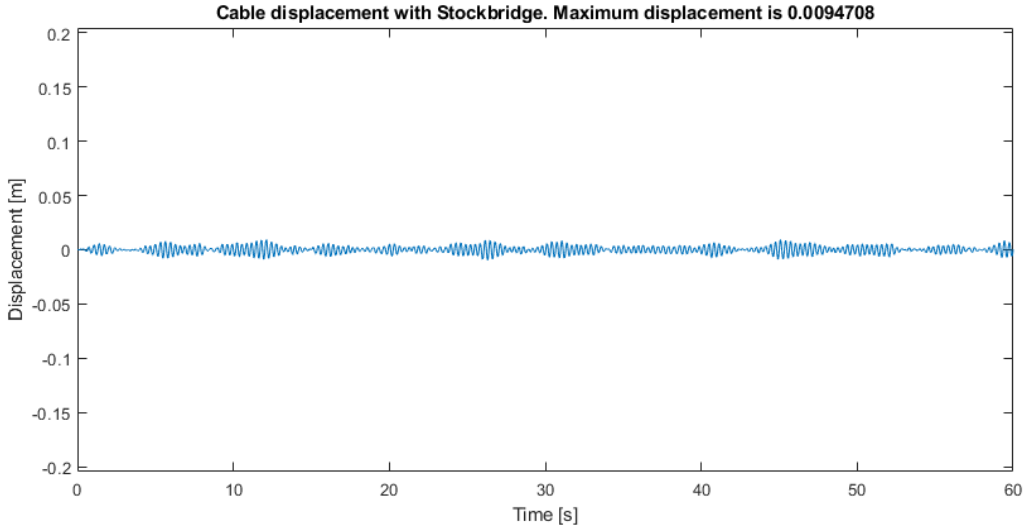

Figure 86 Cable displacement with random force, with Stockbridge damper, $\zeta = 0$

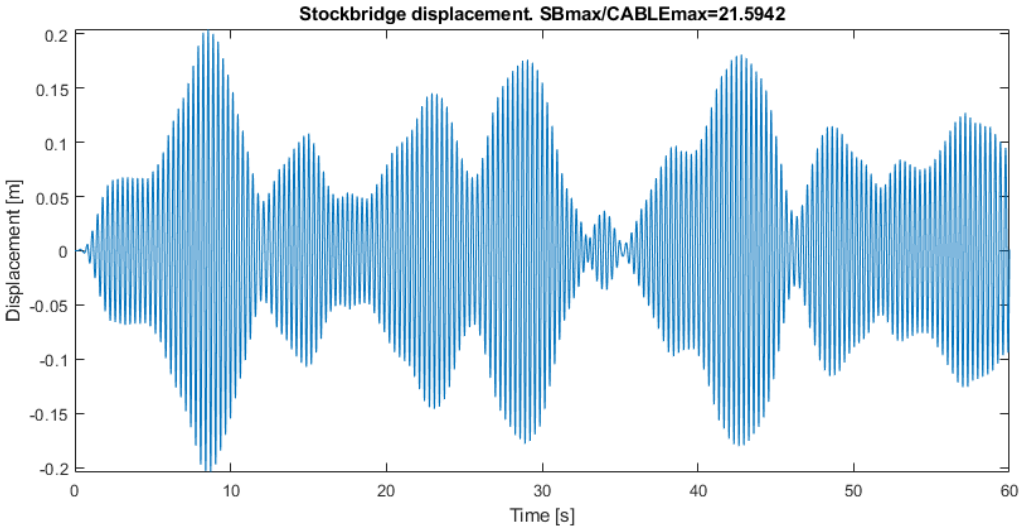

Figure 87 Stockbridge displacement with random force, $\zeta = 0$

For the above scenario, the largest amplitude that the cable experienced without the Stockbridge damper was $0{,}031\ m$ whereas when the Stockbridge was added the largest vibration amplitude on the cable was $0{,}00947\ m$. Which is $30,5\%$ of the value without the Stockbridge damper. This means that even if the Stockbridge damper does not have any inherited damping coefficient, it is still able to reduce the cable vibration peaks by near 70%. The maximum displacement of the Stockbridge damper is $20{,}3$ times the maximum displacement of the cable, this happens because of the much lower mass of the damper. Displacements of around $20\ cm$ can be seen.

The fifth scenario will be as follows:

- Damping ratio of $\zeta_{SB} = 0{,}01 \therefore c_{SB} = \zeta * 2 * \sqrt{k_{SB} * m_{SB}}$
- No initial displacement
- Random exciting force, same as in previous case

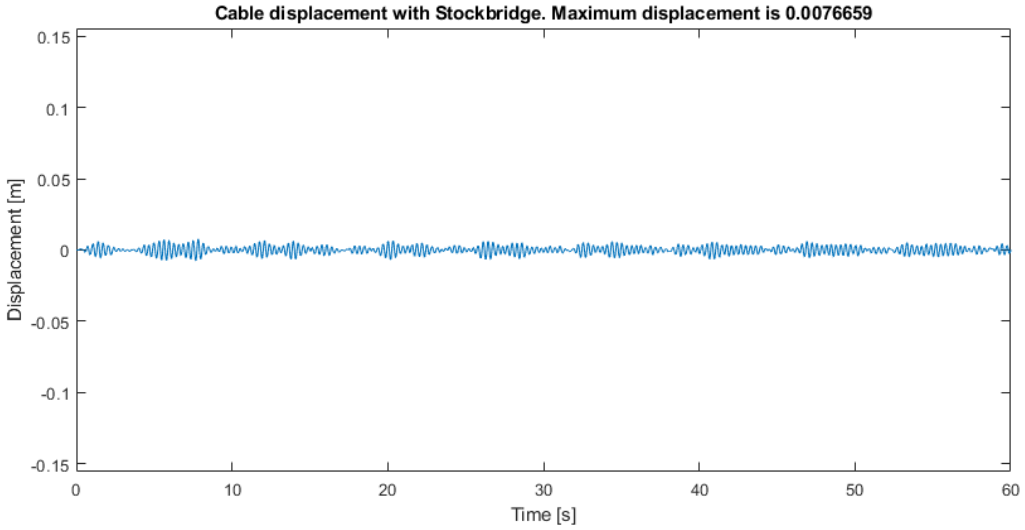

Figure 88 Cable displacement with random force, with Stockbridge damper, $\zeta = 0{,}01$

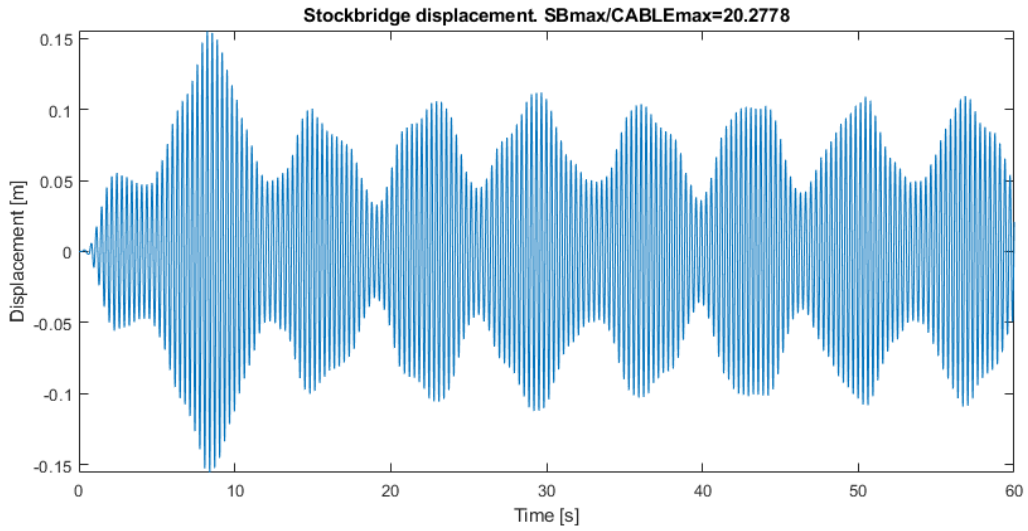

Figure 89 Stockbridge displacement with random force, $\zeta = 0{,}01$

For the above scenario, the largest amplitude that the cable experienced without the Stockbridge damper was $0{,}031\ m$ whereas when the Stockbridge was added the largest vibration amplitude on the cable was $0{,}0077\ m$. Which is $24{,}8\%$ of the value without the Stockbridge damper. There is no large difference between the values of peak displacement for $\zeta = 0{,}01$ and $\zeta = 0$ described in the previous case. The maximum displacement of the Stockbridge damper is $20{,}3$ times the maximum displacement of the cable, this happens because of the much lower mass of the damper.

The sixth scenario will be as follows:

- Damping ratio of $\zeta_{SB} = 0{,}05 \therefore c_{SB} = \zeta * 2 * \sqrt{k_{SB} * m_{SB}}$
- No initial displacement
- Random exciting force, same as in previous case

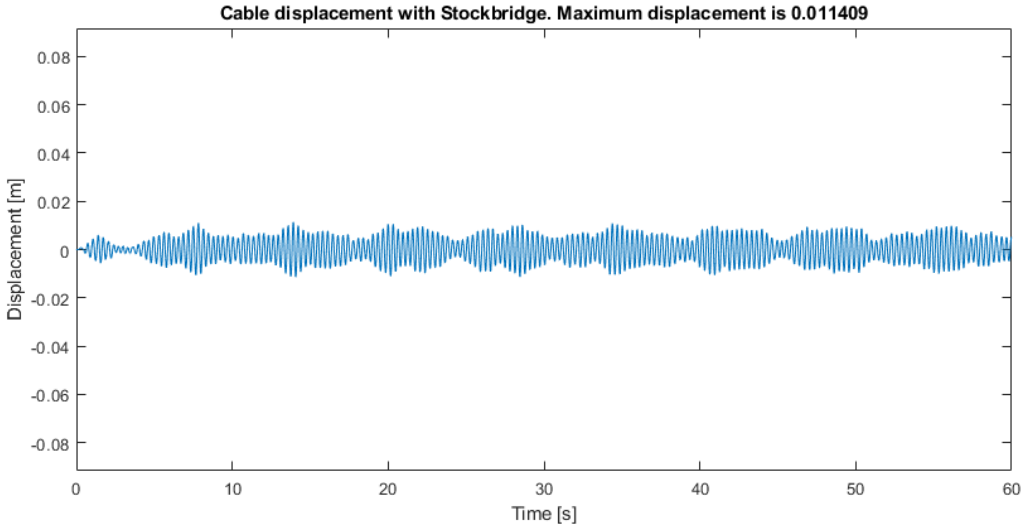

Figure 90 Cable displacement with random force, with Stockbridge damper, $\zeta = 0{,}05$

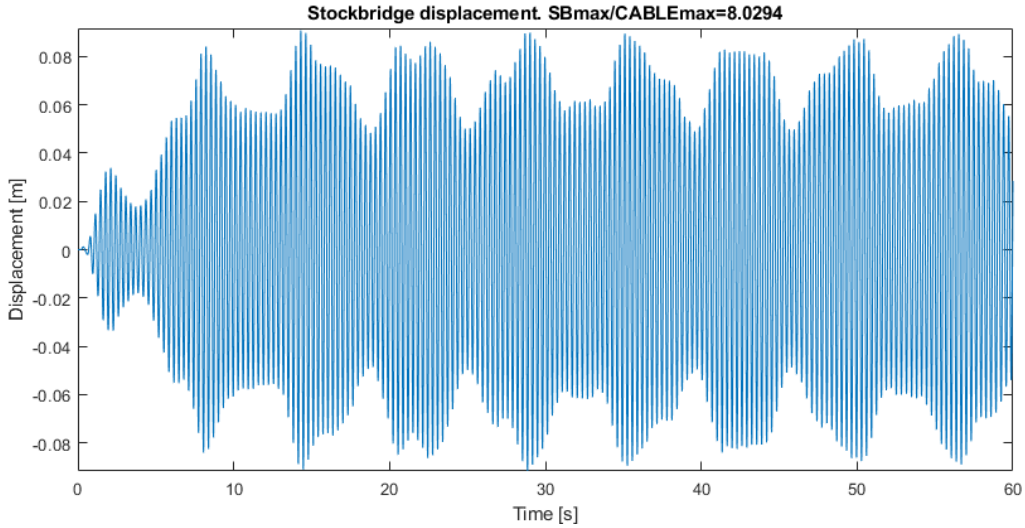

Figure 91 Stockbridge displacement with random force, $\zeta = 0{,}05$

For the above scenario, the largest amplitude that the cable experienced without the Stockbridge damper was $0{,}031\ m$ whereas when the Stockbridge was added the largest vibration amplitude on the cable was $0{,}0114\ m$. This value is larger than the value for $\zeta = 0{,}01$. This means that a Stockbridge damper with increasing damping ratio is showing to be less efficient in damping cable vibration amplitudes.

A similar procedure described in 3.3.2 an in 3.3.3 could applied to the cable displacement with the damper, in order to try to estimate what is the overall damping ratio of the system, however, that is not the scope of this thesis.

4 Conclusion

The thesis had two aims. First, to assess the key dynamic parameters of the stay cables at Bybrua by examining the acceleration data recorded under ambient excitations, as well as free vibration. Second, to estimate the design of a relevant damper.

Signal processing techniques were used to analyse the acceleration response, while the damping ratio was estimated using Free Decay Response, Frequency Domain Decomposition and Random Decrement Technique. The damping ratio was analysed as a function of the displacement amplitude, in order to investigate whether damping varies with amplitude. An analysis of the cable response, when coupled with a Stockbridge damper device using a two degree of freedom system, was carried out to estimate the impact on cable vibrations.

The eigenfrequencies found are within the expected range when compared to the parameters from the original design. The eigenfrequencies are consistent within each other, closely following the simplified taut string model. Estimates for the damping ratio varied depending on the method used. For Free Decay Response, the damping ratio was between 0,03% and 0,07%. Frequency Domain Decomposition showed values between 0,13% and 0,26%. Random Decrement Technique gave results between 0,07% and 0,18%.

The two degree of freedom system, comprised of the Stockbridge damper and modal characteristics of the cable, showed that the damping device can be effective at controlling the vibration amplitude of the cable. Even when the inherent damping of both cable and Stockbridge damper was set to 0, the largest vibration on the cable was reduced by 70%.

Further work should be done to investigate the damping solutions for the stay cables, to mitigate cable vibrations.

5 References

[1] N. Gimsing, Cable Supported Bridges : Concept and Design, John Wiley & Sons, 2012.

[2] N. Daniotti, “Full-Scale observations of bridge stay cable vibrations,” University of Stavanger, Stavanger, 2020.

[3] M. Virlogeux, State-of-the-art in cable vibrations of cable-stayed bridges, London: Taylor & Francis, 2005.

[4] “Wikipedia,” [Online]. Available: https://commons.wikimedia.org/wiki/Category:Bendorfer_Br%C3%BCcke. [Accessed 05 06 2022].

[5] H. Johs, Norwegian Bridge Building, Oslo: TAPIR, 1981.

[6] “Wikipedia,” [Online]. Available: https://en.wikipedia.org/wiki/List_of_longest_suspension_bridge_spans. [Accessed 20 05 2022].

[7] F. G. Jr., “Silver Bridge Failure 1967 (aka Point Pleasant Bridge),” *STRUCTURE Magazine*, pp. 62-64, 2022.

[8] Redaelli Tecna S.P.A., Tensostructures, suspension structures, cable stayed structures, Milano, Italy: Redaelli.

[9] A. M. L. Cardoso, Estudo da rigidez efetiva do cabo de ponte estaiada. English: Study of the effective rigidity of a cable-stayed bridge cable, São Carlos: Universidade de São Paulo, 2013.

[10] U.S. Department of Transportation, Federal Highway Administration, Wind-Induced Vibration of Stay Cables, McLean, United States, 2007.

[11] J. Jakobsen, Environmental Loads - Lecture Notes, Stavanger: University of Stavanger, 2020.

[12] J. Holmes, Wind loading of structures, London: Spon Press, 2001.

[13] Post-Tensioning Institute, Post-Tensioning Manual, Phoenix: Post-Tensioning Institute, 2006.

[14] Y. Fujino and D. Siringoringo, “Vibration Mechanisms and Controls of Long-Span Bridges: A Review,” Structural Engineering International, Tokyo, 2013.

[15] “Google Maps,” [Online]. Available: https://www.google.com/maps/. [Accessed 20 05 2022].

[16] “PE Specialisten Technology,” [Online]. Available: https://www.pes-tec.com/products/stay-cable-protection. [Accessed 06 06 2022].

[17] J. Holt and A. Selberg, “Strømsteingbrua Stavanger,” Trondheim/Oslo, 1976.

[18] DAMPTECH, [Online]. Available: https://www.damptech.com/. [Accessed 13 03 2022].

[19] “Kommunekart,” [Online]. Available: https://kommunekart.com/. [Accessed 06 06 2022].

[20] “International Database and Gallery of Structures,” [Online]. Available: https://structurae.net/en/structures/stavanger-city-bridge. [Accessed 06 06 2022].

[21] “MicroStrain by Parker,” [Online]. Available: https://www.microstrain.com/wireless-sensors/g-link-200. [Accessed 2022 06 07].

[22] Vaisala, “Vaisala, Weather transmitter WXT530 Series,” [Online]. Available: https://www.vaisala.com/en/products/weather-environmental-sensors/weather-transmitter-wxt530-series. [Accessed 07 06 2022].

[23] CSI, “Canterbury Seismic Instruments,” [Online]. Available: https://www.csi.net.nz/index.php/general/products/. [Accessed 07 06 2022].

[24] J. Holt, “Statiske beregninger - Strømsteingbrua,” Oslo, 1975.

[25] I. The Math Works, *MATLAB Version 2021b,* The Math Works, Inc..

[26] D. Newland, An Introduction to Random Vibrations, Spectral & Walevet Analysis, Cambridge: University of Cambridge, 1994.

[27] H. D. The Government of Hong Kong. [Online]. Available: https://www.hyd.gov.hk/en/information_corner/hyd_factsheets/doc/e_Stonecutters_Bridge.pdf. [Accessed 05 06 2022].

[28] R. Brincker, L. Zhang and P. Andersen, “Modal Identification from Ambient Responses using Frequency Domain Decomposition,” International Modal Analysis Conveference (IMAC), San Antonio, 2000.

[29] E. Cheynet, Wind-induced vibrations of a suspension bridge. A case study in full-scale, Stavanger: University of Stavanger, 2016.

[30] I. The Math Works, “MathWorks Help Center,” The Math Works, Inc., [Online]. Available: https://se.mathworks.com/help/matlab/ref/ode45.html#References. [Accessed 05 06 2022].

[31] TESolution, “TESolution,” TESolution, [Online]. Available: http://www.tesolution.com/vibrationcontroltechnology.html. [Accessed 06 06 2022].

[32] N. Barbieri and R. Barbieri, “Dynamic Analysis of Stockbridge Damper,” Advances in Acoustics and Vibration, Curitiba, 2012.

[33] W. Podolny and J. B. Scalzi, Construction and design of cable-stayed bridges, New York: John Wiley & Sons, 1976.

[34] R. Brincker and C. Ventura, Introduction to Operational Modal Analysis, Chichester: John Wiley & Sons, Ltd, 2015.